Ionic Liquid/MOF Composites for CO_2 Separation: Combining Molecular Simulations and Experiments

by

Hüsamettin Mert Polat

A Thesis Submitted to the

Graduate School of Engineering

in Partial Fulfillment of the Requirements

for the Degree of

Master of Science

In

Materials Science and Engineering

Koç University

August 2019

Koç University

Graduate School of Sciences and Engineering

This is to certify that I have examined this copy of a master's thesis by

Hüsamettin Mert Polat

and have found that it is complete and satisfactory in all respects,

and that any and all revisions required by the final

examining committee have been made.

Committee Members:

Prof. Seda Keskin Avcı (Advisor, Koç University)

Assoc. Prof. Alper Uzun (Advisor, Koç University)

Assoc. Prof. Uğur Ünal (Koç University)

Asst. Prof. Cem Albayrak (Koç University)

Prof. Ramazan Yıldırım (Boğaziçi University)

Date: 09.08.2019

ABSTRACT

CO_2 adsorption and separation from flue gas and natural gas have significant environmental and industrial importance. Metal organic frameworks (MOFs) are promising adsorbent materials for CO_2 adsorption and separation processes due to their extraordinary properties and customizable chemistries. Post-synthesis modification of MOFs by incorporation of ionic liquids (ILs) is a new approach to enhance gas adsorption and separation performance of MOFs.

In the first part of this thesis, a computational methodology based on the state-of-the-art molecular simulations of IL/CuBTC composites composed of ILs having the same cation, 1-*n*-butyl-3-methylimidazole ($[BMIM]^+$), and various anions was proposed. Using grand canonical Monte Carlo (GCMC) simulations, CO_2, CH_4, and N_2 uptakes of seven different IL/CuBTC composites were predicted and compared with the experimental gas uptake measurements to select the most appropriate force field. Motivated from the good agreement between experiments and simulations, the same method was applied to estimate the gas adsorption in two new IL/CuBTC composites which have been synthesized and characterized for the first time in this work. Molecular simulations accurately predicted the experimental gas uptakes of newly synthesized composites, validating the transferability of the approach to different IL/CuBTC samples. A detailed analyses of binary gas mixture separation performances of IL/CuBTC composites and diffusion of gases in IL/CuBTC composites were also provided. In the second part, the computational methodology that proposed in the first part was validated using three 1-*n*-butyl-3-methylimidazolium tetrafluoroborate [BMIM][BF_4]/MOF composites with comparable IL-loadings, one of which was synthesized and characterized for the first time in this work. This computational methodology was then used to predict the CO_2/N_2 binary mixture adsorption and separation performances of 1108 different [BMIM][BF_4]/MOF composites. Results showed that vast majority of the [BMIM][BF_4]/MOF composites exhibit increase in their CO_2 adsorption and separation performances. Structural reasons behind the increased performance of IL/MOF composites were examined. The results of this thesis show that IL/MOF composites have a great potential in CO_2 adsorption and separation. Results and the methodology provided in this work will be useful to assess the CO_2 adsorption and separation performances of different IL/MOF composites.

ÖZET

CO_2'nin baca gazı ve doğal gazdan adsorpsiyonu ve ayrılması çevresel ve endüstriyel öneme sahiptir. Metal organik kafesli yapılar (MOF'lar) olağanüstü özellikleri ve özelleştirilebilir kimyaları nedeniyle CO_2 adsorpsiyonu ve ayırma işlemleri için ümit verici malzemelerdir. İyonik sıvıların (IL'ler) katılmasıyla MOF'ların sentez sonrası modifikasyonu, MOF'ların gaz adsorpsiyonu ve ayırma performansını arttırmak için yeni bir yaklaşımdır.

Bu tezin ilk bölümünde, aynı katyona (1-*n*-bütil-3-metilimidazol ($[BMIM]^+$)) ve çeşitli anyonlara sahip IL'lerden oluşan IL/CuBTC kompozitlerinin, moleküler simülasyonları için bir hesaplama metodolojisi önerildi. Büyük kanonik Monte Carlo (GCMC) simülasyonları kullanılarak, yedi farklı IL/CuBTC kompozitinin CO_2, CH_4 ve N_2 tutma kapasiteleri tahmin edildi ve bu simülasyonlar için en uygun kuvvet alanını seçmek için deneysel ölçümlerle karşılaştırıldı. Deneyler ve simülasyonlar arasındaki uyumdan yola çıkarak, bu çalışmada ilk kez sentezlenen ve karakterize edilen iki yeni IL/CuBTC kompozitlerin gaz adsorpsiyonunu tahmin etmek için aynı yöntem uygulandı. Moleküler simülasyonlar, bu yaklaşımın farklı IL/CuBTC örneklerine aktarılabilirliğini doğrulayarak yeni sentezlenmiş kompozitlerin deneysel gaz kapasitelerini doğru bir şekilde öngörmüştür. IL/CuBTC kompozitlerinin ikili gaz karışımı ayırma performanslarının ve IL/CuBTC kompozitlerinde gazların difüzyonunun detaylı bir analizi de sağlandı. İkinci bölümde, birinci bölümde önerilen hesaplama metodolojisi, karşılaştırılabilir IL-yüklemesine sahip üç 1-*n*-bütil-3-metilimidazolyum tetrafloroborat ($[BMIM][BF_4]$)/MOF kompozitleri kullanılarak doğrulandı ve bu kompozitlerden birisi bu çalışma için ilk defa sentezlendi ve karakterize edildi. Bu hesaplama metodolojisi daha sonra 1108 farklı $[BMIM][BF_4]$/MOF kompozitin CO_2/N_2 ikili karışım adsorpsiyon ve ayırma performanslarını tahmin etmek için kullanıldı. Sonuçlar, $[BMIM][BF_4]$/MOF kompozitlerinin büyük çoğunluğunun, CO_2 adsorpsiyon ve ayırma performanslarında artış sergilediğini gösterdi. Ayrıca, IL/MOF kompozitlerin performansındaki artışın ardındaki bazı yapısal nedenler sunuldu. Bu tezin sonuçları, IL/MOF kompozitlerinin CO_2 adsorpsiyon ve ayrılmasında büyük bir potansiyele sahip olduğunu göstermektedir. Bu sonuçları ve sağlanan metodolojiyi kullanarak, IL/MOF kompozitleri hakkında daha iyi bilgi sahibi olabilmek adına, farklı MOF ve IL ailelerini içeren tarama çalışmaları gerçekleştirilebilir.

ACKNOWLEDGEMENTS

First of all, I would like to express my thanks to my supervisors Prof. Seda Keskin and Assoc. Prof Alper Uzun for their supervision and support during my M.Sc. studies. It has been a great opportunity and chance for me to work with them. I also would like to thank to Prof. Ramazan Yıldırım, Assoc. Prof. Uğur Ünal and Asst. Prof. Cem Albayrak for being my committee members and their valuable time.

This project funded by Tübitak (project number: 114R093). I sincerely acknowledge the support of Koç University Seed Program and Koç University-Tüpraş Energy Center (KÜTEM). I am grateful to Koç University Surface Science and Technology Center (KUYTAM), especially to Barış Yağcı, Ceren Yılmaz Akkaya, Gülsu Şimşek and Işınsu Baylam for their help in various characterization equipment.

I also would like to express my sincere thanks to all the members of NEMO and Uzun Lab, especially, Çiğdem Altıntaş, Sadiye Velioğlu and İlknur Eruçar for helping me with simulations always with kindness and care and Melike Babucci and Ahsan Jalal for their most patient help in the lab. I would like to thank to Harun Kulak for being a great colleague and friend to me and fruitful discussions we had about almost everything.

My most special thanks are to beloved Safiyye Kavak. She was always there to support me intellectually and emotionally with kindness, care and passion. Her perspective of world led me to the person who I am now. Without her, no success would be possible for me.

I also would like to express my most genuine gratitude and appreciation to my mother, Semra Polat, my father, Zeki Polat, my sister, Zülal Erdem Polat, and grandmothers, Zübeyde Polat and Pakize Erdem. Thank you for supporting me in every aspect of my life.

TABLE OF CONTENTS

ABSTRACT....ii
ÖZET iii
ACKNOWLEDGEMENTS....iv
LIST OF TABLES....vii
LIST OF FIGURES ix
NOMENCLATURE xii
Chapter 1: Introduction....1
Chapter 2: Literature Review....5
2.1 Experimental Studies of IL/MOF Composites for Gas Adsorption and Separation 5
2.2 Molecular Simulation Studies of IL/MOF Composites for Gas Adsorption and Separation....6
Chapter 3: Methods....9
3.1. Computational Methods....9
3.2. Experimental Methods....14
3.2.1. Sample Preparation 14
3.2.2. Sample Characterization 14
3.2.2.1. X-ray Diffraction (XRD)....14
3.2.2.2. Scanning Electron Microscopy (SEM)....15
3.2.2.3. Fourier Transform Infrared (FTIR) Spectroscopy....15
3.2.2.4. Brunauer-Emmett-Teller (BET) Surface Area 15
3.2.2.5 X-ray Fluorescence Spectroscopy (XRF)....15
3.2.2.6. Thermogravimetric Analysis (TGA) 16
3.2.3. Gas Adsorption Measurements 16
Chapter 4: Unlocking CO_2 Separation Performance of Ionic Liquid/CuBTC Composites: Combining Experiments with Molecular Simulations....17
4.1. Force Field Selection for Molecular Simulations of IL/CuBTC Composites....17
4.2. Application of Computational Approach to Two Different IL/CuBTC Composites 25
4.3. Gas Mixture Separation Performances of IL/CuBTC Composites....31

4.4. Gas Diffusion in IL/CuBTC Composites 33

Chapter 5: High-throughput Computational Screening of [BMIM][BF_4]/MOF Composites for CO_2 Separation from Flue Gas 37

5.1. Selection of IL, MOFs and IL-incorporation Method 37

5.2. Validation of Accuracy of Molecular Simulation Method 41

5.2.1 Characterization and CO_2 Adsorption and Separation Performance of [BMIM][BF_4]/UiO-66 Composite 41

5.2.1.1 X-ray Fluorescence Spectroscopy 42

5.2.1.2 BET Surface Area and Pore Volume Analysis 42

5.2.1.3 X-ray Diffraction 43

5.2.1.4 Scanning Electron Microscopy 44

5.2.1.5 Thermogravimetric Analysis 45

5.2.1.6 Fourier Transform Infrared Spectroscopy 47

5.2.1.7 CO_2 and N_2 Adsorption and Separation Performance of [BMIM][BF_4]/UiO-66 48

5.2.2 Validation of Molecular Simulation Results 50

5.3. CO_2 Separation from Flue Gas Mixtures Using [BMIM][BF_4]/MOF Composites 51

5.4. Structural Reasons Behind CO_2 Adsorption and Separation Performance Increase upon [BMIM][BF_4] Incorporation 57

5.4.1 Effect of Weight Percent IL-loading on the CO_2/N_2 Selectivity of [BMIM][BF_4]/MOF Composites 57

5.4.2 Effect of PLD on the CO_2/N_2 Selectivity of [BMIM][BF_4]/MOF Composites 59

5.4.3 Effect of Porosity on the CO_2/N_2 Selectivity of [BMIM][BF_4]/MOF Composites 62

Chapter 6: Conclusions and Outlook 66

BIBLIOGRAPHY 69

APPENDIX A: Supplementary for Computational Details 81

APPENDIX B: Supplementary Information for Chapter 4 100

APPENDIX C: Supplementary Information for Chapter 5 108

LIST OF TABLES

Table 3.1. Adsorbent selection metrics used in this thesis to evaluate the performance of pristine MOFs and IL/MOF composites 13

Table 4.1. Gas coefficients (A_i) in scaling factor for low pressure (LP), mid pressure (MP), and high pressure (HP). 22

Table 5.1. CSD refcodes of pristine MOFs showing an APS increase of 10-times and retaining 85% R% upon [BMIM][BF_4]-incorporation. 56

Table A.1. Force field parameters used to represent IL/MOF composites. 81

Table A.2. Parameters used to represent gases in molecular simulations. 82

Table A.3. The largest cavity diameters (LCDs) and pore limiting diameters (PLDs) of pristine CuBTC and IL/CuBTC composites. 82

Table A.4. Number of IL molecules per unit cell and calculated IL loading for IL/CuBTC composites used in molecular simulations. 83

Table A.5. ZPVE-corrected binding energies of all conformers. 83

Table A.6. Atomic positions and point charges (NBO) of [BMIM][BF_4] optimized at B3LYP/6-311+G(2d,p). 85

Table A.7. Atomic positions and point charges (NBO) of [BMIM][CF_3SO_3] optimized at B3LYP/6-311+G(2d,p). 86

Table A.8. Atomic positions and point charges (NBO) of [BMIM][$MeSO_3$] optimized at B3LYP/6-311+G(2d,p). 87

Table A.9. Atomic positions and point charges (NBO) of [BMIM][$MeSO_4$] optimized at B3LYP/6-311+G(2d,p). 89

Table A.10. Atomic positions and point charges (NBO) of [BMIM][SbF_6] optimized at B3LYP/DGDZVP. 90

Table A.11. Atomic positions and point charges (NBO) of [BMIM][PF_6] optimized at B3LYP/6-311+G(2d,p). 92

Table A.12. Atomic positions and point charges (NBO) of [BMIM][$OcSO_4$] optimized at B3LYP/6-311+G(2d,p). 93

Table A.13. Atomic positions and point charges (NBO) of [BMIM][DCA] optimized at B3LYP/6-311+G(2d,p). 95

Table A.14. Atomic positions and point charges (NBO) of [BMIM][DBP] optimized at B3LYP/6-311+G(2d,p). 96

Table B.1. Dual-site Langmuir* fit parameters for [BMIM][DCA]/CuBTC and [BMIM][DBP]/CuBTC. 100

Table C.1. Freundlich* fit parameters for N_2 adsorption isotherms of UiO-66 and [BMIM][BF_4]/UiO-66.....108

Table C.2. Dual-site Langmuir fit parameters for N_2 adsorption isotherms of UiO-66 and [BMIM][BF_4]/UiO-66.....109

Table C.3. Notes about the structures of MOFs that show APS increase higher than 10-times upon IL-incorporation. 109

LIST OF FIGURES

Figure 4.1. (a) Single-component adsorption isotherms of CO_2, CH_4, and N_2 as a function of pressure in pristine CuBTC, (b) comparison of experiments and simulations using UFF and Dreiding force fields for CuBTC. 19

Figure 4.2. Comparison of experiments with simulations using (a) UFF and (b) Dreiding force fields for gas uptakes in seven different IL/CuBTC composites.....21

Figure 4.3. Comparison of scaled and unscaled simulations with experimental uptakes of (a) CO_2, (b) CH_4, (c) N_2, and (d) all gases. Filled (empty) symbols represent scaled (non-scaled) simulations. Color code follows that in Figure 4.2. 24

Figure 4.4. Comparison of experimental and simulated selectivities for 7 different IL/CuBTC composites. 25

Figure 4.5. (a) XRD patterns, (b) TGA curves of CuBTC, [BMIM][DCA]/CuBTC, [BMIM][DBP]/CuBTC, and bulk ILs, (c) FTIR spectra of CuBTC, [BMIM][DCA]/CuBTC, [BMIM][DBP]/CuBTC, and bulk ILs, (d) CO_2, CH_4, and N_2 adsorption isotherms of [BMIM][DCA]/CuBTC and [BMIM][DBP]/CuBTC. 28

Figure 4.6. (a) Comparison of scaled simulation results and experimental uptakes for [BMIM][DCA]/CuBTC and [BMIM][DBP]/CuBTC composites, (b) ideal and (c) mixture selectivities of two composites calculated from GCMC simulations. The first component in the label indicates the selected one over the other. 30

Figure 4.7. Comparison of experimental and simulated selectivities of [BMIM][DCA]/CuBTC and [BMIM][DBP]/CuBTC composites.....31

Figure 4.8. CO_2/CH_4:50/50, CO_2/N_2:15/85, and CH_4/N_2:50/50 mixture selectivities calculated by GCMC simulations as a function of pressure for pristine CuBTC and IL/CuBTC composites. 33

Figure 4.9. D^0 values for (a) CO_2, (b) CH_4, and (c) N_2 in IL/CuBTC composites. For (a-c), IL-gas (CuBTC-gas) interactions are considered in the first (second) column. All interactions are considered in the third column. (d) Variation of D^0 values of CO_2, CH_4, and N_2 with respect to pore volume of IL/CuBTC composites and pristine CuBTC. 35

Figure 5.1. Comparison of CO_2 and N_2 uptakes simulated using the methodologies including Baker's minimization and CBMC for minimization of IL molecules. 39

Figure 5.2. Comparison of CO_2/N_2 selectivities simulated using the methodologies including Baker's minimization and CBMC for minimization of IL molecules 40

Figure 5.3. N_2 adsorption isotherms of UiO-66 and [BMIM][BF_4]/UiO-66 at -196 °C. 43

Figure 5.4. XRD patterns of UiO-66 and [BMIM][BF_4]/UiO-66 composite. 44

Figure 5.5. SEM micrographs of (a,b) UiO-66 and (c,d) [BMIM][BF_4]/UiO-66 at (a,c) 15k× and (b,d) 50k× magnifications. 45

Figure 5.6. (a) Thermogravimetric and (b) derivative thermogravimetric curves of [BMIM][BF_4], UiO-66 and [BMIM][BF_4]/UiO-66. 46

Figure 5.7. FTIR spectra of [BMIM][BF_4], UiO-66 and [BMIM][BF_4]/UiO-66. 47

Figure 5.8. CO_2 and N_2 adsorption isotherms of [BMIM][BF_4]/UiO-66 and UiO-66 as a function of pressure. Square (round) symbols represent CO_2 (N_2) uptakes. 48

Figure 5.9. Ideal CO_2/N_2 selectivity of [BMIM][BF_4]/UiO-66 and pristine UiO-66 as a function of pressure. 49

Figure 5.10. Comparison of experimental and simulated CO_2/N_2 selectivity and CO_2 working capacity of [BMIM][BF_4]/CuBTC, [BMIM][BF_4]/ZIF-8 and [BMIM][BF_4]/UiO-66 composites. 50

Figure 5.11. Selectivities and CO_2 working capacities of [BMIM][BF_4]/MOF composites calculated at adsorption and desorption pressures of 1 and 0.1 bar, respectively, for CO_2/N_2:15/85 mixture at 25 °C. 52

Figure 5.12. Normalized selectivity and normalized CO_2 working capacity of [BMIM][BF_4]/MOF composites for CO_2/N_2 mixture. 53

Figure 5.13 R% and APS of pristine MOFs and [BMIM][BF_4]/MOF composites computed at adsorption (desorption) pressure of 1 (0.1) bar and 25 °C for CO_2/N_2:15/85 mixture. The black dotted line shows the minimum desired R% = 85%. 54

Figure 5.14. Normalized R% and normalized APS of [BMIM][BF_4]/MOF composites for CO_2/N_2 mixture. The black dotted lines show the 20% change in R%. 55

Figure 5.15. Weight percent IL loading and normalized selectivity of [BMIM][BF_4]/MOF composites. 58

Figure 5.16. Percentage of [BMIM][BF_4]/MOF composites that are more than 3-times selective than their corresponding MOFs for different ranges of IL loading. 59

Figure 5.17. CO_2/N_2 selectivities at 1 bar and PLDs of pristine MOFs and [BMIM][BF_4]/MOF composites 60

Figure 5.18. Reduction in PLD (%) upon IL-incorporation and normalized selectivity of [BMIM][BF_4]/MOF composites. 61

Figure 5.19. Porosities and CO_2/N_2 selectivities of pristine MOFs and [BMIM][BF_4]/MOF composites. 63

Figure 5.20. Reduction in porosity upon [BMIM][BF_4]-incorporation to MOFs and normalized selectivities of [BMIM][BF_4]/MOF composites. 64

Figure A.1. Ball-and-stick molecular structures of (a) [BMIM][BF_4], (b) [BMIM][CF_3SO_3], (c) [BMIM][$MeSO_4$], (d) [BMIM][$MeSO_3$], (e) [BMIM][PF_6], (f) [BMIM][SbF_6], (g) [BMIM][$OcSO_4$], (h) [BMIM][DCA] and (i) [BMIM][DBP].....99

Figure B.1. SEM images of (a,b) pristine CuBTC [BMIM][DCA]/CuBTC, (c,d) [BMIM][DCA]/CuBTC and (e,f) [BMIM][DBP]/CuBTC at different magnifications. 101

Figure B.2. (a) TGA and (b) derivative TGA curves of CuBTC, [BMIM][DCA]/CuBTC, and bulk [BMIM][DCA]. 102

Figure B.3. (a) TGA and (b) derivative TGA curves of CuBTC, [BMIM][DBP]/CuBTC, and bulk [BMIM][DBP].....103

Figure B.4. (a) Experimental ideal CO_2/CH_4, CO_2/N_2, and CH_4/N_2 selectivities of CuBTC, [BMIM][DCA]/CuBTC, and [BMIM][DBP]/CuBTC as a function of pressure. (b) Mixture selectivities calculated using IAST from experimental uptakes of [BMIM][DCA]/CuBTC and [BMIM][DBP]/CuBTC as a function of pressure. 104

Figure B.5. FTIR spectra of (a) toluene, filtrate after washing [BMIM][DCA]/CuBTC and filtrate after [BMIM][DBP]/CuBTC with toluene. FTIR spectra of (b) [BMIM][DCA]/CuBTC and (c) [BMIM][DBP]/CuBTC before and after washing. ...105

Figure B.6. N_2 adsorption-desorption isotherms of [BMIM][DCA]/CuBTC and [BMIM][DBP]/CuBTC at -196 °C. 106

Figure B.7. Experimental adsorption isotherms and dual-site Langmuir fits of [BMIM][DCA]/CuBTC and [BMIM][DBP]/CuBTC. Lines represent the corresponding dual-site Langmuir fit. 107

NOMENCLATURE

IL: Ionic liquid

MOF: Metal organic framework

NBO: Natural bond orbit

GCMC: Grand canonical Monte Carlo

MD: Molecular dynamics

UFF : Universal force field

LJ: Lennard-Jones

LCD: Largest cavity diameter

PLD: Pore limiting diameter

CSD: Cambridge Structural Database

QEq: Charge equilibration

DFT: Density Functional Theory

R^2: Correlation coefficient

S: Selectivity

ΔN: Working capacity

R%: Percent regenerability

APS: Adsorbent performance score

XRD: X-ray diffraction

SEM: Scanning electron microscopy

FTIR: Fourier transform infrared

ATR: Attenuated total reflectance

BET: Brunauer–Emmett–Teller

XRF: X-ray fluorescence

TGA: Thermogravimetric analysis

HPVA: High-pressure volumetric analyzer

STP: Standard temperature and pressure

IAST: Ideal Adsorbed Solution Theory

CBMC: Configurational-bias Monte Carlo

Chapter 1: Introduction

Carbon dioxide (CO_2) capture from natural gas and flue gas has a significant environmental, social, economic, and industrial importance.[1–3] CO_2 concentration in the atmosphere increased from 280 ppm in the pre-industrial revolution time to above 400 ppm today.[4] Contribution of emissions from fossil fuels to this increase is higher than 2 ppm per year, presenting the importance of CO_2 capture from flue gas.[5] On the other hand, presence of CO_2 in the natural gas decreases its energy density and causes corrosion in pipelines. Although the limit of CO_2 concentration in the natural gas is dictated by different regulations, it is generally expected not to exceed 2%.[6] Therefore, developing efficient technologies for CO_2 separation from flue gas and natural gas has significant environmental importance. Among many available techniques,[7] adsorption-based CO_2 separation is widely preferred since it is low-cost, energy efficient, and easy to operate. A large variety of porous materials has been developed and tested for adsorption-based CO_2 separation to date, including activated carbons,[8] zeolites,[9] silica gels,[10] carbon nanotubes,[11] and metal organic frameworks (MOFs).[12,13]

MOFs are a relatively new group of crystalline porous materials comprised of metal ions or clusters connected to each other with organic ligands.[14] They have gained significant attention because of their extraordinary properties, such as very high surface areas, high porosities, low densities, and tunable structures,[15] which make them potential materials in various applications including catalysis,[16] drug delivery,[17] fuel cell applications,[18] gas storage, and gas separation.[13,19] MOFs have been considered as strong candidates for gas adsorption and various gas separation applications, because they can be designed with desired structural and chemical properties for a target

process.[20–22] However, complicated synthesis procedures are often required to discover new MOFs having high gas separation performances. Post-synthetic modification of MOFs creates an alternative to this approach offering materials having high performance with relatively simpler synthesis procedures. A very recent approach is the post-synthetic modification of MOFs with ionic liquids (ILs) to tune the gas adsorption and selectivity of MOFs. ILs, organic salts that are liquid below 100 °C,[23] have high thermal stabilities, negligible vapor pressures, and ionic conductivities.[24,25] Similar to MOFs, practically infinite number of ILs can be synthesized by changing the combinations of cations and anions. Thanks to their tunable properties, ILs have been widely utilized in synthesis,[26,27] catalysis,[28,29] and gas absorption and separation.[30,31] Recent studies have focused on incorporation of ILs into MOFs[32] or coating the external surface area of MOFs with ILs to make IL/MOF composites,[33] which offer significantly improved gas adsorption and/or separation performance compared to that of the host MOF.

IL/MOF composites are a new type of composite materials which are used for various applications,[34,35] mainly for adsorption-based CO_2 separation.[32,33,36,37] Combining the high porosity and the high surface area of MOFs with high gas solubility of ILs, these composites offer a great potential for efficient gas storage and gas separation.[38] However, it is not possible to experimentally synthesize and test every single IL/MOF composite for a desired application, because of the infinite number of possible IL/MOF pairs. Molecular simulations have been very useful to screen large numbers of materials and to identify the best ones for a target application. They have been widely used to accurately predict gas storage and separation performances of MOFs.[39,40] Similarly, molecular simulation methods have been used for screening ILs for absorption-based gas separations.[41] However, there are only a handful of molecular simulation studies that investigated IL/MOF composites for gas storage and separation as we discuss in Chapter 2. In order to have a comprehensive understanding of IL/MOF composites, various types of materials should be investigated so that molecular

simulations can be validated by comparing with the experiments and then these molecular simulations can be used for high-throughput screening of new IL/MOF composites for which the experimental data are not available. In this way, IL/MOF composites that offer high selectivities for gas separations can be accurately and effectively identified by molecular simulations and then the experimental efforts, time, and resources can be directed towards the investigation of the most promising materials.

To this end, in the first chapter of this thesis, we proposed a computational methodology to predict the CO_2, CH_4 and N_2 adsorption and separation properties of IL/CuBTC composites. We performed GCMC simulations to predict CO_2, CH_4, and N_2 adsorption in seven different IL/CuBTC composites consisting of ILs with the $[BMIM]^+$ cation and a commonly used, commercial MOF, CuBTC. We compared simulation results with the experimental gas uptake measurements of these composites to propose a computational screening approach that is applicable to various IL/CuBTC composites. This approach was then tested on two new IL/CuBTC composites which have not been synthesized before to unlock their gas adsorption and separation performances. We showed the transferability of our computational methodology to these two new IL/CuBTC composites by synthesizing and characterizing them and comparing the experimentally measured gas adsorption data with the simulations. In the second part, the computational methodology was used to predict CO_2 and N_2 adsorption and separation in 1108 different [BMIM][BF_4]/MOF composites. First, the methodology was validated using three [BMIM][BF_4]/MOF composites, one of which, [BMIM][BF_4]/UiO-66, was prepared and characterized in detail for the first time in the literature. Then, CO_2/N_2 adsorption and separation performance of 1108 [BMIM][BF_4]/MOF composites were characterized using various adsorption performance metrics such as selectivity, working capacity, percent regeneration and adsorption performance score. Then, correlation between the weight percent IL loading of these composites and the increase in their CO_2/N_2 adsorption and separation performance is examined. Finally, relationships between changes in pore limiting

diameter and porosity upon IL-incorporation and the increase in gas adsorption and separation performance of MOFs upon IL-incorporation were investigated.

In Chapter 2, a detailed literature review about the IL/MOF composites and the studies including molecular simulations of IL/MOF composites were given. In Chapter 3, computational and experimental methods used in this thesis were explained. In Chapter 4, a computational method for the molecular simulations of IL/CuBTC composites was proposed and validated using two new IL/CuBTC composites. The results presented in Chapter 4 were published in *Chemical Engineering Journal.* In Chapter 5, proposed computational methodology was applied on 1108 [BMIM][BF_4]/MOF composite to discover the potential of IL/MOF composites in CO_2/N_2 separation. In the last chapter, results of this thesis and opportunities for future studies were summarized.

Chapter 2: Literature Review*

In this chapter, first, the literature about experimental gas adsorption and separation studies of IL/MOF composites was summarized. Then, molecular simulation studies that investigated IL/MOF composites were explained.

2.1 Experimental Studies of IL/MOF Composites for Gas Adsorption and Separation

In this section, experimental studies that investigated IL/MOF composites for gas adsorption and separation is summarized. Our group[42] investigated 1-*n*-butyl-3-methylimidazolium tetrafluoroborate ([BMIM][BF_4])-incorporated CuBTC and showed that the resulting composite material is more selective towards CH_4 over CO_2, N_2 and H_2. Our group also investigated six different IL/CuBTC composites where ILs are composed of 1-*n*-butyl-3-methylimidazole ($[BMIM]^+$) cation and different anions and found that interionic interaction energy of bulk ILs, which is determined by stretching vibration of second carbon atom of imidazolium ring and hydrogen (ν(C2H)) can be used to determine the CO_2 adsorption performance and thermal stability limit of IL/CuBTC composite.[43] In another study,[44] it was shown that CO_2/N_2:15/85 selectivity of CuBTC is increased by 37 and 34% upon 1-*n*-butyl-2,3-dimethylimidazolium hexafluorophosphate ([BMMIM][PF_6]) and 1-*n*-butyl-3-methylimidazolium hexafluorophosphate ([BMIM][PF_6]) incorporation, respectively, while CO_2/CH_4:50/50 selectivity is enhanced by 60 and 50% upon [BMMIM][PF_6] and [BMIM][PF_6]

* Some of the literature review given in this chapter were published in Chemical Engineering Journal with following reference: Polat, H. M.; Zeeshan, M.; Uzun, A.; Keskin, S, Unlocking CO_2 separation performance of ionic liquid/CuBTC composites: Combining experiments with molecular simulations. Chemical Engineering Journal, **2019**, *373*, 1179-1189. This chapter is the reformatted version of the mentioned paper.

incorporation, respectively. Lei et al.[45] used another approach on IL/MOF composites and suspended ZIF-8 particles in two ILs, 1-*n*-octyl-3-methylimidazolium bis(trifluoromethanesulfonyl)imide ([OMIM][NTf_2]) and 1-*n*-octyl-3-methylimidazolium hexafluorophosphate ([OMIM][PF_6]). They showed that CO_2 solubilities of the ILs were increased upon the addition of ZIF-8 particles via a coupling effect between adsorption and absorption. In another study,[46] 1-*n*-butyl-3-methylimidazolium thiocyanate ([BMIM][SCN]) was incorporated into ZIF-8. It was shown that [BMIM][SCN]/ZIF-8 have 2.6-times and 4-times higher selectivity towards CO_2 over CH_4 and N_2, respectively, when compared to pristine ZIF-8. Mohamedali et al.[37] incorporated ZIF-8 with 1-ethyl-3-methylimidazolium acetate ([EMIM][OAc]) and 1-*n*-butyl-3-methylimidazolium acetate ([BMIM][OAc]). They showed that [BMIM][OAc]/ZIF-8 composite have 7-times higher CO_2 capacity at 0.1 bar and 30 °C than that of pristine ZIF-8 and [EMIM][OAc]/ZIF-8 composite have 18-times higher CO_2/N_2 selectivity at 0.1 bar and 50 °C. Our group also used another approach and deposited 1-(2-hydroxyethyl)-3-methylimidazolium dicyanamide ([HEMIM][DCA]) on the surface of ZIF-8.[33] The resulting core-shell type composite material showed 45-times higher selectivity towards CO_2 over CH_4. We investigated 1-*n*-butyl-3-methylimidazolium methylsulfate ([BMIM][$MeSO_4$])/MIL-53(Al) composite and showed that CO_2/CH_4 and CO_2/N_2 selectivities increased by two- and three-times, respectively, upon [BMIM][$MeSO_4$]-incorporation into MIL-53(Al).[47] We also showed that incorporating ILs with smaller anions causes higher increase in CO_2 selectivity over CH_4 and N_2 when compared with the incorporation of ILs with bulky anions by investigating five IL/MIL-53(Al) composites where ILs were composed of $[BMIM]^+$ cation and different anions.[48]

2.2 Molecular Simulation Studies of IL/MOF Composites for Gas Adsorption and Separation

In this section, molecular simulation studies that investigated IL/MOF composites for gas adsorption and separation applications is summarized. Chen et al.[49] performed a

molecular simulation study for an IL/MOF composite, [BMIM][PF_6]/IRMOF-1, and showed that the composite is more selective for CO_2 over N_2 than the pristine IRMOF-1 using grand canonical Monte Carlo (GCMC) simulations. Vicent-Luna et al.[50] used GCMC simulations to show that incorporation of ILs significantly increases the CO_2 uptake of CuBTC at low pressures, whereas changes in CH_4 and N_2 uptakes are negligible. Li et al.[51] performed GCMC simulations and showed that IL impregnation into Cu-TDPAT increases the selectivity of H_2S over CH_4 with increasing IL loading. Xue et al.[52] investigated both IL/MOF and IL/covalent organic frameworks (COFs) composites using GCMC and molecular dynamics (MD) simulations and reported that better IL dispersion inside the pores results in better selectivity of CO_2 over CH_4 and N_2. Vicent-Luna et al.[53] showed that small additions of ILs into COFs significantly increase their CO_2/CH_4 selectivity compared to the hydrated COFs. The same group[54] also examined 1-ethyl-3-methylimidazolium thiocyanate ([EMIM][SCN]) incorporated IRMOF-1, HMOF-1, MIL-47, and MOF-1 using density functional theory (DFT) calculations, GCMC, and MD simulations; and reported that CO_2/CH_4, CO_2/N_2, and CH_4/N_2 selectivities of the composites increase with increasing IL loading. Gupta et al.[55] studied four different IL-incorporated IRMOF-1 composites for membrane-based separation of CO_2 from flue gas using MD simulations and showed that [BMIM][SCN]/IRMOF-1 membrane can surpass the Robeson's upper bound. They also investigated [BMIM][SCN]/ZIF-71 and [BMIM][SCN]/ZMOF composites using MD simulations and concluded that CO_2/N_2 selectivity of the composite in membrane-based separation is dominated by the adsorption selectivity.[56] The first high-throughput screening study was done by Lan et al.[57] using CBMC and GCMC simulations. They incorporated two ILs, 1,3-dimethylimidazolium tetrafluoroborate ([MMIM][BF_4]) and 1-*n*-butyl-3-methylimidazolium bis(trifluoromethanesulfonyl)imide ([BMIM][NTf_2]), into 303991 hypothetical MOFs and investigated a total of 550357 IL/MOF composites. They showed that [MMIM][BF_4] IL in MOFs with sql topology form a wire-tube conformation and these composites show the highest increase in CO_2/CH_4 selectivity. All these computational studies have been very useful to predict the gas adsorption and

gas separation performances of several different IL/MOF composites; however, none of these studies, to the best of our knowledge, included experimentally measured gas adsorption data of the composites to compare with the simulation results.

We recently combined experiments and molecular simulations for an IL/MOF composite and presented the good agreement between experimental measurements and predictions of GCMC simulations for single-component adsorption isotherms of CO_2, CH_4, and N_2 in a [BMIM][PF6]/ZIF-8 composite.[32] It was shown that IL/ZIF-8 composite more than doubles the CO_2/CH_4 and CO_2/N_2 selectivities of pristine ZIF-8 at low pressures. A follow-up study combining experimental and computational work[36] focused on [BMIM][BF_4]/ZIF-8 composite and presented the good agreement between experiments and molecular simulations for the heat of adsorption values for CO_2, CH_4, and N_2 in the composite. The work also showed that CO_2/CH_4, CO_2/N_2, and CH_4/N_2 selectivities enhance at low pressures upon IL incorporation into ZIF-8. These combined experimental and computational studies investigated only two types of IL/MOF composites having the same MOF, ZIF-8.

Chapter 3: Methods

Computational and experimental methods used in this thesis are explained in this chapter. First part of the chapter shows the computational methods and the second part explains experimental methods in detail.

3.1. Computational Methods

We studied a total of nine different ILs in this work: 1-*n*-butyl-3-methylimidazolium tetrafluoroborate ([BMIM][BF_4]), 1-*n*-butyl-3-methylimidazolium trifluoromethanesulfonate ([BMIM][CF_3SO_3]), 1-*n*-butyl-3-methylimidazolium methylsulfate ([BMIM][$MeSO_4$]), 1-*n*-butyl-3-methylimidazolium methanesulfonate ([BMIM][$MeSO_3$]), 1-*n*-butyl-3-methylimidazolium hexafluorophosphate ([BMIM][PF_6]), 1-*n*-butyl-3-methylimidazolium hexafluoroantimonate ([BMIM][SbF_6]), 1-*n*-butyl-3-methylimidazolium octylsulfate ([BMIM][$OcSO_4$]), 1-*n*-butyl-3-methylimidazolium dicyanamide ([BMIM][DCA]), and 1-*n*-butyl-3-methylimidazolium dibutylphosphate ([BMIM][DBP]). Molecular structures of ILs are shown in Appendix A. The IL structures were optimized by using Gaussian 09 software. [58] Conformer search was done to obtain the energetically the most stable structures of the cation and the anions. The cation ($[BMIM]^+$) and the anions ($[BF_4]^-$, $[CF_3SO_3]^-$, $[MeSO_4]^-$, $[MeSO_3]^-$, $[PF_6]^-$, $[OcSO_4]^-$, $[DCA]^-$, and $[DBP]^-$) were optimized using the Becke's three parameter hybrid exchange functional[59] and the Lee-Yang-Parr correlation functional[60] (B3LYP) and by using the 6-31+G(d) basis set. $[SbF_6]^-$ anion was optimized using density Gauss double-zeta with polarization functions (DGDZVP) basis set.[61] In these calculations, the convergence was set to tight

criteria (10^{-8} on root-mean-square density matrix, 10^{-6} on maximum density matrix, and 10^{-6} on maximum energy). To find the energetically most stable structures, conformer search was performed for the anion-cation pairs by using the same parameters given above and considering different anion orientations around the cation. The most stable conformer for ILs, except for [BMIM][SbF_6], was then further optimized by using 6-311+G(2d,p) basis set to increase the calculation accuracy. Population analyses were carried out to calculate the partial charges using full Natural Bond Orbital (NBO) analysis with NBO version 3.1.[62,63] Optimized IL structures were then used in the GCMC and MD simulations of IL/MOF composites.

All GCMC and MD simulations were performed using the RASPA software.[64] In Chapter 4, molecular simulations were performed twice using two different generic force fields, Universal Force Field (UFF)[65] and Dreiding[66], for both CuBTC and IL/CuBTC composites. In Chapter 5, Dreiding force field is used for both pristine MOFs and IL/MOF composites. For metal atoms, the potential parameters were taken from the UFF since they are not available in the Dreiding. After comparing the predictions of simulations and experimental results, the force field that best represents the experimental gas uptake data of the composites was selected. Force field parameters used in molecular simulations can be found in Appendix A.

CO_2 was modeled using a three-site rigid model with Lennard-Jones (LJ) 12-6 potential, where locations of point charges were the center of each site.[67] CH_4 was modeled as a spherical single-site LJ 12-6 potential.[68] N_2 was modeled as a three-site molecule, where two sites were N atoms and the third one was at the center of mass with point charges.[69] Parameters used for gas molecules in molecular simulations are given in Appendix A. Cross-atomic force field parameters were calculated using the Lorentz-Berthelot mixing rules and intermolecular interactions were truncated at 12 Å. MOFs and ILs were considered as rigid structures during the simulations to save significant computational time. Since adsorbate molecules are relatively small compared to the pore size of CuBTC and IL/CuBTC composites as shown in Appendix

A, flexibility is expected to have a negligible effect on the simulated gas uptakes as previously shown in the literature.[70] The largest cavity diameters (LCDs) and pore limiting diameters (PLDs) of pristine MOFs and IL/MOF composites were calculated using Zeo++ software.[71] The Baker minimization method with NVT ensemble was used to incorporate ILs into MOFs, as implemented in the RASPA. In this method, a minimum energy configuration with all positive eigenvalues in Hessian matrix was obtained.[72] In chapter 4, we calculated the required number of IL molecules that will lead to 30 wt. % IL-loading in the composite to be consistent with the previous experimental works[42–44] using the mass of one unit cell of CuBTC and molar weight of ILs. An IL loading of 30 wt. % was reported to provide the highest selectivity of the composites without forming a muddy product as discussed in our previous work.[42] It should be noted that there may be deviations between the pre-determined IL loading (30 wt. %) and the actual loading reported in the experimental studies because some part of the IL may be lost on the glass container that is used for the preparation of composites.[32] The number of IL molecules incorporated into CuBTC and calculated IL loading for each composite for Chapter 4 are given in Appendix A. In Chapter 5, IL loading was set to 1 molecule IL per unit cell of MOF. ILs were inserted into the MOFs using three different GCMC moves, translation, rotation, and random translation. The energy minimization procedure was continued until the root-mean-square gradient and maximum gradient were smaller than 10^{-6}. CBMC simulations were performed using translation, rotation, regrowth of full molecule and regrowth of partial molecule moves They were carried out for 5×10^{5} cycles. In these simulations, crystal structure of CuBTC and its partial charges were taken from the RASPA.[64] For ZIF-8 and UiO-66, structures with CSD[73] refcodes of FAWCEN01 and RUBTAK was used, respectively, and partial charges were assigned using charge equilibration (QEq) method as implemented in RASPA.[74] For ILs, point charges computed by DFT calculations were used. Both the atomic positions and point charges of ILs are given in Appendix A. Since incorporation of ILs into MOFs changes the electronic environment,[32,36,42] we reassigned the partial charges of IL/MOF structures using QEq method as implemented

in the RASPA and computed the electrostatic interactions between adsorbates having quadrupole moments (CO_2, N_2) and atoms of IL/MOF composites.

Single-component and binary mixture gas adsorption simulations of IL/CuBTC composites were performed in a pressure range of 0.1–10 bar at 25 °C in Chapter 4. The simulations were performed for adsorption (desorption) pressure of 1 (0.1) bar and 25 °C in Chapter 5 to mimic the conditions of vacuum swing adsorption process.[75] These simulations were carried out for 5×10^4 cycles for initialization and 5×10^5 cycles for taking the ensemble averages. In single-component GCMC simulations, four different types of moves, translation, rotation, reinsertion, and swap, were used. For the binary mixture GCMC simulations, an additional move, the identity exchange was also considered. The compositions of the mixtures were set as CO_2/CH_4:50/50, CO_2/N_2:15/85, and CH_4/N_2:50/50 to mimic the flue gas and natural gas separations. The Peng-Robinson equation of state was used to convert the pressure to fugacity. Pore volumes and void fractions of IL/MOF composites were calculated by using Zeo++[71] using a probe diameter of 0 Å and calculated void fractions were used in the GCMC simulations to convert the absolute gas uptakes to excess values to compare the results of simulations with those of the experiments. The experimental results of gas uptake measurements on [BMIM][BF_4]/CuBTC, [BMIM][CF_3SO_3]/CuBTC, [BMIM][$MeSO_4$]/CuBTC, [BMIM][$MeSO_3$]/CuBTC, [BMIM][SbF_6]/CuBTC, [BMIM][PF_6]/CuBTC, and [BMIM][$OcSO_4$]/CuBTC composites were taken from our previous publications.[42–44] We note that our previous article[44] on [BMIM][PF_6]/CuBTC reported CO_2, CH_4, and N_2 uptakes from 0.1 to 1 bar; however, here, we presented the gas uptakes from 0.1 to 10 bar for the same composite. Values of coefficient of determinations (R^2) were calculated using,

$$R^2 = 1 - \frac{\sum_0^{n-1}(y_i - \hat{y}_i)^2}{\sum_0^{n-1}(y_i - \bar{y})^2} \tag{3.1}$$

where y_i is the experimental value, $\hat{y}_i$ is the prediction from simulations, $\bar{y}$ is the arithmetic average of all experimental values and *n* is the number of data points, to quantify the goodness of prediction of simulations compared to the experimental data.

There are several different adsorbent performance metrics to compare the performance of adsorbents. In this thesis, selectivity (S), working capacity (ΔN), percent regenerability (R%) and adsorbent performance score (APS) was used as adsorbent selection metrics. They were calculated according to the equations shown in Table 3.1.

Table 3.1. Adsorbent selection metrics used in this thesis to evaluate the performance of pristine MOFs and IL/MOF composites

Parameter	Equation
Selectivity	$S_{CO_2/i} = \frac{x_{CO_2}/x_i}{y_{CO_2}/y_i}$
CO_2 Working Capacity	$\Delta N_{CO_2} = N_{ads} - N_{des}$
Percent Regenerability	$R\% = \frac{\Delta N_{CO_2}}{N_{ads,CO_2}} \times 100$
Adsorbent Performance Score	$APS = S_{ads,CO_2/i} \times \Delta N_{CO_2}$

* i is either CH_4 or N_2. ads: adsorption, des: desorption

Finally, MD simulations within NVT ensemble using Nose-Hoover thermostat[76,77] were performed to calculate the single-component self-diffusivity coefficient (D^0) of CO_2, CH_4, and N_2 in IL/CuBTC composites at infinite dilution. Gas-gas intermolecular interactions were switched-off to mimic the infinite dilution condition and 30 gas molecules were added inside the IL/CuBTC composites. MD simulations were performed by turning-off these interactions alternately to isolate the contributions of IL-gas and CuBTC-gas interactions. 1000 initialization and 10,000 equilibration cycles

were performed at the start of each simulation. MD simulations were performed for a total of 5 ns using a time step of 0.5 ps. Self-diffusion coefficients of gases were calculated from the slope of mean square displacement of the gas molecules obtained from the MD simulations.

3.2. Experimental Methods

3.2.1. Sample Preparation

In this work, three new IL/MOF composites, [BMIM][DCA]/CuBTC, [BMIM][DBP]/CuBTC and [BMIM][BF_4]/UiO-66 which have not been reported in the literature before, were synthesized. [BMIM][DCA] (>97%), [BMIM][DBP] (>96%), [BMIM][BF_4] (>97%) and CuBTC (Basolite C300) were purchased from Sigma Aldrich. UiO-66 was purchased from ACSYNAM, Canada. ILs and MOFs were stored in an Ar (>99.999%, Linde) glovebox (Labconco). We dried the ILs at 80 °C for 6 h and kept them under vacuum for 12 h before transferring them into the glovebox.[78] CuBTC and UiO-66 was activated overnight at 105 and 125 °C, respectively, under vacuum before usage. To prepare the samples with 30 wt. % IL loading, 0.3 g of [BMIM][DCA] or [BMIM][DBP] was dissolved in 20 mL of acetone (>99.8%, Merck) for 1 h. 0.7 g of CuBTC was then added into the solution and acetone was evaporated from the solution at 35 °C under atmospheric conditions. Muddy product from mostly evaporated solution was completely dried in the oven at 105 °C. Final product was stored in a desiccator until further usage. For the preparation of 3.34 wt. % IL-loaded sample, same procedure was used except 0.0334 g of IL and 0.967 g of UiO-66 were used.

3.2.2. Sample Characterization

3.2.2.1. X-ray Diffraction (XRD)

The XRD patterns of pristine CuBTC, UiO-66, [BMIM][DCA]/CuBTC, [BMIM][DBP]/CuBTC and [BMIM][BF_4]/UiO-66 were obtained by a Bruker D8 Advance X-ray Diffractometer using a Lynxeye detector equipped with a slit of 1 mm.

X-ray generator was set to 30 kV voltage and 10 mA current producing Cu Kα1 (1.5406 Å) radiation. The diffraction patterns were obtained between 2θ values of 5-50° with a resolution of 0.0204°.

3.2.2.2. Scanning Electron Microscopy (SEM)

SEM imaging was done using a Zeiss Ultra Plus Field Emission SEM (FESEM) with an accelerating voltage of 3 kV and working distance of approximately 4 mm. Materials were placed on a carbon tape attached on pin mount sample holder and coated with carbon to prevent charging during imaging.

3.2.2.3. Fourier Transform Infrared (FTIR) Spectroscopy

The infrared spectrum of CuBTC, UiO-66, [BMIM][DCA]/CuBTC, [BMIM][DBP]/CuBTC, [BMIM][BF_4]/UiO-66 and bulk ILs were obtained by using a Thermo Scientific Nicolet iS50 FTIR spectrometer equipped with an attenuated total reflection (ATR) cell. For background and sample, 64 and 512 scans were collected, respectively. The FTIR spectra of samples were collected between 400 and 4000 cm^{-1} with a spectral resolution of 2 cm^{-1}.

3.2.2.4. Brunauer-Emmett-Teller (BET) Surface Area

BET analyses were performed by using a Micromeritics ASAP 2020 physisorption analyzer. Approximately 200 mg of sample was used. Materials were activated at 125 °C under vacuum, then the samples were cooled down to −196 °C using liquid nitrogen before the analyses. The free space measurements were conducted using helium gas. N_2 gas adsorption isotherms of materials were obtained at −196 °C between 10^{-6} and 1 bar.

3.2.2.5 X-ray Fluorescence Spectroscopy (XRF)

A Bruker S8 Tiger XRF spectrometer was used for elemental analysis of [BMIM][BF_4]/UiO-66 composite. The analysis was performed under vacuum. A

rhodium anode was used in the X-ray generator and the generator was set to 4 kW. SpectraPlus Eval2 v.2.2.454 software was used for data analysis.

3.2.2.6. Thermogravimetric Analysis (TGA)

A TA Instruments Q500 thermogravimetric analyzer was used to determine the thermal stability limits of pristine CuBTC, UiO-66, [BMIM][DCA]/CuBTC, [BMIM][DBP]/CuBTC, [BMIM][BF_4]/UiO-66 and bulk ILs. An empty platinum pan was tared and approximately 15 mg of sample was placed on it. Then, a temperature ramp of 5 °C/min was applied until the temperature reached 125 °C. An isothermal treatment at 125 °C for 8 h was conducted to remove any moisture from the samples. After that, a temperature ramp of 2 °C/min was applied up to 700 °C. N_2 was used as balance and purge gas with flow rates of 40 and 60 mL/min, respectively. From the thermogravimetry (TG) and derivative TG curves, onset (T_{onset}) and derivative onset (T'_{onset}) temperatures obtained. T_{onset} generally overestimates the decomposition temperature, thus T'_{onset} was considered as decomposition temperature in this thesis.[32]

3.2.3. Gas Adsorption Measurements

CO_2, CH_4, and N_2 adsorption isotherms of pristine CuBTC, UiO-66, [BMIM][DCA]/CuBTC, [BMIM][DBP]/CuBTC and [BMIM][BF_4]/UiO-66 were obtained using a Micromeritics High Pressure Volumetric Analyzer II (HPVA-II-200). Before the measurements, approximately 350 mg of sample was activated at 125 °C under vacuum until the pressure inside the sample holder reaches to 10^{-6} bar. Then, the system was purged with He for three-times to eliminate the impurities and residuals from previous measurements. Temperature was set to 25 °C and held constant throughout the measurements, while the temperature of the laboratory was maintained at 23 °C. Gas adsorption isotherms were obtained in a pressure range of 0.1–10 bar.

Chapter 4: Unlocking CO_2 Separation Performance of Ionic Liquid/CuBTC Composites: Combining Experiments with Molecular Simulations[2]

In this chapter, a computational methodology to simulate CO_2 adsorption and separation of IL/CuBTC composites was proposed. This computational methodology was then validated using two new IL/CuBTC composites which have not been studied before. Also, CO_2/CH_4, CO_2/N_2 and CH_4/N_2 binary-mixture separation performances of IL/CuBTC composites were investigated. Finally, diffusion coefficients of CO_2, CH_4 and N_2 in pristine CuBTC and IL/CuBTC composites were computed using MD simulations. To the best of our knowledge, this is the first study that proposes a computational methodology for high-throughput screening of IL/CuBTC composites and confirms the validity of this methodology experimentally on new composites, presenting a broad potential for being expanded to other types of ILs and MOFs in the future.

4.1. Force Field Selection for Molecular Simulations of IL/CuBTC Composites

Adsorption of CO_2, CH_4, and N_2 in CuBTC has been widely studied in the literature using molecular simulations employing different force fields by several research groups.[79–83] We performed GCMC simulations using two different generic

[2] The results given in this chapter were published in Chemical Engineering Journal with following reference: Polat, H. M.; Zeeshan, M.; Uzun, A.; Keskin, S, Unlocking CO_2 separation performance of ionic liquid/CuBTC composites: Combining experiments with molecular simulations. Chemical Engineering Journal, **2019**, *373*, 1179-1189. This chapter is the reformatted version of the mentioned research paper.

force fields, UFF and Dreiding, to examine which force field provides a better representation of the experimental gas adsorption data in CuBTC. Figure 4.1(a) compares our experimental results of CO_2, CH_4, and N_2 uptakes in CuBTC with the predictions of GCMC simulations using UFF and Dreiding at a pressure range of 0.1–10 bar at room temperature. Based on the data presented in Figure 4.1, both force fields overestimated CO_2 and N_2 uptakes, whereas CH_4 uptakes were underestimated. For all gases at all pressures, predictions of UFF were found to be slightly higher than those of Dreiding. Figure 4.1(b) compares the experimental and simulated gas uptakes and the inset table shows the goodness of the agreement between them as quantified by the R^2 values. R^2 values were computed to be >0.9 for all gases except for N_2 when Dreiding force field was used. Once the overall prediction performances of the two force fields were considered for three gases at 16 different pressure points, R^2 values were computed as 0.980 for UFF and 0.975 for Dreiding, respectively, indicating that both generic force fields can be used to accurately estimate CO_2, CH_4, and N_2 uptakes of pristine CuBTC, which is consistent with the literature.[50,83]

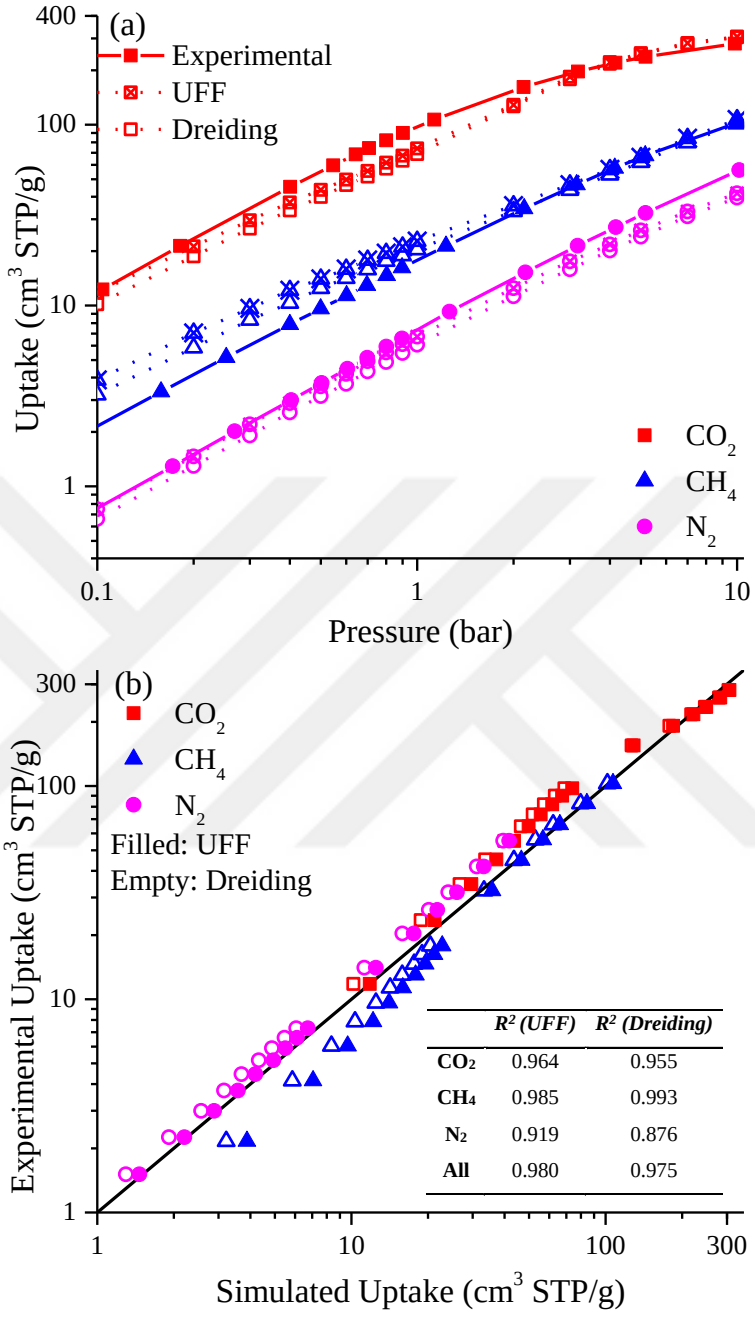

Figure 4.1. (a) Single-component adsorption isotherms of CO_2, CH_4, and N_2 as a function of pressure in pristine CuBTC, (b) comparison of experiments and simulations using UFF and Dreiding force fields for CuBTC.

After we validated the accuracy of molecular simulations for predicting CO_2, CH_4, and N_2 uptakes of pristine CuBTC, we applied the same computational approach to IL/CuBTC composites. We studied seven different IL/CuBTC composites, for which our group already has the experimental gas adsorption data for CO_2, CH_4, and N_2, as reported in our previous reports.[42–44] These IL/CuBTC composites are [BMIM][BF_4]/CuBTC, [BMIM][CF_3SO_3]/CuBTC, [BMIM][$MeSO_4$]/CuBTC, [BMIM][$MeSO_3$]/CuBTC, [BMIM][SbF_6]/CuBTC, [BMIM][PF_6]/CuBTC, and [BMIM][$OcSO_4$]/CuBTC. We performed molecular simulations for these composites and predicted their CO_2, CH_4, and N_2 uptakes between 0.1 and 10 bar at 25 °C. These GCMC simulations were performed by using both UFF and Dreiding to investigate which force field provides a better prediction for the gas uptake performances of the corresponding IL/CuBTC composite. Comparison of simulation results with the experimental gas uptake measurements are shown in Figure 4.2. Results indicate that simulations employing either of the force fields generally overestimate the experimental gas uptake values of all IL/CuBTC composites. Simulations using Dreiding force field tend to give a better agreement with the experiments than the ones using UFF. R^2 values were computed as 0.840, 0.734, and 0.913 for CO_2, CH_4, and N_2, respectively, when Dreiding was used in the molecular simulations, whereas UFF was found to result in much lower R^2 values (<0.6) for all gases. Overall, Figure 4.2 suggests that molecular simulations using Dreiding force field can provide reasonably accurate predictions for adsorption of CO_2, CH_4, and N_2 in these seven different IL/CuBTC composites at a wide pressure range.

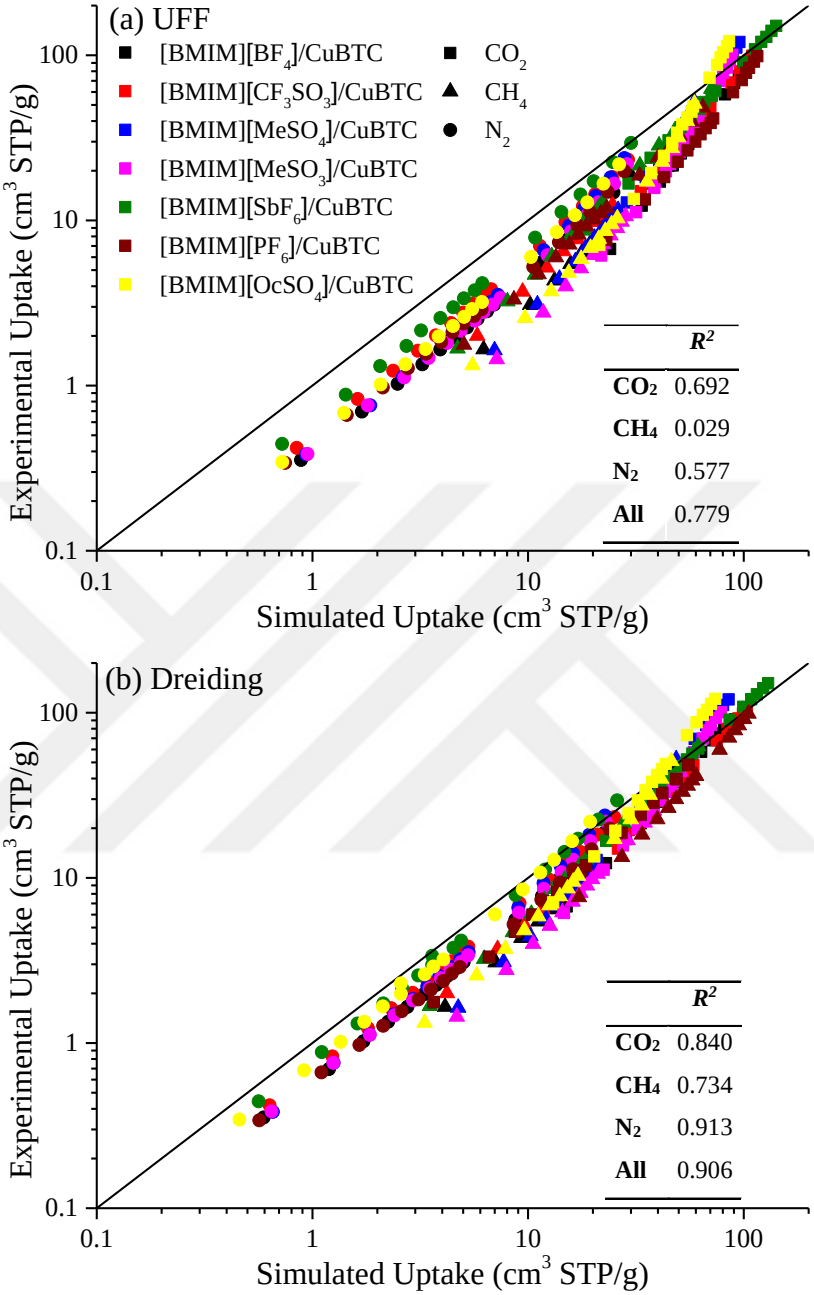

Figure 4.2. Comparison of experiments with simulations using (a) UFF and (b) Dreiding force fields for gas uptakes in seven different IL/CuBTC composites.

Correcting simulation results using a scaling factor has been previously done in several molecular simulation studies[84–89] to compensate the slight systematic deviations

between experiments and simulations, which generally results from the possible crystal defects, residual solvents, inaccessible adsorption sites of MOFs, or some specific interactions between MOFs and adsorbates that are not well represented by the generic force fields.[85,89–91] Thus, to improve the agreement between simulations and experiments, uptakes obtained from GCMC simulations were multiplied by a pressure dependent factor (s_i) as shown in equation 4.1,

$$s_i = A_i \times (\log(P) + 2) \quad (4.1)$$

where P is the pressure and A_i is the coefficient of scaling function changing with pressure range (defined for low pressure (<0.3 bar), moderate pressure (0.3-1 bar) and high pressure (>1 bar) regions) and gas species. The constant "2" was added to this factor to eliminate the possibility of zero multipliers at 0.1 and 1 bar pressures. We note that scaling factors do not have specific physical meanings, they were purely defined by fitting the simulation results to experiments. Table 4.1 lists the scaling factors that we defined for each of the pressure regions, low, moderate, and high pressure regions. The data of Figure 4.2 show that deviations between the experiments and simulations are much higher at lower pressures compared to the ones at higher pressure. Thus, the coefficients of the scaling function (A_i) show a decreasing trend with increasing pressure for all adsorbates (Table 4.1).

Table 4.1. Gas coefficients (A_i) in scaling factor for low pressure (LP), mid pressure (MP), and high pressure (HP).

	A_{LP} (<0.3 bar)	A_{MP} (0.3-1 bar)	A_{HP} (>1 bar)
CO_2	0.446	0.439	0.406
CH_4	0.332	0.302	0.299
N_2	0.465	0.362	0.318

Figure 4.3 compares the experimental gas uptakes of IL/MOF composites with the scaled simulations, which are in a much better agreement with the experimental data compared to the non-scaled ones. The inset table in Figure 4.3(d) shows the R^2 values for the scaled simulation results. Accordingly, the R2 values increased from 0.840 to 0.904 for CO_2, from 0.734 to 0.972 for CH_4, and from 0.913 to 0.970 for N_2 uptakes of seven different IL/MOF composites. The better agreement of simulations with experiments after scaling indicates that ideal selectivities, which were calculated as the ratio of single-component gas uptakes, can also be well-predicted by the simulations. Comparison of experimental and simulated ideal selectivities for CO_2/CH_4, CO_2/N_2, and CH_4/N_2 shown in Figure 4.4 present the good agreement between two. Overall, we showed that molecular simulations using Dreiding force field and the function that we introduced above to scale the simulated gas uptakes can be used to accurately estimate the gas uptake and separation performances of IL/CuBTC composites, where ILs are composed of $[BMIM]^+$ cation and different types of anions, which are not too big in size not to limit their transport into the pores.

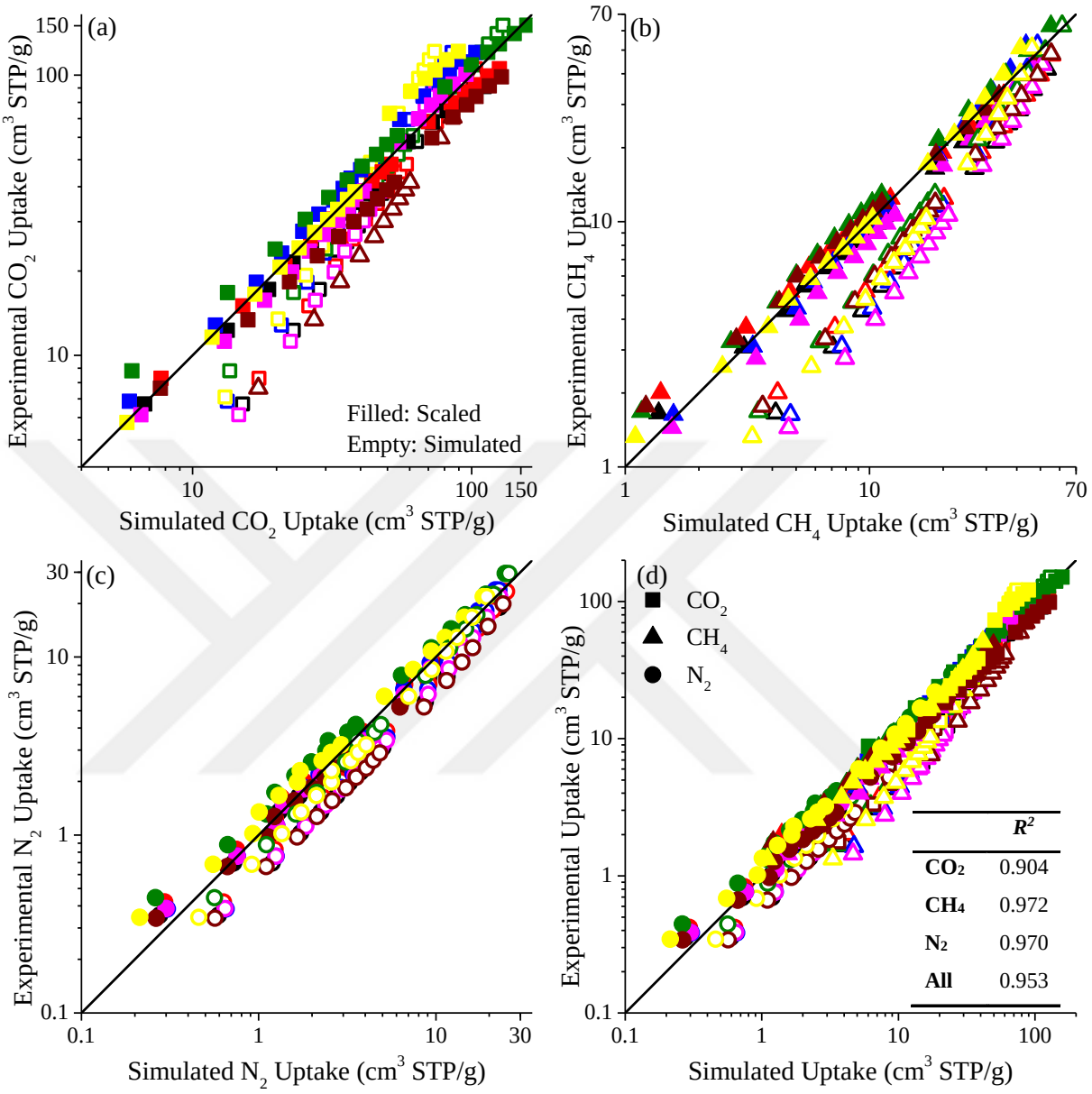

Figure 4.3. Comparison of scaled and unscaled simulations with experimental uptakes of (a) CO_2, (b) CH_4, (c) N_2, and (d) all gases. Filled (empty) symbols represent scaled (non-scaled) simulations. Color code follows that in Figure 4.2.

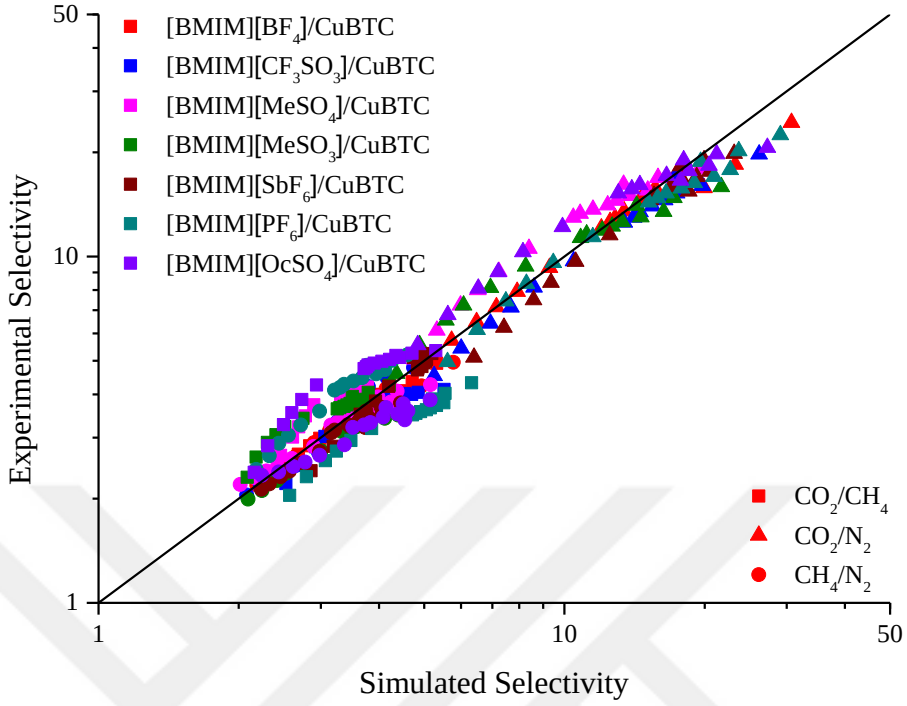

Figure 4.4. Comparison of experimental and simulated selectivities for 7 different IL/CuBTC composites.

4.2. Application of Computational Approach to Two Different IL/CuBTC Composites

The computational approach that we described above was developed and validated by using seven different IL/CuBTC composites for which our group already had the experimental gas adsorption data. Next, we performed GCMC simulations of CO_2, CH_4, and N_2 adsorptions on two new composites, [BMIM][DCA]/CuBTC and [BMIM][DBP]/CuBTC, to confirm the transferability of this approach to other IL/CuBTC composites. We note that these two composites have not been reported before in the literature. These two ILs were chosen as they are commonly available and we also aimed to select the anions of ILs in a way to represent a small ($[DCA]^-$) and a large anion ($[DBP]^-$). This approach let us to test the transferability of our computational approach to predict gas uptakes and selectivities of different IL/CuBTC

composites, where ILs are composed of the same $[BMIM]^+$ cation with different anions. We synthesized and characterized these two new composites and measured their gas uptake performances. Before focusing on the simulation results, we first discuss the characterization of these two new composites.

Figure 4.5(a) illustrates the XRD patterns of pristine CuBTC, [BMIM][DCA]/CuBTC, and [BMIM][DBP]/CuBTC composites. These results show that crystal structure of CuBTC was preserved upon IL incorporation. SEM images shown in Appendix B confirm that crystal size and shape do not change in the composite materials when compared with those of CuBTC. Figure 4.5(b) shows thermogravimetric curves of pristine CuBTC and the new composites. More detailed comparisons of TGA results of composites with their respective bulk ILs and pristine CuBTC are given in Appendix B. The derivative onset temperature (T'_{onset}) of pristine CuBTC was found as 324 °C. T'_{onset} of [BMIM][DCA]/CuBTC and [BMIM][DBP]/CuBTC were found as 254 °C and 178 °C, while bulk ILs, [BMIM][DCA] and [BMIM][DBP], were found to start to decompose at 226 °C and 228 °C, respectively. These changes in T'_{onset} values indicate the presence of direct interactions between CuBTC and ILs, which might be because of the slight structural alterations in the individual components of the composite. FTIR spectra of pristine CuBTC, bulk ILs, and composites are shown in Figure 4.5(c). Three intense peaks between 2100-2300 cm^{-1} in the spectrum of bulk [BMIM][DCA] were assigned to asymmetric stretching of –C≡N group (ν_{as}(–C≡N)), symmetric stretching of –C≡N group (ν_s(–C≡N)) and combination of these two modes.[92] In [BMIM][DCA]/CuBTC composite, ν_{as}(–C≡N) shifted from 2126 cm^{-1} to 2165 cm^{-1}, ν_s(–C≡N) shifted from 2191 cm^{-1} to 2212 cm^{-1} and the combination of these two modes shifted from 2229 cm^{-1} to 2285 cm^{-1}. Symmetric stretching deformation of second carbon of the imidazolium group and the proton bonded to it (ν_s(–C2H)) exhibited a red shift from 3101 cm^{-1} to 3086 cm^{-1}. Similar shifts in the position of bands were also seen in [BMIM][DBP]/CuBTC composite. After IL-incorporation, –P=O stretching vibration

[86] (ν_s(–P=O)) at 1233 cm^{-1} and ν_s(–C2H) at 3097 cm^{-1} shifted to 1239 cm^{-1} and 3093 cm^{-1}, respectively. These shifts in the positions of characteristic bands of ILs confirm the presence of direct interactions between CuBTC and incorporated ILs. Figure 4.5(d) shows the experimental adsorption isotherms of CO_2, CH_4, and N_2 between 0.1-10 bar for [BMIM][DCA]/CuBTC and [BMIM][DBP]/CuBTC at 25 °C. For both composites, uptakes for all three gases are lower than those of pristine CuBTC[44] at all pressure points. Comparison of experimental CO_2/CH_4, CO_2/N_2, and CH_4/N_2 selectivities of these new composites and those of the pristine CuBTC is shown in Appendix B. Data show that both composites offer improved gas separation performance especially at low pressures, consistent with the previous reports.[32,36,42,44]

Next, we washed the [BMIM][DCA]/CuBTC and [BMIM][DBP]/CuBTC composites with toluene to validate that the ILs were successfully incorporated into the pores of CuBTC. We chose toluene as it is larger than the pore openings of CuBTC so it cannot go into the pores and yet it is capable of dissolving both of these ILs at room temperature.[44] FTIR spectra of toluene, the filtrates of washing process, and the corresponding composites before and after washing are shown in Appendix B. Data showed that the spectra of the filtrates do not have any evident IL bands, while the spectra of the composites after washing showing the characteristic IL bands still present in the composites even after the washing experiment. These results confirmed that the incorporation of ILs into the pores was successful for both composites. N_2 adsorption at -196 °C for two composites were shown in Appendix B. It shows that N_2 adsorption at -196 °C is quite different for two composites although their CO_2, CH_4, and N_2 adsorption isotherms at room temperature are similar (Figure 4.5(d)), which may be attributed to the low solubility of N_2 in ILs at -196 °C rendering the BET method unreliable for this type of materials.[43]

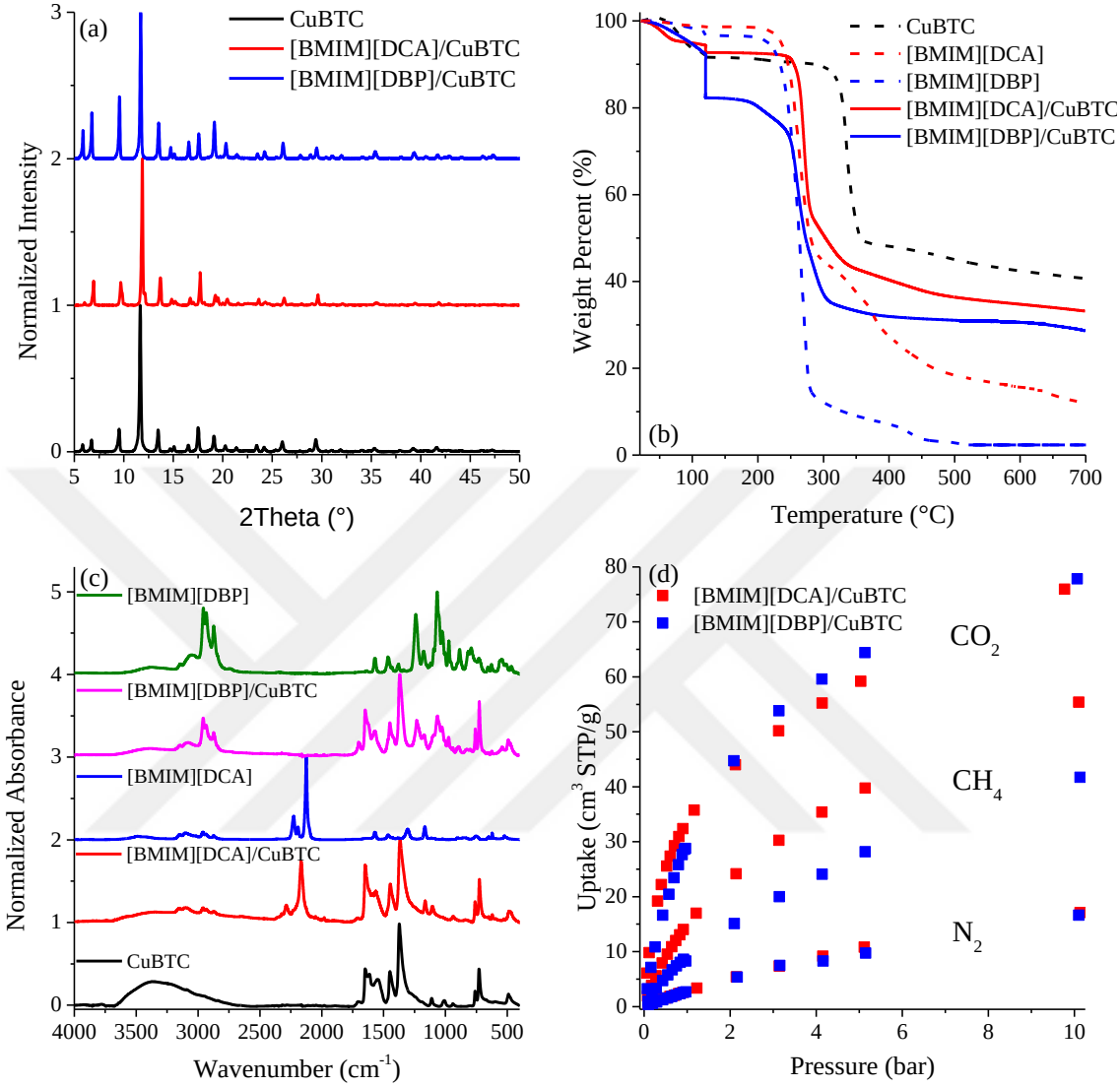

Figure 4.5. (a) XRD patterns, (b) TGA curves of CuBTC, [BMIM][DCA]/CuBTC, [BMIM][DBP]/CuBTC, and bulk ILs, (c) FTIR spectra of CuBTC, [BMIM][DCA]/CuBTC, [BMIM][DBP]/CuBTC, and bulk ILs, (d) CO_2, CH_4, and N_2 adsorption isotherms of [BMIM][DCA]/CuBTC and [BMIM][DBP]/CuBTC.

Results of GCMC simulations for [BMIM][DCA]/CuBTC and [BMIM][DBP]/CuBTC composites were scaled using the same function as described in

equation 4.1 and Table 4.1. Figure 4.6(a) shows the good agreement between experiments and simulations. CO_2, CH_4, and N_2 uptakes were estimated well by the scaled GCMC simulations leading to R^2 values of 0.951, 0.897, and 0.964, respectively, while the raw GCMC simulation results have the corresponding R^2 values of 0.888, 0.873, and 0.805, respectively. Predicted ideal CO_2/CH_4, CO_2/N2, and CH_4/N_2 selectivities of [BMIM][DCA]/CuBTC and [BMIM][DBP]/CuBTC were also in a reasonable agreement with the experimental selectivities as shown in Figure 4.7. For example, experimental CO_2/N_2 selectivities vary between 4.5 and 16 at 0.5–10 bar, whereas simulations predicted these values as between 4.3 and 14.7. The experimental values for the ideal CO_2/CH_4 selectivity were between 1.4 and 3.5 at the same pressure range and the simulations estimated this selectivity as between 2 and 3.6.

We finally discuss the validity of the assumptions used to predict the gas adsorption properties of IL/CuBTC composites in this work. We considered CuBTC as a perfect crystal without defects in our molecular simulations. CuBTC we used in the experiments may have defects which may explain the overestimation of experimental gas uptake results by the GCMC simulations. Atomic positions of ILs in CuBTC were predicted with MD simulations in this work to save computational time in calculating the positions of 12 to 20 IL molecules inside a unit cell of MOF having 624 atoms but this is a rough estimation and quantum chemical/mechanical calculations are required for more accurate positions of ILs incorporated into MOFs. Finally, we used generic force fields which do not consider the specific chemical interactions[85,89–91] between IL and CuBTC, but previous experimental studies[32,36,42] suggested that IL incorporation may be changing not only the structure of the ILs, but also the electronic structure of the gas adsorption sites in MOFs. We attempted to use a generic force field to enable the transferability of our computational approach to various IL/MOF composites for high-throughput computational screening. Overall, these assumptions allowed us to provide an efficient computational approach, validated by experiments, which can quickly estimate the gas adsorption behavior in IL/CuBTC composites at a minimal

computational expense, opening up opportunities for high-throughput screening studies on these novel materials.

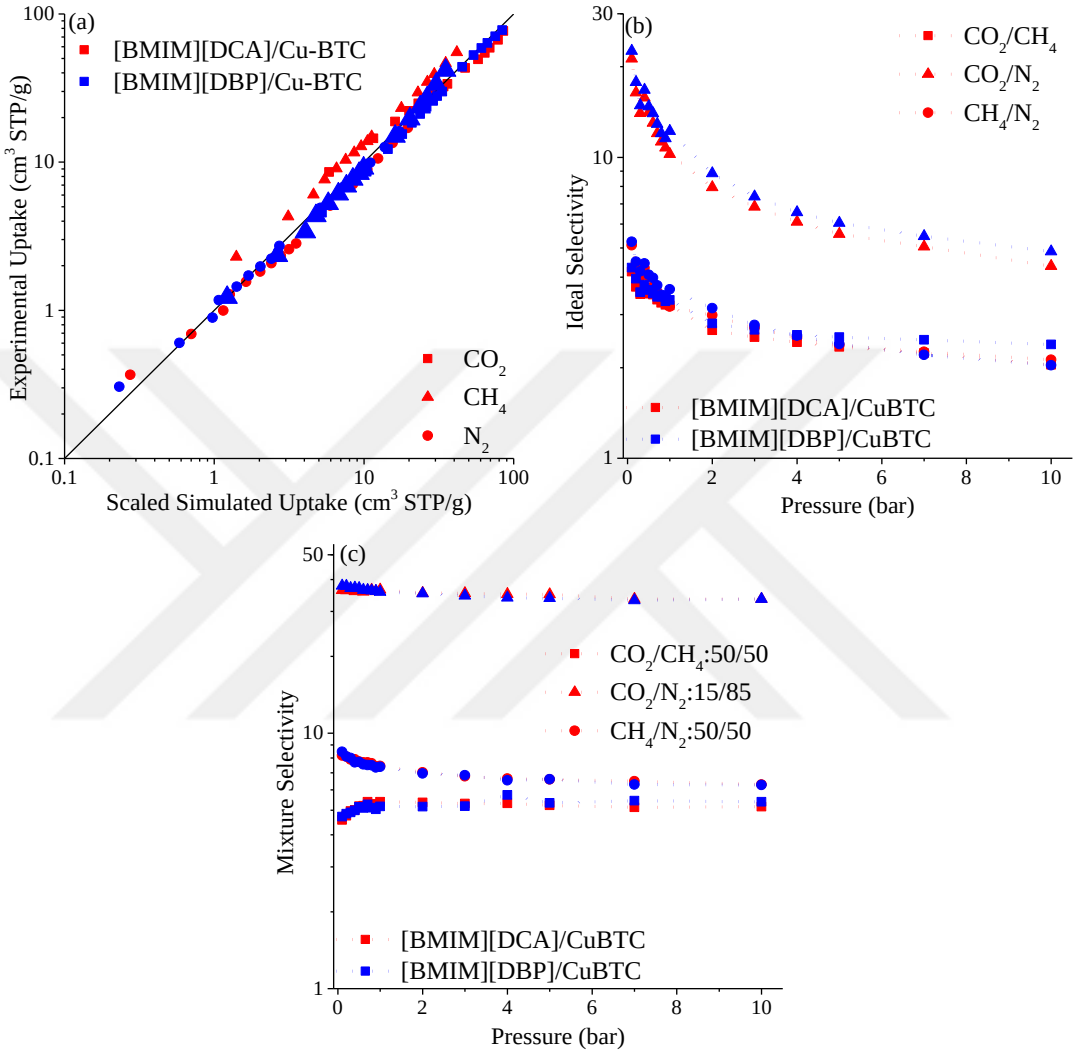

Figure 4.6. (a) Comparison of scaled simulation results and experimental uptakes for [BMIM][DCA]/CuBTC and [BMIM][DBP]/CuBTC composites, (b) ideal and (c) mixture selectivities of two composites calculated from GCMC simulations. The first component in the label indicates the selected one over the other.

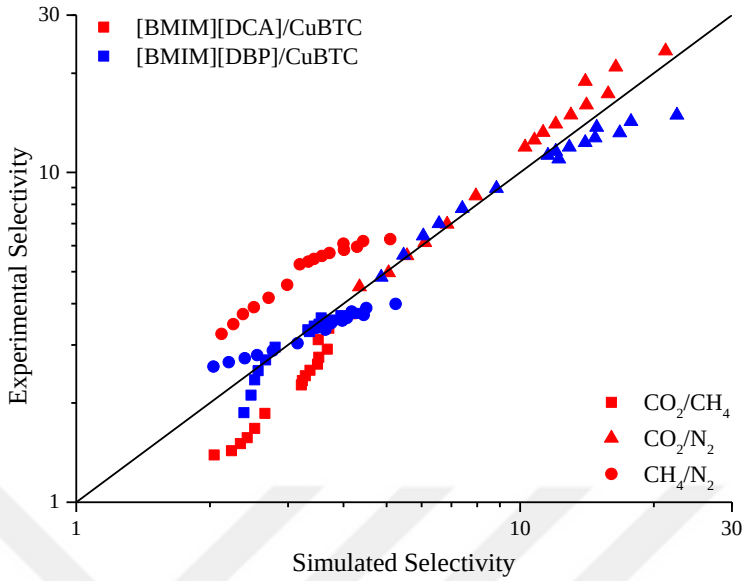

Figure 4.7. Comparison of experimental and simulated selectivities of [BMIM][DCA]/CuBTC and [BMIM][DBP]/CuBTC composites.

4.3. Gas Mixture Separation Performances of IL/CuBTC Composites

We also performed GCMC simulations considering CO_2/CH_4:50/50, CO_2/N_2:15/85, and CH_4/N_2:50/50 mixtures, which have industrial and environmental significance, at 0.1–10 bar to provide a more realistic gas separation performance analysis for all nine IL/CuBTC composites considered in this chapter. Figures 4.6 (b) and (c) demonstrate the ideal and mixture selectivities of [BMIM][DCA]/CuBTC and [BMIM][DBP]/CuBTC computed from GCMC simulations, respectively. Experimental CO_2/CH_4, CO_2/N_2, and CH_4/N_2 selectivities and the corresponding mixture selectivities calculated by using the Ideal Adsorbed Solution Theory (IAST)[93] is shown in Appendix B. Dual-site Langmuir fits were also shown in Appendix B with their corresponding parameters. Mixture selectivities in both cases were found to be higher than the ideal selectivities as expected because of the competition between the gas molecules for the same adsorption sites.[94–97] Ideal selectivities of the two new composites were computed

to vary between 2.1–4.3 for CO_2/CH_4 and 4.3–22.6 for CO_2/N_2 in a pressure range of 0.1–10 bar, while they were between 3 and 4.1 and 7.7–15.4, respectively, for pristine CuBTC. As we showed in our previous studies,[32,36,42] ILs act as additional interaction sites for adsorbate molecules at low pressures. Increase in CO_2 uptake because of the presence of these additional adsorption sites is higher than that of CH_4 and N_2, which leads to an increase in CO_2/CH_4 and CO_2/N_2 selectivities of composites at low pressures. However, at high pressures, available pore space for gas species becomes more dominant than the intermolecular interactions in determining the gas uptake performance, and thus, the selectivities decrease.

The comparison of mixture selectivities of all nine IL/CuBTC composites that we examined in this work with those of pristine CuBTC is given in Figure 4.8. CO_2/CH_4:50/50, CO_2/N_2:15/85, and CH_4/N_2:50/50 mixture selectivities of all composites are higher than those of pristine CuBTC at all pressures except between 7 and 10 bar for CO_2/CH_4. At 0.1 bar, mixture selectivities of IL/CuBTC composites vary between 4.1–6.1, 31.5–44.7, and 6.5–8.5 for CO_2/CH_4, CO_2/N_2, and CH_4/N_2, respectively, while pristine CuBTC has a selectivity of 3.4, 15.7, and 4.9 for CO_2/CH_4, CO_2/N_2, and CH_4/N_2, respectively. These results suggest that IL/CuBTC composites that we examined in this work have a strong potential in separation of gas mixtures, especially for CO_2 separation from natural gas and flue gas. Using this computational approach, promising IL/MOF composites offering high selectivity for a desired gas separation can be identified among many possible candidates and the experimental efforts can then be focused on the synthesis and testing of these promising candidates.

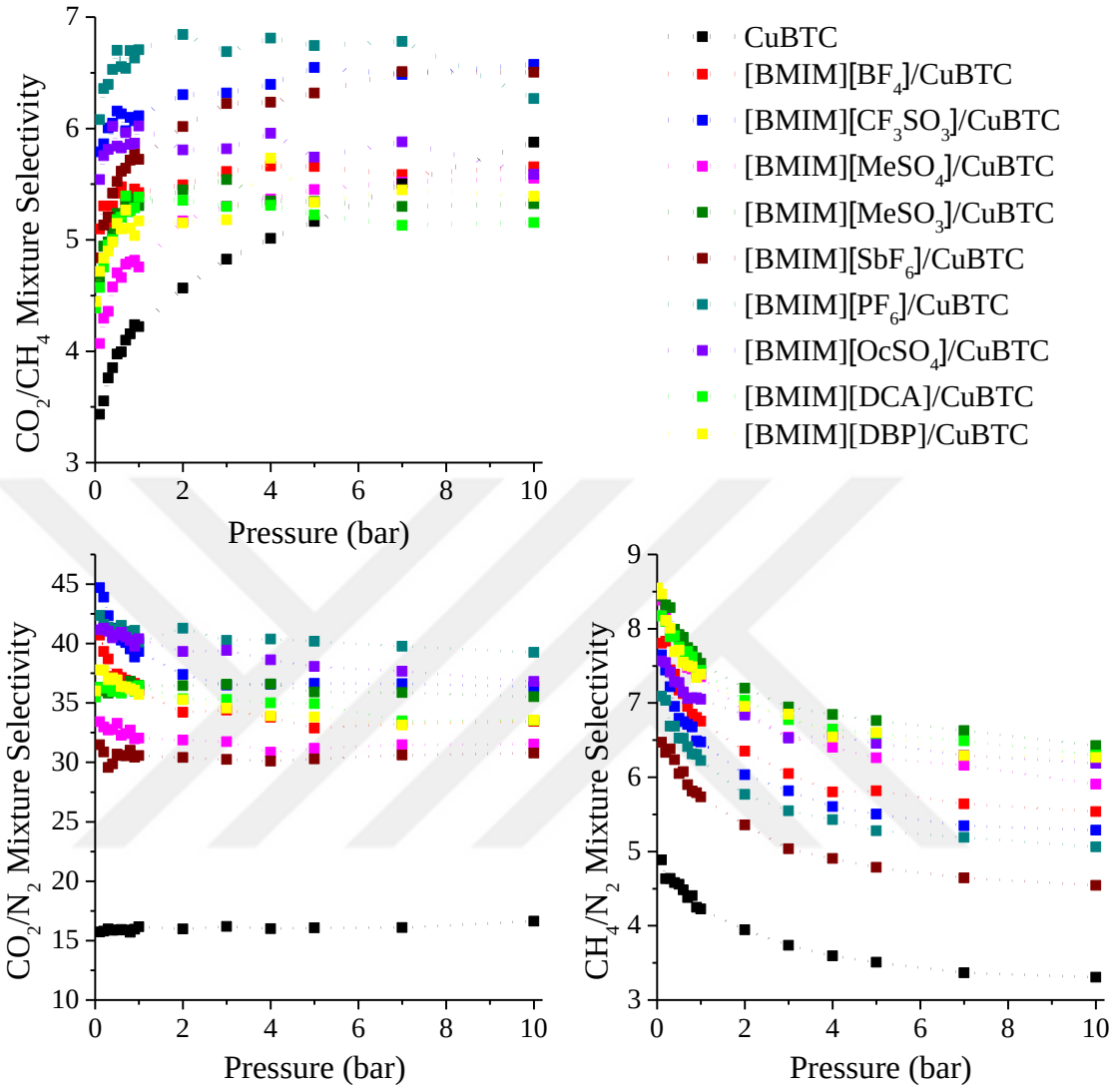

Figure 4.8. CO_2/CH_4:50/50, CO_2/N_2:15/85, and CH_4/N_2:50/50 mixture selectivities calculated by GCMC simulations as a function of pressure for pristine CuBTC and IL/CuBTC composites.

4.4. Gas Diffusion in IL/CuBTC Composites

We so far examined the gas adsorption in IL/CuBTC composites. Kinetic properties of gases inside the pores of an adsorbent material are also important because

slow diffusion due to the strong host-guest interactions can be a bottleneck in the adsorption processes.[98] To have an understanding on the gas transport inside the IL/CuBTC composites, MD simulations were performed and self-diffusivities of gases (D^0) in each IL/CuBTC composite were computed at infinite dilution. We specifically examined D^0 values in three cases to assess the effects of interactions between adsorbates and CuBTC and the ones between adsorbates and ILs: (i) only IL-gas interactions were considered, (ii) only CuBTC-gas interactions were considered, and (iii) both IL-gas and CuBTC-gas interactions were considered. Figure 4.9 shows that D^0 of CO_2 is the lowest in all composites, 1.05×10^{-6}–1.34×10^{-5} cm^2/s, followed by CH_4 and N_2. This is expected as CO_2 has stronger interactions with the composite than CH_4 and N_2 have, leading to higher uptakes under the same conditions. Because of its stronger adsorption, it diffuses slower than the other gas components. D^0 values range between 1.21×10^{-6}–1.45×10^{-5} cm^2/s and 3.3×10^{-6}–3.76×10^{-5} cm^2/s for CH_4 and N_2, respectively. According to results presented in Figures 4.9(a-c), D^0 values of all gases are the highest in case (i) than the ones in case (ii) for all IL/MOF composites, indicating that IL-gas interactions are weaker than the CuBTC-gas interactions because of the significantly larger number of interaction sites in CuBTC compared to IL molecules. Once both interactions were taken into account as in the case of (iii), gas molecules are strongly adsorbed and diffusivities become the lowest. Figure 4.9(d) shows that D^0 values of gases in all IL/CuBTC composites are lower than those of pristine CuBTC, since IL molecules incorporated inside the pores of CuBTC decrease the pore volume of the material and hinder the gas mobility inside the cages. Among the IL/MOF composites we examined, [BMIM][SbF_6]/CuBTC has the highest gas diffusivities as it has the highest pore volume. We note that several factors other than the pore volume such as different chemical and physical properties of the anion of ILs may lead to differences in molecular interactions between gas molecules and IL molecules, which can be a major factor in determining the gas diffusivity.[99,100]

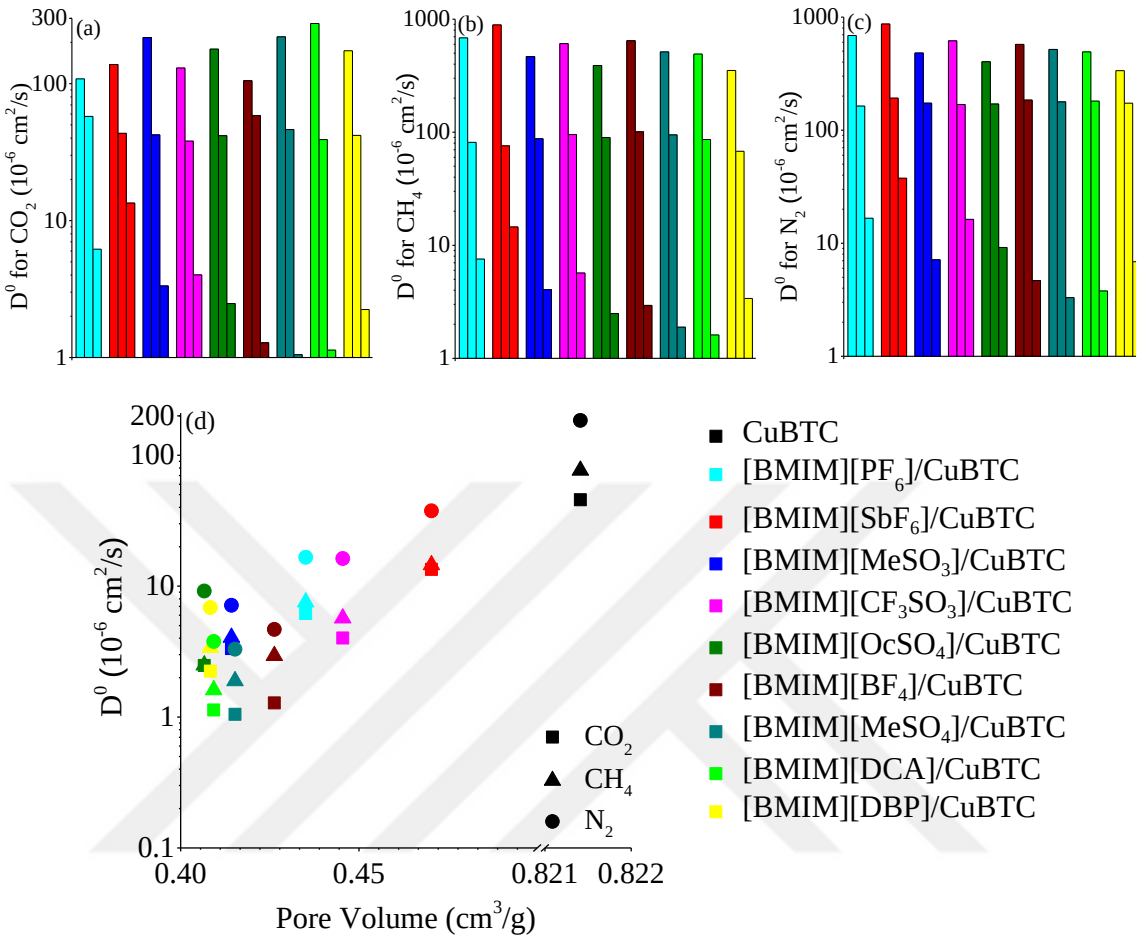

Figure 4.9. D^0 values for (a) CO_2, (b) CH_4, and (c) N_2 in IL/CuBTC composites. For (a-c), IL-gas (CuBTC-gas) interactions are considered in the first (second) column. All interactions are considered in the third column. (d) Variation of D^0 values of CO_2, CH_4, and N_2 with respect to pore volume of IL/CuBTC composites and pristine CuBTC.

Finally, we compared our simulated self-diffusion coefficients of gases in pristine CuBTC and IL/CuBTC composites with other available experimental and simulation studies. Experimental self-diffusion coefficient of CO_2 in CuBTC was reported as 1.7×10^{-5} cm^2/s at 0.5 vol% gas phase concentration of CO_2 in He at 1 bar at room temperature.[101] Schlayer et al.[102] measured self-diffusion coefficient of CH_4 in

commercial CuBTC as 5.8×10^{-5} cm^2/s for 15 mg of CH_4/g of CuBTC at room temperature. Gutiérrez-Sevillano et al.[103] simulated CO_2/CH_4:50/50 mixture in pristine CuBTC and calculated diffusion coefficients of CH_4 and CO_2 at 0.1 bar at room temperature as 1.2×10^{-4} and 4×10^{-5} cm^2/s, respectively, without changing much with composition of the mixture. Our simulated self-diffusion coefficients for CH_4 and CO_2 were 7.7×10^{-5} and 4.6×10^{-5} cm^2/s, respectively, for pristine CuBTC at infinite dilution and these values were found to be consistent with the literature values listed above. Vicent-Luna et al.[54] calculated diffusion coefficients for CO_2 and CH_4 for [EMIM][SCN] incorporated IRMOF-1, MIL-47, MOF-1, and HMOF-1 at 1 bar at room temperature. The self-diffusion coefficients of CH_4 and CO_2 were reported to be between 5×10^{-6}-10^{-5} cm^2/s and 10^{-6}-7×10^{-6} cm^2/s, respectively, in 25 vol.% IL incorporated MIL-47, 40 vol.% IL incorporated MOF-1, and 35 vol.% IL incorporated HMOF-1, which have similar pore volumes (0.41-0.48 cm^3/g) with the composites we studied in this work. Corresponding values were found to vary between 1.2×10^{-6}-1.5×10^{-5} cm^2/s for CH_4 and 10^{-6}-1.3×10^{-5} cm^2/s for CO_2 at infinite dilution in this chapter. We note that one may expect higher rate of gas transport at infinite dilution but the similarities of diffusivities between the reported work and ours can be explained with the longer chain of $[BMIM]^+$ than $[EMIM]^+$ and larger anions that we studied than linear $[SCN]^-$, which all hinder the gas transport inside the cages.

Chapter 5: High-throughput Computational Screening of [BMIM][BF_4]/MOF Composites for CO_2 Separation from Flue Gas

To expand the information we have about IL/MOF composites and to discover their potential in CO_2 adsorption and separation applications, the computational methodology that we described and validated in the previous chapter was used to simulate numerous MOFs from the CSD database. In this chapter, the effect of a commercial IL, [BMIM][BF_4], on the CO_2 and N_2 adsorption and separation performance of different MOFs are investigated. Molecular simulations were carried out to identify the best [BMIM][BF_4]/MOF couples. Further investigation was done by correlating some of the important physical properties of IL/MOF composites with their CO_2 adsorption and separation performance. The information gathered for this chapter can be used to extrapolate IL/MOF composites that have high performance of CO_2 separation and adsorption.

5.1. Selection of IL, MOFs and IL-incorporation Method

There are 9 different IL candidates that we validated our methodology as accurate to simulate CO_2 separation performance of IL/CuBTC composites in the previous chapter. Among them, we chose [BMIM][BF_4] because it is one of the smallest ILs in the list and one of the most investigated ILs in the literature. The list of MOFs was taken from the previous works of our group[39] where 3816 MOFs were filtered with a criterion of PLD > 3.8 Å from 54808 non-disordered MOFs within the CSD database. We further refined that list into 1108 MOFs by discarding the structures that have PLDs lower than 6 Å. It should be noted that 6 Å is the approximate value of the length

between the furthest fluorine atom in the anion and the furthest hydrogen atom in the cation of [BMIM][BF_4]. We have ensured the successful incorporation of IL molecules into the pores of MOFs by using this additional criterion.

There are two different methods to incorporate the IL molecules into MOFs in the literature. One of them is the Baker's minimization method that we used and validated in Chapter 4 of this thesis. The other one is used by Lan et.al,[57] called configurational-bias Monte Carlo (CBMC), was utilized for high-throughput screening of 550357 IL/MOF couples for CO_2/CH_4 adsorption and separation where MOFs were hypothetical. Before we start to perform large-scale computational screening of [BMIM][BF_4]/MOF composites for CO_2/N_2 adsorption and separation, first we would like to investigate the differences caused by these two incorporation methods on CO_2/N_2 adsorption and separation performance of IL/MOF composites. To this end, we incorporated CuBTC with 1 IL molecule/unit cell loading using 9 different ILs from Chapter 4 utilizing Baker's minimization and CBMC methods. Then, we calculated the CO_2/N_2:15/85 binary mixture adsorption of these IL/CuBTC composites at 0.1-10 bar pressure range to represent the vacuum swing adsorption process at 25 °C using GCMC simulations. Finally, we compared the data (total of 144 data points for each gas) that we acquired using the Baker's minimization and CBMC methods. Comparison of the simulation results are shown in Figure 5.1.

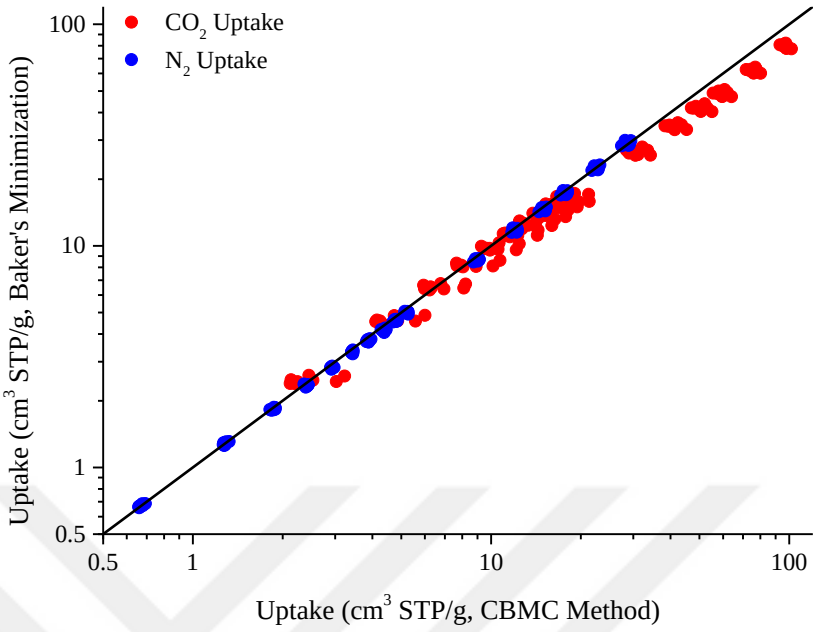

Figure 5.1. Comparison of CO_2 and N_2 uptakes simulated using the methodologies including Baker's minimization and CBMC for minimization of IL molecules.

Figure 5.1 shows that two methods of minimization do not have any significant differences on the adsorption of CO_2 and N_2 on the IL/CuBTC composites. R^2 values were calculated as 0.932 and 0.998 for CO_2 and N_2, respectively, showing that both methods result in similar uptakes for simulation of CO_2/N_2 adsorption of these materials. Although there is some difference in the high pressure regime for CO_2, both methods can be used with similar accuracy to simulate the CO_2/N_2 uptakes of IL/CuBTC composites. It is also important to compare selectivities to show the differences of two methods when it comes to prediction of CO_2 separation performance of these materials. Figure 5.2 shows comparison of CO_2/N_2 selectivities calculated from binary mixture GCMC simulations using Baker's minimization and CBMC.

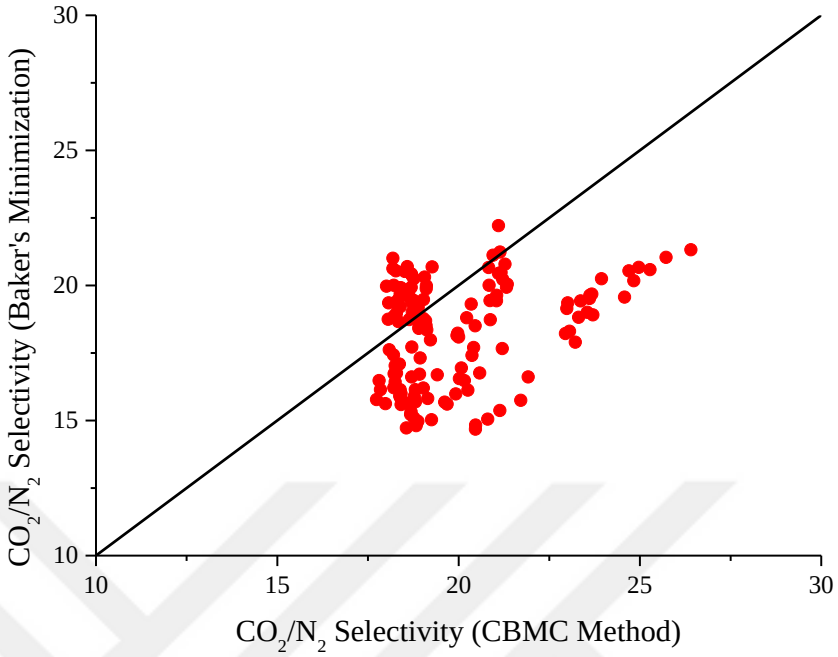

Figure 5.2. Comparison of CO_2/N_2 selectivities simulated using the methodologies including Baker's minimization and CBMC for minimization of IL molecules.

Figure 5.2 shows that selectivities are slightly overestimated when CBMC method is used as a minimization method compared with Baker's method. Nevertheless, comparison of CO_2/N_2 selectivities for two minimization methods presents a good agreement between two. Predicted CO_2/N_2 selectivities of 9 IL/CuBTC composites from the Baker's minimization method were between 14.7-22.2 whereas for the method that include CBMC method these selectivities were between 17.7-26.4. Overall, Figures 5.1 and 5.2 suggest that both methods can be used to simulate the CO_2/N_2 adsorption and separation performance of IL/MOF composites with similar accuracy. We choose to continue this work using Baker's minimization method because it is a faster method than the CBMC and we already validated its accuracy by comparing the results with experimental data as discussed in Chapter 4.

5.2. Validation of Accuracy of Molecular Simulation Method

As explained Chapter 4, validating the results of molecular simulations using experimental data is important to test their accuracy. There was only one IL/MOF composite investigated in literature from our list of 1108 [BMIM][BF_4]/MOF composites which is CuBTC. Sezginel et al.[42] investigated 5 wt.% loaded [BMIM][BF_4]/CuBTC for CO_2/N_2 separation. The IL-loading of this material was comparable with 1 IL molecule per unit cell loading which corresponds to 2.28 wt.%. Another [BMIM][BF_4]/MOF composite investigated in the literature was [BMIM][BF_4]/ZIF-8 composite[36] which had experimental loading of 4 wt.%. ZIF-8 was not included our initial 1108 MOF list because of it has a PLD lower than 6 Å, but we included ZIF-8 in our list to use it in this section. We incorporated 1 molecule of [BMIM][BF_4] per unit cell of ZIF-8 (CSD refcode: FAWCEN01) and calculated its ideal CO_2/N_2 selectivity, and CO_2 working capacity using single-component GCMC simulations at an adsorption (desorption) pressure of 1 (0.1) bar and 25 °C. Simulated IL-loading was calculated as 7.83 wt.%. Simulations and experiments including [BMIM][BF_4]/ZIF-8 composite were also comparable. We added [BMIM][BF_4]/UiO-66 composite to this list by preparing and measuring its CO_2 and N_2 uptakes at 0.1 and 1 bar pressures at 25 °C. Consequently, UiO-66 (CSD refcode: RUBTAK) was added to the simulation list and simulated at the conditions described above. It should be noted that this composite has not been reported in literature before. Before focusing on validation of the molecular simulations, we would like to discuss the characterization of [BMIM][BF_4]/UiO-66 composite.

5.2.1 Characterization and CO_2 Adsorption and Separation Performance of [BMIM][BF_4]/UiO-66 Composite

In this section, characterization and gas uptake measurements of pristine UiO-66 and [BMIM][BF_4]/UiO-66 composite is discussed. Composite material is prepared with

IL-loading of 3.34 wt.% and both materials are characterized in detail by XRF, XRD, SEM, TGA, FTIR and BET surface area and pore volume analyses as explained in Chapter 3. Also, CO_2 and N_2 adsorption of both the pristine MOF and the composite were measured between 0.1-10 bar at 25 °C using HPVA-II accordingly with Chapter 3.

5.2.1.1 X-ray Fluorescence Spectroscopy

XRF spectroscopy was performed on [BMIM][BF_4]/UiO-66 composite to calculate the actual IL-loading of the composite using the parameters given in Chapter 3. XRF results showed that zirconium is present in the composite with the weight percent of 24.16% while boron has the weight percent of 0.12%. Actual IL-loading in the [BMIM][BF_4]/UiO-66 composite was calculated as 3.44 wt.% using these results which is similar to the targeted IL-loading.

5.2.1.2 BET Surface Area and Pore Volume Analysis

BET surface area and pore volume analyses were performed on UiO-66 and [BMIM][BF_4]/UiO-66 using the conditions given in Chapter 3. Results show that UiO-66 have a surface area of 750.2 m^2/g while [BMIM][BF_4]/UiO-66 have a surface are of 577.7 m^2/g. Pore volume of UiO-66 also decreases from 0.319 cm^3/g to 0.205 cm^3/g upon IL-incorporation. This decrease is expected because of the space occupied by the IL molecules inside the pores of UiO-66.

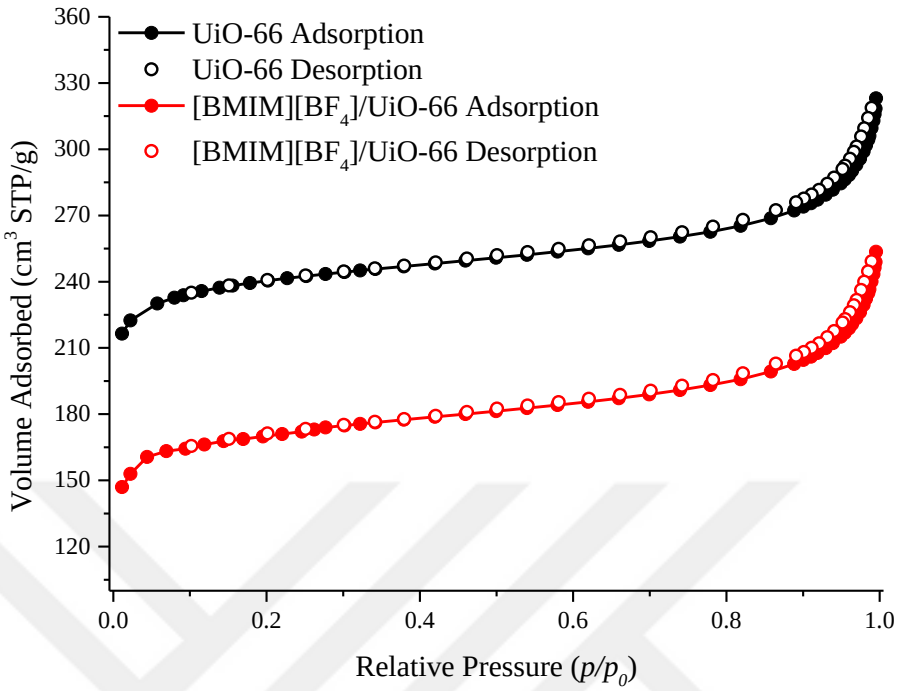

Figure 5.3. N_2 adsorption isotherms of UiO-66 and [BMIM][BF_4]/UiO-66 at -196 °C.

5.2.1.3 X-ray Diffraction

XRD patterns of UiO-66 and [BMIM][BF_4]/UiO-66 were obtained using the parameters mentioned in Chapter 3. Figure 5.4 shows the XRD patterns of the pristine UiO-66 and [BMIM][BF_4]/UiO-66 composite for 2Theta range of 5-50°. XRD pattern of UiO-66 is consistent with the literature.[104] Also, these results show that crystal structure of UiO-66 was preserved upon IL-incorporation. It should be noted that changes in the intensity of the peaks may occur due to the alterations in the electronic structure of the UiO-66 upon IL-incorporation.

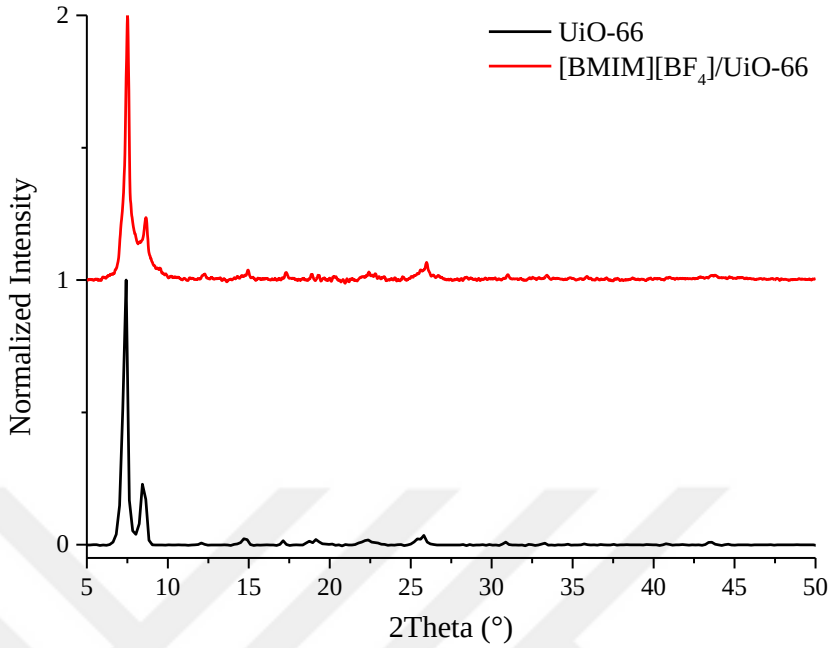

Figure 5.4. XRD patterns of UiO-66 and [BMIM][BF_4]/UiO-66 composite.

5.2.1.4 Scanning Electron Microscopy

SEM micrographs of UiO-66 and [BMIM][BF_4]/UiO-66 were obtained using the parameters given in Chapter 3. Figure 5.5 demonstrates the SEM micrographs of pristine MOF and the composite at different magnifications. Our results show that crystal size and geometry do not change in the composite when compared with the pristine UiO-66.

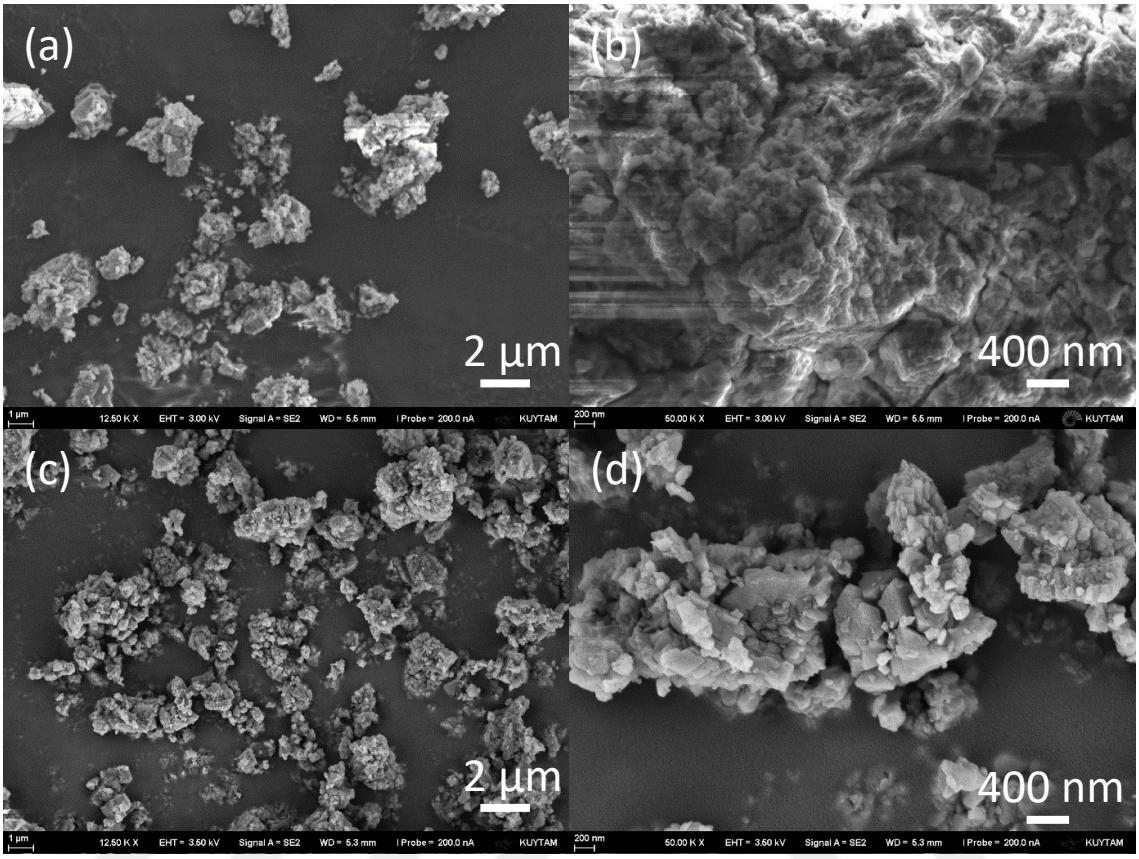

Figure 5.5. SEM micrographs of (a,b) UiO-66 and (c,d) [BMIM][BF_4]/UiO-66 at (a,c) 15k× and (b,d) 50k× magnifications.

5.2.1.5 Thermogravimetric Analysis

TGA analyses were performed to determine the thermal decomposition temperature of [BMIM][BF_4], UiO-66 and [BMIM][BF_4]/UiO-66. These analyses were using the parameters given in Chapter 3. Figure 5.6 shows thermogravimetric and derivative thermogravimetric curves of [BMIM][BF_4], UiO-66 and the composite of two materials. UiO-66 shows 7% weight loss until 100 °C while [BMIM][BF_4]/UiO-66 lose 10% of its initial weight until 100 °C. Pure [BMIM][BF_4] shows 0.4% weight loss until 100 °C. These weight losses were attributed to removal of adsorbed water from the

materials. As mentioned in Chapter 3, derivative onset temperature (T'_{onset}) was used as thermal decomposition temperature in this thesis. T'_{onset} of pristine UiO-66 was found as 448 °C which is consistent with the literature.[105] T'_{onset} of [BMIM][BF_4]/UiO-66 was found as 310 °C while [BMIM][BF_4] starts to decompose at 350 °C. This change in the T'_{onset} indicates direct interactions between [BMIM][BF_4] and UiO-66 in the composite.

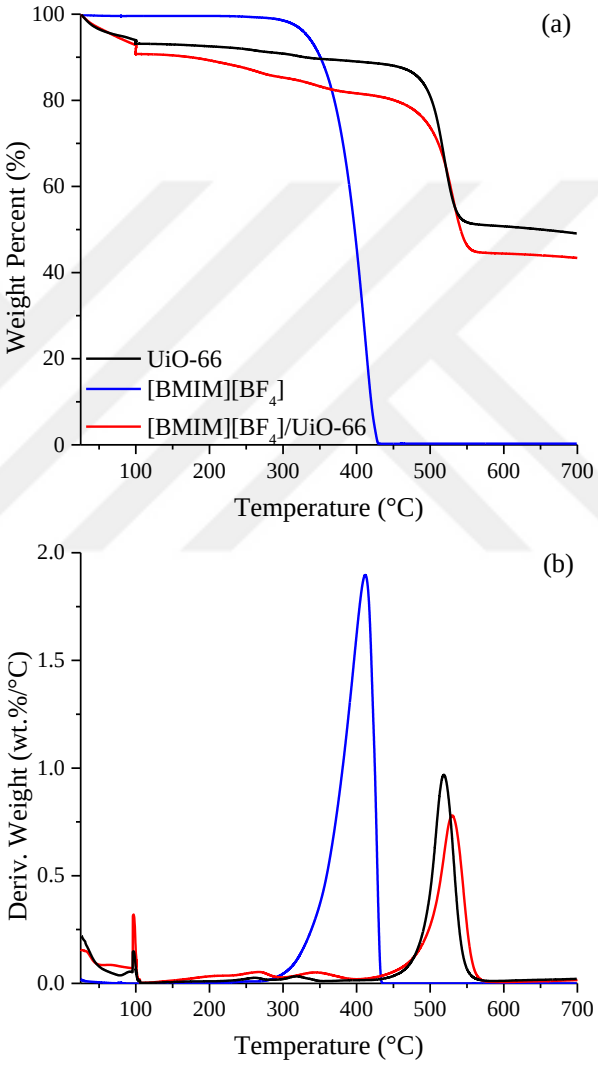

Figure 5.6. (a) Thermogravimetric and (b) derivative thermogravimetric curves of [BMIM][BF_4], UiO-66 and [BMIM][BF_4]/UiO-66.

5.2.1.6 Fourier Transform Infrared Spectroscopy

FTIR spectroscopy was performed on [BMIM][BF_4], UiO-66 and [BMIM][BF_4]/UiO-66 to confirm the interactions between [BMIM][BF_4] and UiO-66 in the composite. The analyses were performed using the parameters given in Chapter 3. FTIR spectra of [BMIM][BF_4], UiO-66 and [BMIM][BF_4]/UiO-66 are shown in Figure 5.7. Vibrational modes were assigned to the peaks in the FTIR spectrum of [BMIM][BF_4] according to the literature reports.[106,107] Symmetric (ν_s(B–F)) and asymmetric stretching mode of B–F bond (ν_{as}(B–F)) of the anion were assigned to peaks centered at 751 and 1021 cm^{-1}, respectively, in the FTIR spectrum of [BMIM][BF_4]. ν_s(B–F) and ν_{as}(B–F) shifted to 806 and 1034 cm^{-1} upon incorporation into UiO-66. ν_s(–C2H) mode exhibited blue shift from 3126 cm^{-1} to 3137 cm^{-1} while ν_s(C(4)HC(5)H) mode red shifted by 11 cm^{-1} from 3162 cm^{-1} to 3151 cm^{-1}. These shifts in the characteristic vibrational modes of [BMIM][BF_4] are because of the small changes in the structure of IL, which confirms the direct interaction between [BMIM][BF_4] and UiO-66 in the composite structure.

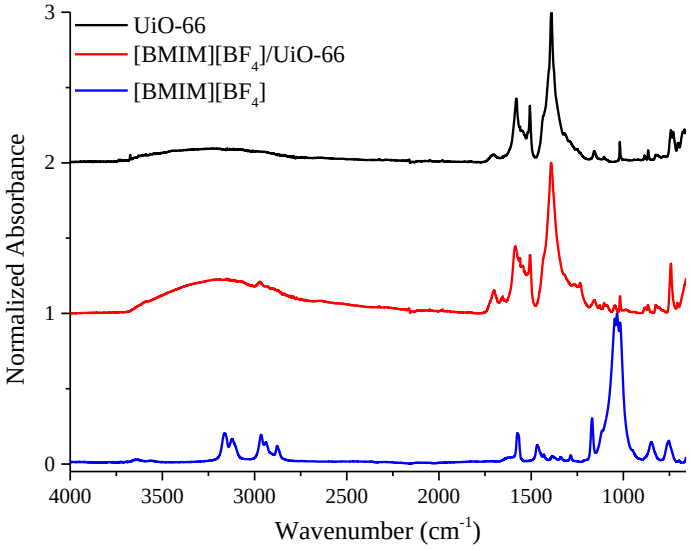

Figure 5.7. FTIR spectra of [BMIM][BF_4], UiO-66 and [BMIM][BF_4]/UiO-66.

5.2.1.7 CO_2 and N_2 Adsorption and Separation Performance of [BMIM][BF_4]/UiO-66

In this section, experimental CO_2 and N_2 adsorption and separation performance of [BMIM][BF_4]/UiO-66 and pristine UiO-66 is discussed. Adsorption measurements were conducted using the parameters given in Chapter 3. Although only 0.1 and 1 bar are needed as pressure points to compare the experimental adsorption results with that of simulations, here, we present adsorption isotherms between 0.1-10 bar. Figure 5.8 shows experimental adsorption isotherms of CO_2 and N_2 for [BMIM][BF_4]/UiO-66 and UiO-66 for the pressure range of 0.1-10 bar.

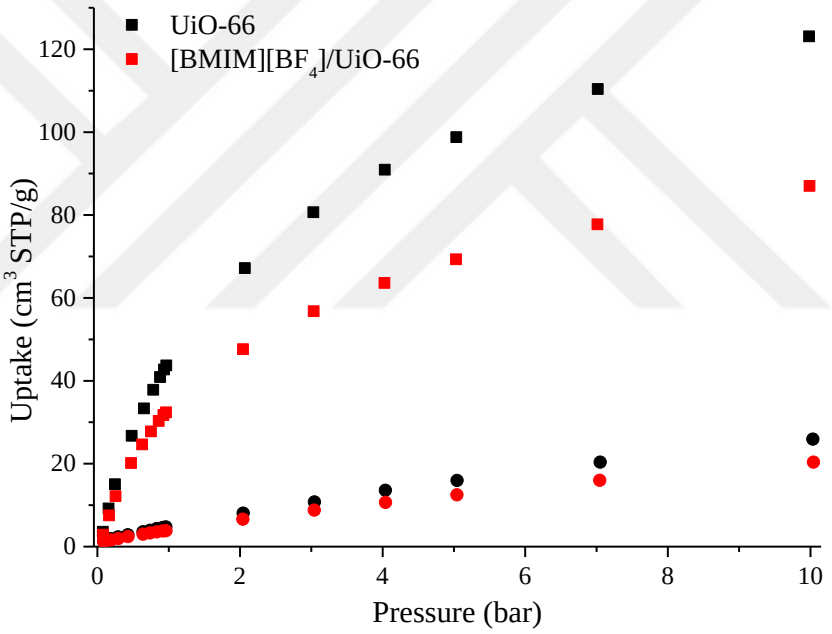

Figure 5.8. CO_2 and N_2 adsorption isotherms of [BMIM][BF_4]/UiO-66 and UiO-66 as a function of pressure. Square (round) symbols represent CO_2 (N_2) uptakes.

CO_2 uptakes of UiO-66 are between 3.6-123 cm^3 STP/g while the adsorbed amount of N_2 varies between 1.3-26 cm^3 STP/g. For [BMIM][BF_4]/UiO-66, uptake for both gases are lower than that of UiO-66 at all pressure points. They increase from 2.9 to 87 cm^3 STP/g for CO_2 and from 1.1-20.4 cm^3 STP/g for N_2 as the pressure increases.

Figure 5.9 shows ideal CO_2/N_2 selectivity of [BMIM][BF_4]/UiO-66 and UiO-66 for the pressure range of 0.1-10 bar. Parameters used to fit the dual-site Langmuir and Freundlich models are given in Appendix C. CO_2/N_2 selectivity of UiO-66 changes between 2-9.4 which is consistent with the literature.[108] CO_2/N_2 selectivities of [BMIM][BF_4]/UiO-66 are lower than that of pristine UiO-66 among the pressure range as they vary between 1.8-8.6. Although the [BMIM][BF_4]-incorporation decreases the CO_2/N_2 selectivity of UiO-66, the changes in the selectivity is lower than 10% at all pressure points. This composite has an IL-loading of 3.44 wt.%, therefore, this insignificant decrease in the CO_2/N_2 selectivity may be expected. As it will be discussed in the following section, higher IL loadings may increase the CO_2/N_2 selectivity of UiO-66. Therefore, further studies should focus on higher IL loadings than 3.44 wt.% to achieve an increase in the CO_2/N_2 selectivity of UiO-66.

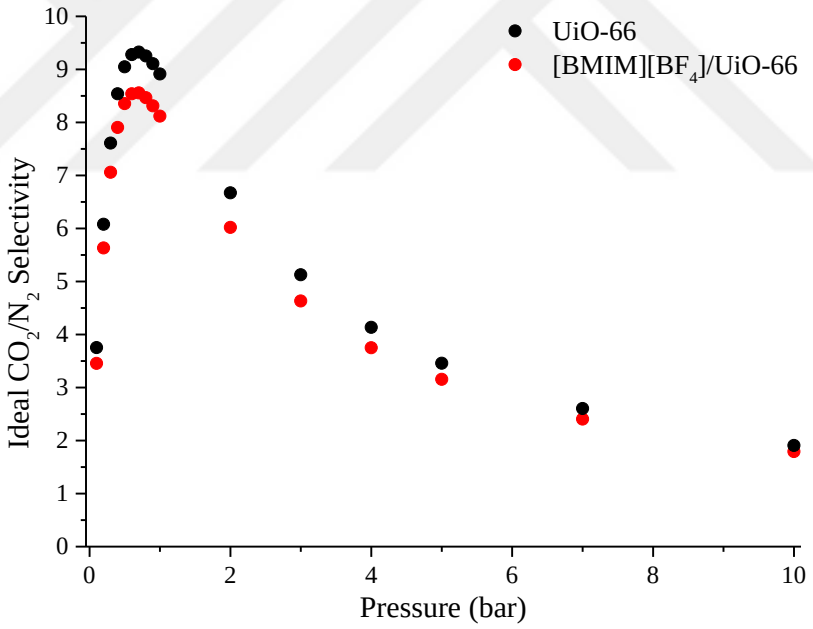

Figure 5.9. Ideal CO_2/N_2 selectivity of [BMIM][BF_4]/UiO-66 and pristine UiO-66 as a function of pressure.

5.2.2 Validation of Molecular Simulation Results

In this section, comparison of experimental and simulated ideal CO_2/N_2 selectivity and CO_2 working capacity of [BMIM][BF4]/CuBTC, [BMIM][BF4]/ZIF-8 and [BMIM][BF4]/UiO-66 composites are discussed. Figure 5.10 compares experimental and simulated ideal CO_2/N_2 selectivity and CO_2 working capacity of these composites.

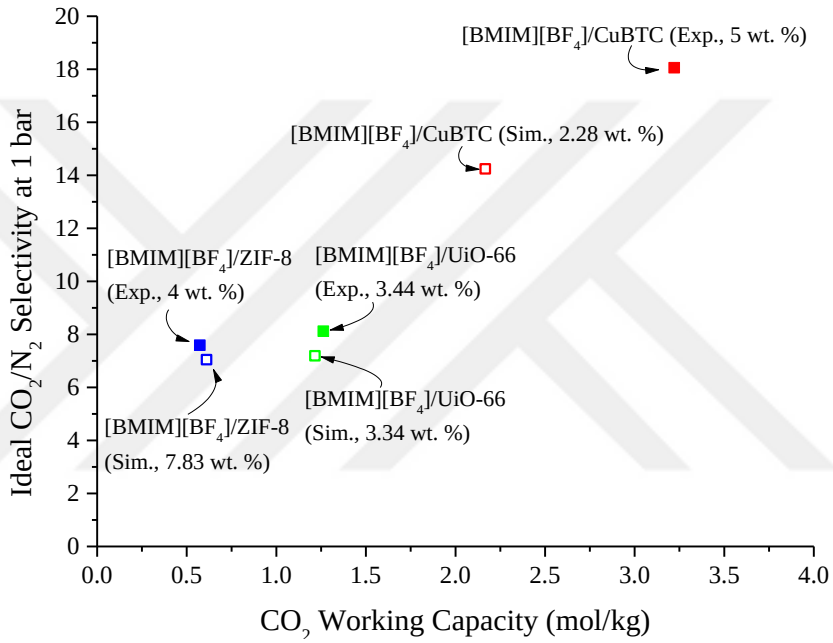

Figure 5.10. Comparison of experimental and simulated CO_2/N_2 selectivity and CO_2 working capacity of [BMIM][BF4]/CuBTC, [BMIM][BF4]/ZIF-8 and [BMIM][BF4]/UiO-66 composites.

Experimental ideal CO_2/N_2 selectivity of [BMIM][BF4]/CuBTC, [BMIM][BF4]/ZIF-8 and [BMIM][BF4]/UiO-66 composites were calculated as 18.1, 7.6 and 8.1, at 1 bar respectively. GCMC simulations predicted values of 14.3, 7.0 and 7.2, respectively, indicating that GCMC simulations were able to predict the CO_2/N_2 selectivities of these [BMIM][BF4]/MOF composites with a high accuracy. Experimental CO_2 working capacities of [BMIM][BF4]/CuBTC, [BMIM][BF4]/ZIF-8

and [BMIM][BF_4]/UiO-66 composites were measured as 3.2, 0.6 and 1.3 mol/kg, respectively, while GCMC simulations predicted them as 2.2, 0.6 and 1.2 mol/kg, respectively. Although, GCMC simulations underestimated the CO_2 working capacity of [BMIM][BF_4]/CuBTC composite, MOFs with open metal sites such as CuBTC may need some correction to their molecular simulations as discussed in Chapter 4. Overall, these results indicate that the computational methodology that we described above can be used to accurately estimate the CO_2/N_2 selectivity and CO_2 working capacity of [BMIM][BF_4]/MOF composites.

5.3. CO_2 Separation from Flue Gas Mixtures Using [BMIM][BF_4]/MOF Composites

In this section, we investigated 1108 different [BMIM][BF_4]/MOF composites to discover their potential for CO_2 separation from flue gas mixture. First, the selected MOF structures was cleaned of their excess solvent and other adsorbates that are present for some of the structures using the Python code from literature.[109] Baker's minimization was used to incorporate IL molecules into the MOFs as described in Chapter 3. IL loading was set to 1 IL molecule per unit cell in these simulations. After the incorporation, binary mixture GCMC simulations were conducted for CO_2/N_2:15/85 gas mixture at adsorption (desorption) pressure of 1 (0.1) bar at 25 °C. Figure 5.11 shows the CO_2/N_2 selectivities and CO_2 working capacities of [BMIM][BF_4]/MOF composites for CO_2/N_2 separation calculated using GCMC simulations.

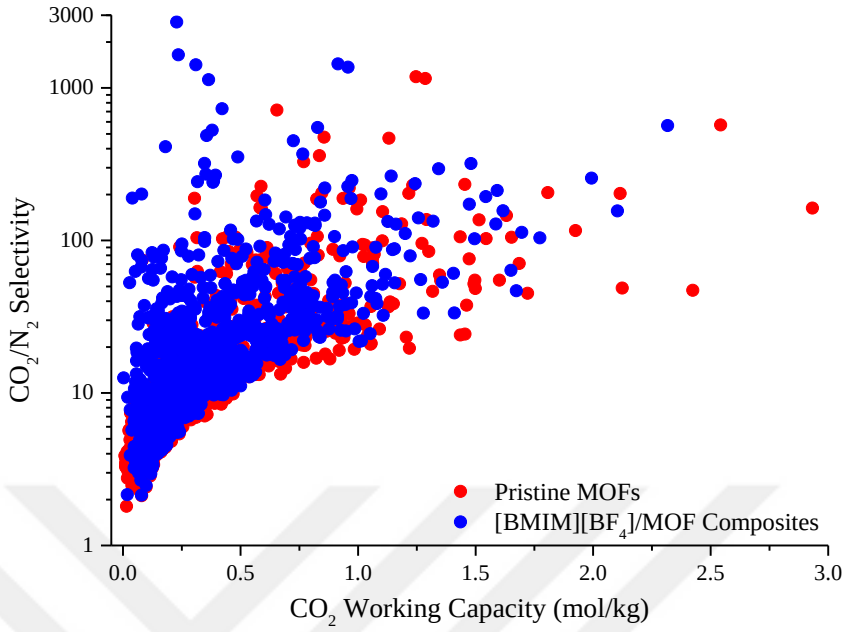

Figure 5.11. Selectivities and CO_2 working capacities of [BMIM][BF_4]/MOF composites calculated at adsorption and desorption pressures of 1 and 0.1 bar, respectively, for CO_2/N_2:15/85 mixture at 25 °C.

CO_2 selectivities of the pristine MOFs are between 1.8-1184.1 and their CO_2 working capacities are in the range of 0.01-2.93 mol/kg. Selectivities and CO_2 working capacities of [BMIM][BF_4]/MOF composites are between 2.1-2706.2 and 0.01-2.3 mol/kg, respectively. In the case of IL/MOF composites, it is important to quantify the increase in performance by comparing the performance of the composite with its corresponding pristine MOF. Although the general trend of increasing selectivity and working capacity can be seen in Figure 5.11, normalized selectivity and normalized CO_2 working capacity of [BMIM][BF_4]/MOF composites were calculated by dividing the selectivity and working capacity of the composite by the selectivity and working capacity of the corresponding pristine MOF, respectively. Figure 5.12 shows the normalized selectivity and working capacity of [BMIM][BF_4]/MOF composites.

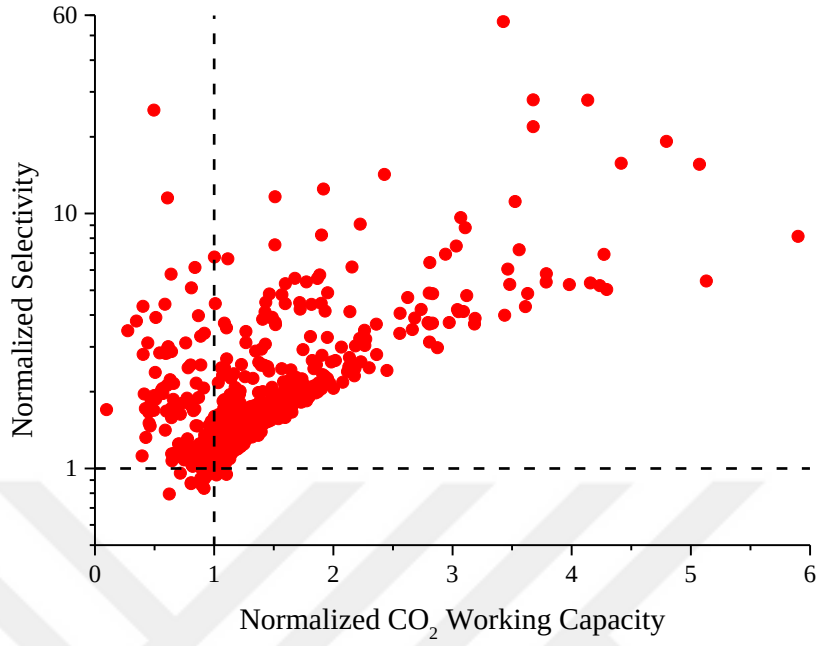

Figure 5.12. Normalized selectivity and normalized CO_2 working capacity of [BMIM][BF_4]/MOF composites for CO_2/N_2 mixture.

Normalized selectivities of composites vary between 0.8-56.6 while their normalized CO_2 working capacities are between 0.1-5.9. Although some MOFs show decreased selectivity upon incorporation of [BMIM][BF_4], 1082 of the 1108 selected MOFs show higher selectivity than their pristine MOFs. This means that 97.6% of MOFs show increased selectivity upon IL-incorporation into their pores. Similarly, CO_2 working capacities of 83.1% of MOFs (921 of 1108) have increased upon IL incorporation. 917 of the 1108 pristine MOFs (82.7%) have both increased selectivity and increased working capacity upon the incorporation of [BMIM][BF_4]. Among all, MOFs with refcodes of ALICEE and HAHPIQ demonstrated the highest increase in selectivity (56.6-times) and CO_2 working capacity (5.9-times), respectively. It is important to note that these increases in performance were achieved with only 1 IL molecule per unit cell of the MOF. Overall, Figure 5.12 demonstrates the exceptional potential of IL/MOF composites for CO_2 separation from flue gas applications.

Selectivity and working capacity are not the only factors that show the performance of an adsorbent for a separation application. Several factors such as percent regenerability (R%) and adsorption performance score (APS) are important to ascertain the potential of an adsorbent material. Therefore, R% and APS are calculated for pristine MOFs and [BMIM][BF_4]/MOF composites according to Chapter 3. Figure 5.13 shows the R% and APS of all materials investigated in this chapter.

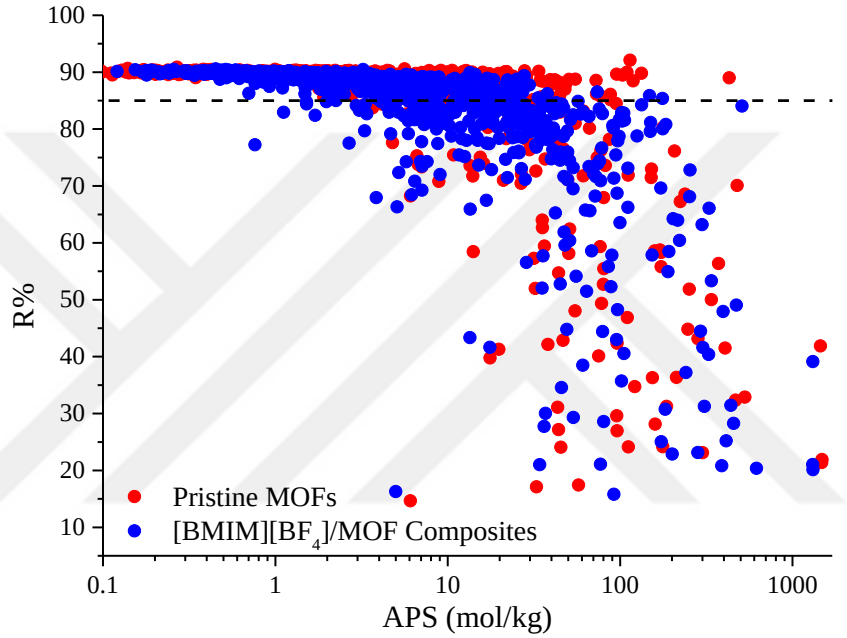

Figure 5.13 R% and APS of pristine MOFs and [BMIM][BF_4]/MOF composites computed at adsorption (desorption) pressure of 1 (0.1) bar and 25 °C for CO_2/N_2:15/85 mixture. The black dotted line shows the minimum desired R% = 85%.

87.9% of pristine MOFs have higher R% than the minimum desired value of 85% while 72.3% of [BMIM][BF_4]/MOF composites have surpassed the minimum desired value. 38 of the 1108 pristine MOFs have higher APS than 100 mol/kg. This number increases to 49 upon [BMIM][BF_4]-incorporation. Our group previously showed that most of the MOFs with APS values higher than 1000 show R% values lower than 60% for CO_2/N_2 separations.[39] Same trend can be seen in Figure 5.13 for [BMIM][BF_4]/MOF composites. Pristine MOFs with refcodes of DOMDAL, NURVAZ

and SAJFEO have APS of 1453, 1475 and 1484 mol/kg, respectively, whereas their R% are 42, 21 and 22%, respectively. It is important to note that neither APS nor R% performance factors have not changed significantly upon [BMIM][BF_4] incorporation into these three MOFs with the highest APS. Therefore, it is safe to state that IL-incorporation does not change the APS of MOFs with the highest values, but it shows its positive effect on the performance when MOFs with lower APS values were incorporated. Although, the effect on R% and APS values can be seen in Figure 5.13, normalized R% and normalized APS values were calculated for [BMIM][BF_4]/MOF composites using the definition of normalization mentioned above. Figure 5.14 demonstrates the normalized R% and normalized APS of [BMIM][BF_4]/MOF composites.

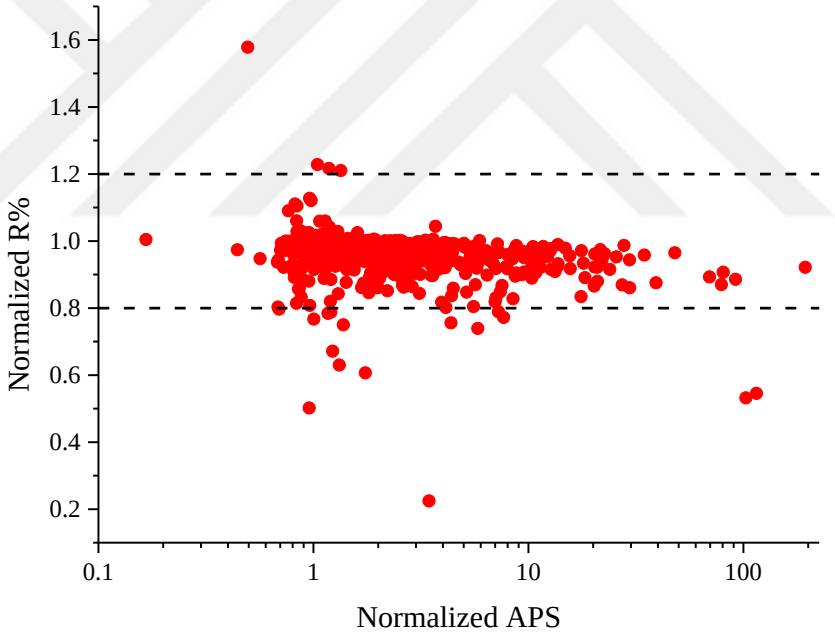

Figure 5.14. Normalized R% and normalized APS of [BMIM][BF_4]/MOF composites for CO_2/N_2 mixture. The black dotted lines show the 20% change in R%.

891 of the 1108 pristine MOFs have higher R% then their corresponding [BMIM][BF_4]/MOF composite. Although the general trend shows that R% decreases

upon IL-incorporation, the decrease is lower than 20% of the initial R% for 98.2% of the composites. Moreover, R% of 1088 pristine MOFs have shown no significant change upon IL-incorporation ($\Delta R\% < 20\%$). Figure 5.14 shows that increase in APS is more significant than the changes in R%. 92.4% of the [BMIM][BF_4] composites show higher APS than their corresponding pristine MOFs and APS values of 54 MOFs has increased more than 10-times upon IL-incorporation. Combining the data of Figures 5.13 and 5.14, we identified 25 composites that show APS increase more than 10-times and still retain the minimum desired value of R% (85%). The CSD refcodes of these pristine MOFs are listed in Table 5.1. Some structures in the CSD database show defects that should not be present in the structure that is reported in the original article such as missing hydrogen atoms. Also, solvent removal process may delete some portion of the MOF or solvent that must present in the structure in order to preserve stability. We checked the structures of MOFs that show APS increase higher than 10-times upon IL-incorporation and listed the problems we have found (Appendix C).

Table 5.1. CSD refcodes of pristine MOFs showing an APS increase of 10-times and retaining 85% R% upon [BMIM][BF_4]-incorporation.

Refcode				
BEPLUF	DETHEQ	IBIDAA	KIGCEK	SEGBOX
BEPMAM	GAVBIP	ILUCIC	LARVIL	TEJLIF
BEPMIU	HAHPIQ	ILUCOI	QOSKAY	VACFUB01
BEPNOB	HAWMAT	ILUDAV	REZXIE	XESKOX
BEPNUH	IBICED	JOYKUF	REZXIE01	XEWDUA

5.4. Structural Reasons Behind CO_2 Adsorption and Separation Performance Increase upon [BMIM][BF_4] Incorporation

In this section, structural reasons behind the increase in CO_2 adsorption and separation performance of MOFs upon IL-incorporation is discussed. Structural parameters such as PLD and porosity were calculated for both pristine MOFs and [BMIM][BF_4]/MOF composites using Zeo++ with the parameters explained in Chapter 3.

5.4.1 Effect of Weight Percent IL-loading on the CO_2/N_2 Selectivity of [BMIM][BF_4]/MOF Composites

In order to clarify the effect of weight percent IL-loading on the CO_2/N_2 selectivity of [BMIM][BF_4]/MOF composites, weight percent loadings were calculated for all composites using the equation 5.1 where $N_{[BMIM][BF_4]}$ is the number of IL molecules per unit cell (1), $w_{[BMIM][BF_4]}$ is the molar mass of [BMIM][BF_4] (226.02 g/mol), N_A is Avogadro's number (6.022×10^{23}), ρ_{MOF} is theoretical crystal density of the MOF and V_{UC} is unit cell volume of the MOF. and Figure 5.15 shows the wt.% IL-loading and normalized CO_2/N_2 selectivity for 1108 [BMIM][BF_4] composites.

$$wt.\%\, IL - loading = \frac{N_{[BMIM][BF_4]} \times \frac{w_{[BMIM][BF_4]}}{N_A}}{N_{[BMIM][BF_4]} \times \frac{w_{[BMIM][BF_4]}}{N_A} + \rho_{MOF} \times V_{UC}} \quad (5.1)$$

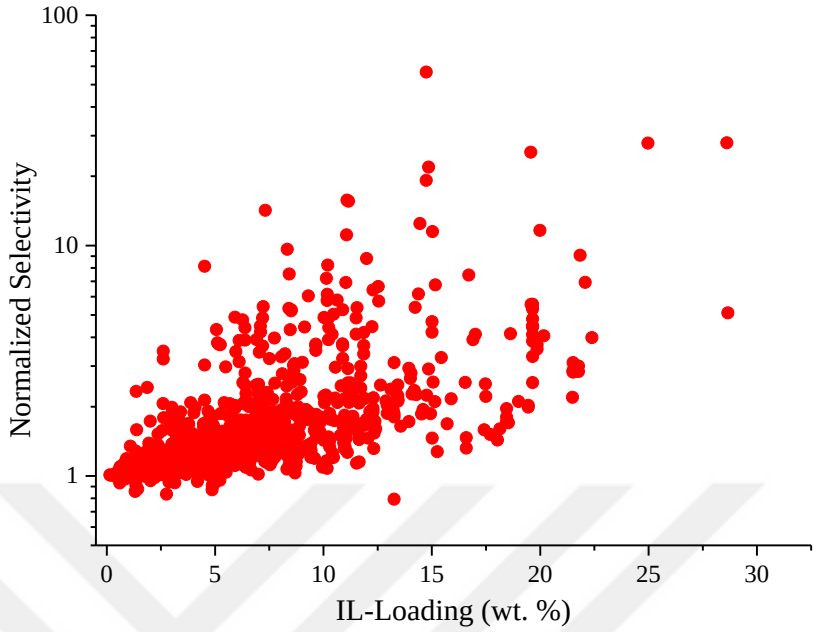

Figure 5.15. Weight percent IL loading and normalized selectivity of [BMIM][BF_4]/MOF composites.

It is important to note that weight percent IL-loading shows the ratio between weight of IL inside the MOF and the weight of MOF itself and it demonstrates how the positive effect of IL changes with the changing impact of IL in the composite structure. 54% of the [BMIM][BF_4]/MOF composites have IL-loadings between 0.15-5 wt.%. 28.1% of them have loadings in the range of 5-10 wt.%. Higher loadings are less common in our list of composites as 12.3%, 4.1% and 1.3% of [BMIM][BF_4]/MOF composites have IL loadings in between 10-15 wt.%, 15-20 wt.% and 20-30 wt.%, respectively. Figure 5.15 shows that 9 of the 14 composites that have IL loadings between 20-30 wt.% are more than 3-times selective towards CO_2 over N_2 than their corresponding pristine MOFs. 48.9% of the composites that have IL-loadings in the range of 15-20 wt.% have more than 3-times the selectivity of their corresponding MOF. The percentage of composites that are at least 3-times more CO_2 selective than their corresponding MOFs decreases as the weight percent IL loading decreases. Figure 5.16 shows the percentage of composites that are 3-times more selective than their

corresponding MOFs upon IL-incorporation for different ranges of IL-loading. Our results clearly show that increasing IL-loading increases the percentage of the composite being 3-times more selective than its corresponding MOF. This finding is consistent with the literature.[36,42] All in all, the positive effect of IL-incorporation increases with the increasing IL-loading. Further studies should include IL loadings higher than 20 wt.% to achieve promising results for CO_2 separation from CO_2/N_2 mixture.

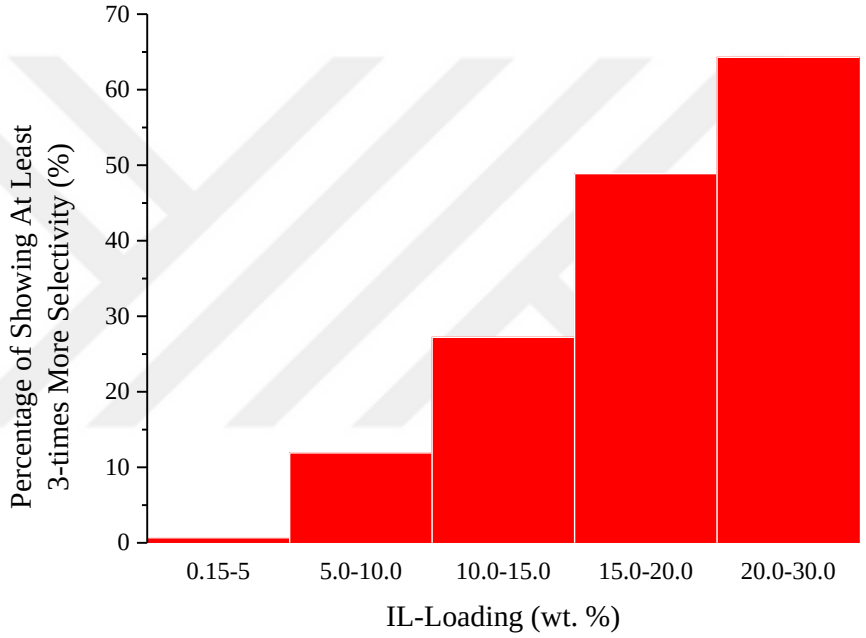

Figure 5.16. Percentage of [BMIM][BF_4]/MOF composites that are more than 3-times selective than their corresponding MOFs for different ranges of IL loading.

5.4.2 Effect of PLD on the CO_2/N_2 Selectivity of [BMIM][BF_4]/MOF Composites

Our group previously showed that MOFs with PLDs between 3.8-5 Å have the highest performance for CO_2 separation from CO_2/N_2 mixture.[39] Therefore, in this section, the effect of PLD on the CO_2 selectivity of pristine MOFs and

[BMIM][BF_4]/MOF composites is investigated. Figure 5.17 demonstrates the PLDs and CO_2/N_2 selectivities of pristine MOFs and [BMIM][BF_4]/MOF composites.

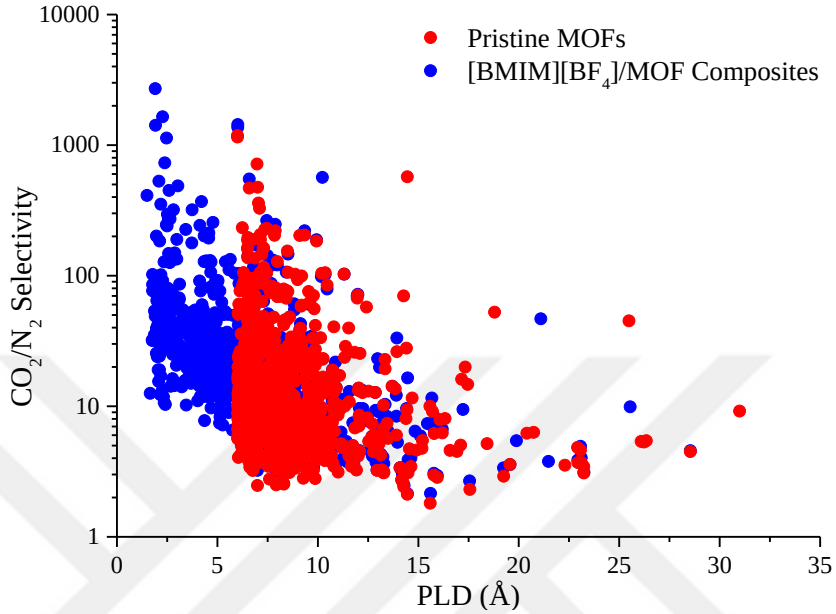

Figure 5.17. CO_2/N_2 selectivities at 1 bar and PLDs of pristine MOFs and [BMIM][BF_4]/MOF composites

36.6% of the pristine MOFs have PLDs between 6-9 Å, while PLDs of 35% of them are in the range of 9-12 Å. The number of MOFs decreases with increasing PLD. 13.2, 8.8 and 6.5% of pristine MOFs have PLDs in the ranges of 12-15, 15-18 and 18-34 Å, respectively. Percentage of materials that have PLDs in the range of 6-9 Å increases to 48.6% upon IL-incorporation. 13.2, 4.3, 1 and 1% of the composites have PLDs in the ranges of 9-12, 12-15, 15-18 and 18-32 Å. Due to the space IL molecules occupy inside the pores of MOFs, PLDs decrease upon IL-incorporation. Because of this decrease, 32% of the composites have PLDs lower than 6 Å. 56 of the 96 pristine MOFs that have higher CO_2/N_2 selectivity than 50 has the PLDs between 6-9 Å. PLDs of 30 of the MOFs that show CO_2/N_2 selectivity higher than are in the range of 9-12 Å while 6, 1 and 3 of them have the PLDs in the ranges of 12-15, 15-18 and 18-34 Å, respectively. These results show that most of the pristine MOFs with highest

selectivities have the lowest PLDs, which is consistent with the literature.[39] A total of 152 [BMIM][BF_4] composites surpass the CO_2 selectivity of 50 for CO_2/N_2 mixture. 104 of them have PLDs lower than 6 Å while 38 and 10 of them have PLDs in the ranges of 6-9 and 9-12 Å, respectively. Therefore, it can be stated that [BMIM][BF_4]/MOF composites with the lower PLDs show the highest CO_2/N_2 selectivities. For a clearer representation on the effect of PLD reduction on selectivity increase, Figure 5.18 shows the reduction of PLDs upon IL-incorporation and normalized CO_2/N_2 selectivity of composites.

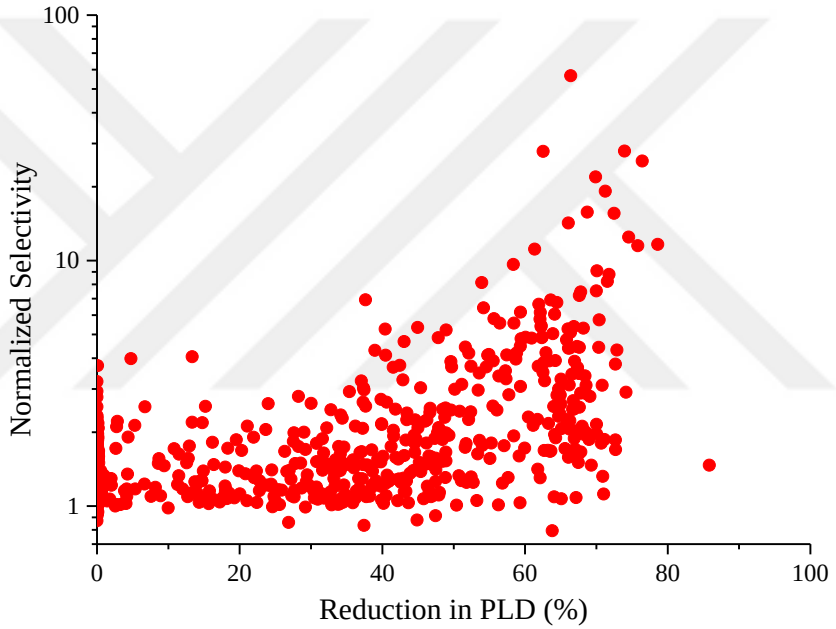

Figure 5.18. Reduction in PLD (%) upon IL-incorporation and normalized selectivity of [BMIM][BF_4]/MOF composites.

As Figure 5.18 demonstrates, 37.3% of the pristine MOFs show no change in their PLDs upon [BMIM][BF_4]-incorporation. IL-incorporation causes 0-30% decrease in the PLDs of 24.3% of the pristine MOFs while 15.3% of the MOFs experience 30-50% decrease in their PLDs. PLDs of 14 and 2.3% of the pristine MOFs decrease between 50-70 and 70-90%, respectively. There are 16 [BMIM][BF_4]/MOF composites that show normalized selectivity higher than 10. 10 of them show decrease in their PLDs in

the range of 70-90% while PLDs of 6 of them decreased by 50-70%. Also, composites that have 70-90% lower PLDs than their pristine MOFs are at least 3-times more selective than their corresponding pristine MOFs. Moreover, 74 of 155 composites that have 50-70% lower PLDs than their pristine MOFs show 3-10-times higher CO_2/N_2 selectivity than their corresponding MOFs while 6 of them are at least 10-times more selective than their pristine MOFs. All these results suggest that reduction in the PLD upon IL-incorporation is one of the reasons behind the increased CO_2 separation performance of [BMIM][BF_4]/MOF composites for CO_2/N_2 mixture.

5.4.3 Effect of Porosity on the CO_2/N_2 Selectivity of [BMIM][BF_4]/MOF Composites

Porosity is also an important factor determining the CO_2 separation performance of MOFs.[39] In this section, correlation between porosity of MOFs and [BMIM][BF_4]/MOF composites and their CO_2/N_2 selectivities is investigated. Figure 5.19 show porosities and CO_2/N_2 selectivities of pristine MOFs and [BMIM][BF_4]/MOF composites.

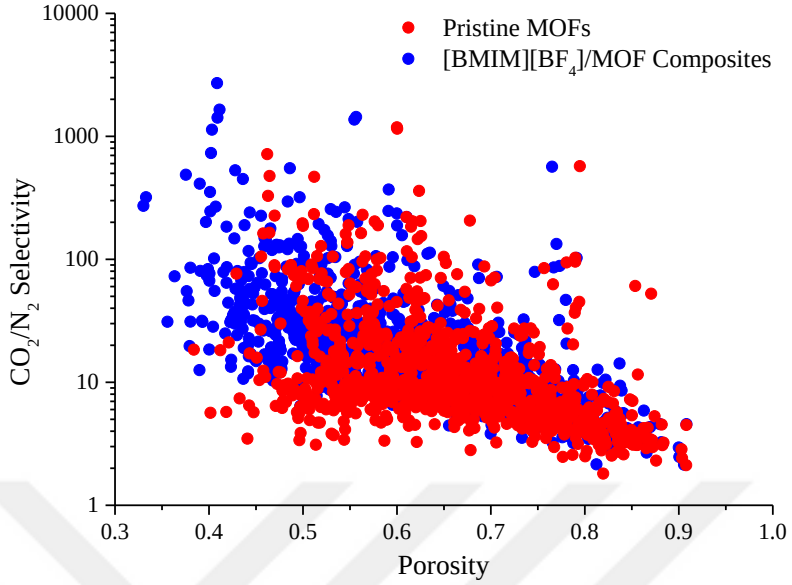

Figure 5.19. Porosities and CO_2/N_2 selectivities of pristine MOFs and [BMIM][BF_4]/MOF composites.

70 of the 1108 pristine MOFs have porosities between 0.3-0.5 while 630 and 408 of them have porosities in the ranges of 0.5-0.7 and 0.7-1, respectively. Similar to the effect of IL-incorporation on PLDs, porosity of MOFs decreases upon IL-incorporation due to the space IL-molecules occupy. 207 of the 1108 composites we investigated have porosities in the range of 0.3-0.5 while porosities of 564 and 337 of them are in the range of 0.5-0.7 and 0.7-1, respectively. 31.4% of the MOFs with porosities in the range of 0.3-0.5 have CO_2/N_2 selectivity higher than 50 while 10.2% of the MOFs with porosities in the range of 0.5-0.7 show CO_2/N_2 selectivity higher than 50. Percentage of MOFs with porosities between 0.7-1 that show CO_2/N_2 selectivity higher than 50 is the lowest with 2.5%. These results indicate that it is more likely for a MOF to have high selectivity if that MOF have low porosity. Therefore, the decreased porosity upon IL-incorporation is one of the causes of the increasing CO_2/N_2 selectivity. Figure 5.20 shows reduction of porosity upon IL-incorporation and normalized selectivities of [BMIM][BF_4]/MOF composites.

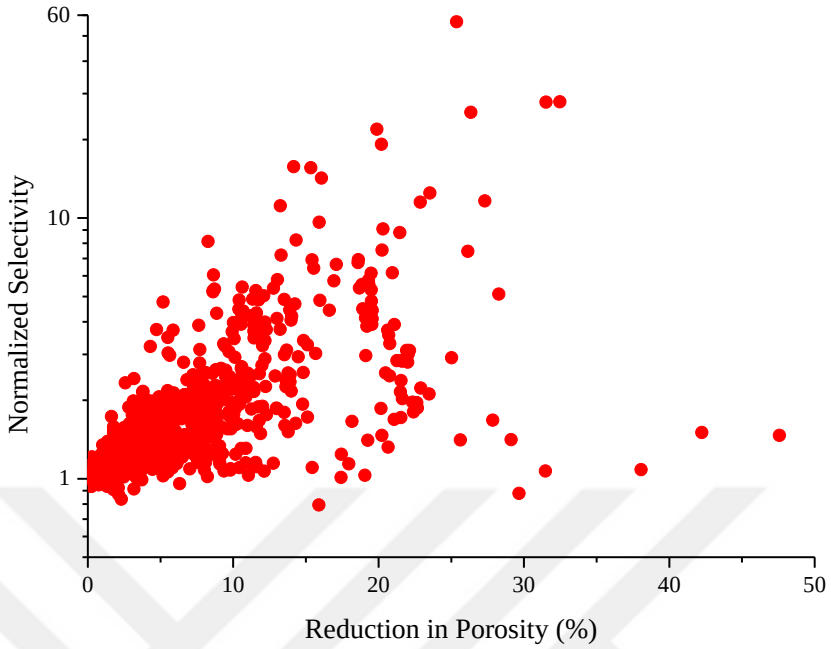

Figure 5.20. Reduction in porosity upon [BMIM][BF_4]-incorporation to MOFs and normalized selectivities of [BMIM][BF_4]/MOF composites.

Porosities 886 of the pristine MOFs decreased between 0-10% upon IL-incorporation while 179 and 16 of them showed a decrease in the range of 10-25 and 25-50%, respectively. Only 2% of the MOFs that exhibited 0-10% decrease in their porosity upon IL-incorporation show more than 3-times increase in their CO_2/N_2 selectivity. 84 of the 179 MOFs that show 10-25% decreased porosity upon IL-incorporation are more than 3-times more CO_2 selective than their corresponding pristine MOFs while 7 of the 16 composites have more than 3-times more selectivity than that of their pristine MOFs. None of the composites with decreased porosity between 0-10% show more than 10-times selectivity of their corresponding pristine MOF. 8 of the 179 composites with decreased porosities in the range of 10-25% are at least 10-times more selective than their pristine MOFs while 5 of the 16 composites with decreased porosities between 25-50% have more than 10-times selectivity when compared to their corresponding pristine MOFs. These results indicate that the more the decrease in the porosity of a MOF upon IL-incorporation the more its CO_2/N_2

selectivity is likely to be increase. This result is consistent with the findings of the section 5.4.1 where normalized selectivity of the composites increased with the weight percent IL-loading. To make it clear, our results show that selectivity increase upon IL-incorporation increases with the increasing influence of IL in the composite structure.

Chapter 6: Conclusions and Outlook

In this thesis, a computational methodology for molecular simulations of IL/MOF composites is proposed, validated using experimental results and used in high-throughput screening of numerous IL/MOF composites for CO_2 separation from CO_2/N_2 mixture. In the first part, we proposed a computational methodology to predict CO_2, CH_4, and N_2 uptakes and CO_2/CH_4, CO_2/N_2, and CH_4/N_2 selectivities of IL/CuBTC composites, in which ILs are composed of $[BMIM]^+$ cation with different type of anions. We performed GCMC simulations for seven different IL/CuBTC composites, which were previously synthesized, and compared their simulated gas uptakes with the experimentally measured data. Two different generic force fields, UFF and Dreiding, were used to represent the IL/MOF composites and the one better representing the experimental gas uptake data (Dreiding) was chosen. We then offered a pressure dependent scaling factor to improve the agreement between simulations and experiments for the gas uptakes of IL/MOF composites. Motivated from the good agreement between experiments and simulations, we applied the same molecular simulation method to estimate the gas adsorption and separation performances of two new IL/CuBTC composites, which have not been synthesized before. These composites were synthesized, characterized, and their CO_2, CH_4, and N_2 uptakes were measured and compared with the predictions of molecular simulations. Results showed that the computational method that is validated on seven different IL/CuBTC composites can be used to efficiently and accurately predict the gas uptakes and selectivities of new IL/CuBTC composites, indicating transferability of the computational approach to different types of IL-incorporated CuBTC samples. We also performed GCMC simulations to provide a more realistic performance of nine different IL/CuBTC

composites for separation of gas mixtures. Results showed that CO_2/CH_4:50/50, CO_2/N_2:15/85, and CH_4/N_2:50/50 selectivities of all IL/CuBTC composites are higher than selectivities of pristine CuBTC from 0.1 to 7 bar. These results highlight the fact that IL-incorporated CuBTC composites have a strong potential for CO_2 separation from natural gas and flue gas mixtures.

In the second part, the computational methodology that we proposed and validated in the Chapter 4 was used to predict CO_2/N_2 mixture separation performance of 1108 [BMIM][BF_4]/MOF composites. We compared two computational methods to incorporate IL molecules into MOFs, Baker's minimization and CBMC, and showed that these two methods do not have significant difference on the predicted CO_2 adsorption and separation performance of IL/MOF composites. Then, we validated the computational methodology using three different [BMIM][BF_4]/MOF composites with comparable IL loadings. One of them, [BMIM][BF_4]/UiO-66, was synthesized and characterized for the first time in the literature. Motivated from the good agreement between experimental and simulated CO_2/N_2 adsorption and separation performance of these three [BMIM][BF_4]/MOF composites, we calculated CO_2 adsorption and separation performance of 1108 [BMIM][BF_4]/MOF composites and their pristine MOFs for CO_2/N_2:15/85 mixture. Results showed that 97.6 and 83.1% of MOFs exhibit increase in their selectivities and working capacities, respectively, upon IL incorporation. We showed that R% of MOFs does not change significantly while up to 200-times increase was observed in APS values of 92.4% of MOFs upon IL incorporation. We then investigated structural factors behind the increased CO_2 separation performance of [BMIM][BF_4]/MOF composites and showed that lower PLDs and lower porosities of composites as a result of the space occupied by IL molecules inside MOFs are the reasons. We also showed that higher IL loadings results in higher selectivity increases due to the dominant impact of IL molecules in the structure of IL/MOF composites.

To conclude, we have shown the great potential of IL/MOF composite materials for CO_2 separation applications. The computational approach that we proposed in Chapter 4 can be expanded to other families of MOFs and ILs for high-throughput screening of IL/MOF composites to identify the promising materials which might offer extraordinarily high selectivities. Water is an important component of the most gas mixtures in the industry, therefore, it would be beneficial to include it in the simulations as a ternary component to mimic the industrial conditions in future studies. DFT calculations considering the adsorbed gas molecules in IL/MOF composites can also provide useful information about the change in the electronic environment of the structure that causes the increase in selectivity. Furthermore, molecular simulations can be performed to predict separation performance of systems that include IL/MOF composites in a mixed matrix membrane.

BIBLIOGRAPHY

1. Vitillo, J. G., Smit, B., Gagliardi, L., Introduction: Carbon Capture and Separation. *Chemical Reviews* **2017**, *117* (14), 9521–9523.

2. Schoedel, A., Ji, Z., Yaghi, O. M., The Role of Metal–Organic Frameworks in a Carbon-Neutral Energy Cycle. *Nature Energy* **2016**, *1* (4), 16034.

3. Belmabkhout, Y., Guillerm, V., Eddaoudi, M., Low Concentration CO_2 Capture Using Physical Adsorbents: Are Metal–Organic Frameworks Becoming the New Benchmark Materials? *Chemical Engineering Journal* **2016**, *296*, 386–397.

4. Oschatz, M., Antonietti, M., A Search for Selectivity to Enable CO_2 Capture with Porous Adsorbents. *Energy and Environmental Science* **2018**, *11* (1), 57–70.

5. Raupach, M. R., Marland, G., Ciais, P., Le Quere, C., Canadell, J. G., Klepper, G., Field, C. B., Global and Regional Drivers of Accelerating CO_2 Emissions. *Proceedings of the National Academy of Sciences* **2007**, *104* (24), 10288–10293.

6. Cavenati, S., Grande, C. A., Rodrigues, A. E., Removal of Carbon Dioxide from Natural Gas by Vacuum Pressure Swing Adsorption. *Energy and Fuels* **2006**, *20* (6), 2648–2659.

7. Leung, D. Y. C., Caramanna, G., Maroto-Valer, M. M., An Overview of Current Status of Carbon Dioxide Capture and Storage Technologies. *Renewable and Sustainable Energy Reviews* **2014**, *39*, 426–443.

8. Park, J., Jung, M., Jang, H., Lee, K., Attia, N. F., Oh, H., A Facile Synthesis Tool of Nanoporous Carbon for Promising H_2 , CO_2 , and CH_4 Sorption Capacity and Selective Gas Separation. *Journal of Materials Chemistry A* **2018**, *6* (45), 23087–23100.

9. Jiang, Y., Ling, J., Xiao, P., He, Y., Zhao, Q., Chu, Z., Liu, Y., Li, Z., Webley, P. A., Simultaneous Biogas Purification and CO_2 capture by Vacuum Swing Adsorption Using Zeolite NaUSY. *Chemical Engineering Journal* **2018**, *334* (September 2017), 2593–2602.

10. Kosinov, N., Auffret, C., Gücüyener, C., Szyja, B. M., Gascon, J., Kapteijn, F., Hensen, E. J. M., High Flux High-Silica SSZ-13 Membrane for CO_2 separation. *Journal of Materials Chemistry A* **2014**, *2* (32), 13083–13092.

11. Jiao, Y., Zheng, Y., Smith, S. C., Du, A., Zhu, Z., Electrocatalytically Switchable CO_2 Capture: First Principle Computational Exploration of Carbon Nanotubes with Pyridinic Nitrogen. *ChemSusChem* **2014**, *7* (2), 435–441.

12. Adhikari, A. K., Lin, K. S., Improving CO_2 adsorption Capacities and CO_2/N_2 separation Efficiencies of MOF-74(Ni, Co) by Doping Palladium-Containing Activated Carbon. *Chemical Engineering Journal* **2016**, *284*, 1348–1360.

13. Keskin, S., Sholl, D. S., Selecting Metal Organic Frameworks as Enabling Materials in Mixed Matrix Membranes for High Efficiency Natural Gas Purification. *Energy Environ. Sci.* **2010**, *3* (3), 343–351.

14. Uzun, A., Keskin, S., Site Characteristics in Metal Organic Frameworks for Gas Adsorption. *Progress in Surface Science* **2014**, *89* (1), 56–79.

15. Furukawa, H., Cordova, K. E., O'Keeffe, M., Yaghi, O. M., The Chemistry and Applications of Metal-Organic Frameworks. *Science* **2013**, *341* (6149).

16. Meng, W., Zeng, Y., Liang, Z., Guo, W., Zhi, C., Wu, Y., Zhong, R., Qu, C., Zou, R., Tuning Expanded Pores in Metal–Organic Frameworks for Selective Capture and Catalytic Conversion of Carbon Dioxide. *ChemSusChem* **2018**, *11* (21), 3751–3757.

17. Sun, C. Y., Qin, C., Wang, C. G., Su, Z. M., Wang, S., Wang, X. L., Yang, G. S., Shao, K. Z., Lan, Y. Q., Wang, E. B., Chiral Nanoporous Metal-Organic Frameworks with High Porosity as Materials for Drug Delivery. *Advanced Materials* **2011**, *23* (47), 5629–5632.

18. Bureekaew, S., Horike, S., Higuchi, M., Mizuno, M., Kawamura, T., Tanaka, D., Yanai, N., Kitagawa, S., One-Dimensional Imidazole Aggregate in Aluminium Porous Coordination Polymers with High Proton Conductivity. *Nature Materials* **2009**, *8* (10), 831–836.

19. Jiang, J., Furukawa, H., Zhang, Y. B., Yaghi, O. M., High Methane Storage Working Capacity in Metal-Organic Frameworks with Acrylate Links. *Journal of the American Chemical Society* **2016**, *138* (32), 10244–10251.

20. Keskin, S., van Heest, T. M., Sholl, D. S., Can Metal-Organic Framework Materials Play a Useful Role in Large-Scale Carbon Dioxide Separations? *ChemSusChem* **2010**, *3* (8), 879–891.

21. Yazaydın, A. Ö., Snurr, R. Q., Park, T.-H., Koh, K., Liu, J., LeVan, M. D., Benin, A. I., Jakubczak, P., Lanuza, M., Galloway, D. B., Low, J. J., Willis, R. R., Screening of Metal−Organic Frameworks for Carbon Dioxide Capture from Flue Gas Using a Combined Experimental and Modeling Approach. *Journal of the American Chemical Society* **2009**, *131* (51), 18198–18199.

22. Li, J. R., Tao, Y., Yu, Q., Bu, X. H., Sakamoto, H., Kitagawa, S., Selective Gas Adsorption and Unique Structural Topology of a Highly Stable Guest-Free Zeolite-Type MOF Material with N-Rich Chiral Open Channels. *Chemistry - A European Journal* **2008**, *14* (9), 2771–2776.

23. Lei, Z., Chen, B., Koo, Y. M., Macfarlane, D. R., Introduction: Ionic Liquids. *Chemical Reviews* **2017**, *117* (10), 6633–6635.

24. Marsh, K. N., Boxall, J. A., Lichtenthaler, R., Room Temperature Ionic Liquids and Their Mixtures - A Review. *Fluid Phase Equilibria* **2004**, *219* (1), 93–98.

25. Noda, A., Hayamizu, K., Watanabe, M., Pulsed-Gradient Spin-Echo 1H and 19F NMR Ionic Diffusion Coefficient, Viscosity, and Ionic Conductivity of Non-Chloroaluminate Room-Temperature Ionic Liquids. *Journal of Physical Chemistry B* **2001**, *105* (20), 4603–4610.

26. Liao, J. H., Wu, P. C., Huang, W. C., Ionic Liquid as Solvent for the Synthesis and Crystallization of a Coordination Polymer: (EMI)[Cd(BTC)] (EMI = 1-Ethyl-3-Methylimidazolium, BTC = 1,3,5-Benzenetricarboxylate). *Crystal Growth and Design* **2006**, *6* (5), 1062–1063.

27. Dybtsev, D. N., Chun, H., Kim, K., Three-Dimensional Metal–Organic Framework with (3,4)-Connected Net, Synthesized from an Ionic Liquid Medium. *Chem. Commun.* **2004**, No. 14, 1594–1595.

28. Sang, X., Zhang, J., Xiang, J., Cui, J., Zheng, L., Zhang, J., Wu, Z., Li, Z., Mo, G., Xu, Y., Song, J., Liu, C., Tan, X., Luo, T., Zhang, B., Han, B., Ionic Liquid Accelerates the Crystallization of Zr-Based Metal-Organic Frameworks. *Nature Communications* **2017**, *8* (1), 1–7.

29. Jalal, A., Uzun, A., An Ordinary Nickel Catalyst Becomes Completely Selective for Partial Hydrogenation of 1,3-Butadiene When Coated with Tributyl(Methyl)Phosphonium Methyl Sulfate. *Applied Catalysis A: General* **2018**, *562*, 321–326.

30. Sharma, P., Park, S. Do, Park, K. T., Nam, S. C., Jeong, S. K., Yoon, Y. Il, Baek, I. H., Solubility of Carbon Dioxide in Amine-Functionalized Ionic Liquids: Role of the Anions. *Chemical Engineering Journal* **2012**, *193–194*, 267–275.

31. Cui, G., Zheng, J., Luo, X., Lin, W., Ding, F., Li, H., Wang, C., Tuning Anion-Functionalized Ionic Liquids for Improved SO_2 Capture. *Angewandte Chemie - International Edition* **2013**, *52* (40), 10620–10624.

32. Kinik, F. P., Altintas, C., Balci, V., Koyuturk, B., Uzun, A., Keskin, S., [BMIM][PF_6] Incorporation Doubles CO_2 Selectivity of ZIF-8: Elucidation of Interactions and Their Consequences on Performance. *ACS Applied Materials and Interfaces* **2016**, *8* (45), 30992–31005.

33. Zeeshan, M., Nozari, V., Yagci, M. B., Islk, T., Unal, U., Ortalan, V., Keskin, S., Uzun, A., Core-Shell Type Ionic Liquid/Metal Organic Framework Composite: An Exceptionally High CO_2/CH_4 Selectivity. *Journal of the American Chemical Society* **2018**, *140* (32), 10113–10116.

34. Ban, Y., Li, Z., Li, Y., Peng, Y., Jin, H., Jiao, W., Guo, A., Wang, P., Yang, Q., Zhong, C., Yang, W., Confinement of Ionic Liquids in Nanocages: Tailoring the Molecular Sieving Properties of ZIF-8 for Membrane-Based CO_2 Capture. *Angewandte Chemie - International Edition* **2015**, *54* (51), 15483–15487.

35. Hassan, H. M. A., Betiha, M. A., Mohamed, S. K., El-Sharkawy, E. A., Ahmed, E. A., Stable and Recyclable MIL-101(Cr)–Ionic Liquid Based Hybrid Nanomaterials as Heterogeneous Catalyst. *Journal of Molecular Liquids* **2017**, *236*, 385–394.

36. Koyuturk, B., Altintas, C., Kinik, F. P., Keskin, S., Uzun, A., Improving Gas Separation Performance of ZIF-8 by [BMIM][BF4] Incorporation: Interactions and Their Consequences on Performance. *Journal of Physical Chemistry C* **2017**, *121* (19), 10370–10381.

37. Mohamedali, M., Ibrahim, H., Henni, A., Incorporation of Acetate-Based Ionic Liquids into a Zeolitic Imidazolate Framework (ZIF-8) as Efficient Sorbents for Carbon Dioxide Capture. *Chemical Engineering Journal* **2018**, *334* (October 2017), 817–828.

38. Kinik, F. P., Uzun, A., Keskin, S., Ionic Liquid/Metal–Organic Framework Composites: From Synthesis to Applications. *ChemSusChem* **2017**, *10* (14), 2842–2863.

39. Altintas, C., Avci, G., Daglar, H., Nemati Vesali Azar, A., Velioglu, S., Erucar, I., Keskin, S., Database for CO_2 Separation Performances of MOFs Based on Computational Materials Screening. *ACS Applied Materials and Interfaces* **2018**, *10* (20), 17257–17268.

40. Wei, W., Zhang, K., Qiao, Z., Jiang, J., Functional UiO-66 for the Removal of Sulfur-Containing Compounds in Gas and Liquid Mixtures: A Molecular Simulation Study. *Chemical Engineering Journal* **2019**, *356* (May 2018), 737–745.

41. Xing, H., Zhao, X., Yang, Q., Su, B., Bao, Z., Yang, Y., Ren, Q., Molecular Dynamics Simulation Study on the Absorption of Ethylene and Acetylene in Ionic Liquids. *Industrial and Engineering Chemistry Research* **2013**, *52* (26), 9308–9316.

42. Sezginel, K. B., Keskin, S., Uzun, A., Tuning the Gas Separation Performance of CuBTC by Ionic Liquid Incorporation. *Langmuir* **2016**, *32* (4), 1139–1147.

43. Nozari, V., Keskin, S., Uzun, A., Toward Rational Design of Ionic Liquid/Metal-Organic Framework Composites: Effects of Interionic Interaction Energy. *ACS Omega* **2017**, *2* (10), 6613–6618.

44. Nozari, V., Zeeshan, M., Keskin, S., Uzun, A., Effect of Methylation of Ionic Liquids on the Gas Separation Performance of Ionic Liquid/Metal–Organic Framework Composites. *CrystEngComm* **2018**, 7137–7143.

45. Lei, Z., Dai, C., Song, W., Adsorptive Absorption: A Preliminary Experimental and Modeling Study on CO_2 Solubility. *Chemical Engineering Science* **2015**, *127*, 260–268.

46. Zeeshan, M., Keskin, S., Uzun, A., Enhancing CO_2/CH_4 and CO_2/N_2 Separation Performances of ZIF-8 by Post-Synthesis Modification with [BMIM][SCN]. *Polyhedron* **2018**, *155* (2018), 485–492.

47. Kulak, H., Polat, H. M., Kavak, S., Keskin, S., Uzun, A., Improving CO_2 Separation Performance of MIL-53(Al) by Incorporating 1-n-Butyl-3-Methylimidazolium Methyl Sulfate. *Energy Technology 7* (7), 1900157.

48. Kavak, S., Polat, H. M., Kulak, H., Keskin, S., Uzun, A., MIL-53(Al) as a Versatile Platform for Ionic-Liquid/MOF Composites to Enhance CO_2 Selectivity over CH_4 and N_2. *Chemistry – An Asian Journal* **2019**, *53*.

49. Chen, Y., Hu, Z., Gupta, K. M., Jiang, J., Ionic Liquid/Metal-Organic Framework Composite for CO_2 Capture: A Computational Investigation. *Journal of Physical Chemistry C* **2011**, *115* (44), 21736–21742.

50. Vicent-Luna, J. M., Gutiérrez-Sevillano, J. J., Anta, J. A., Calero, S., Effect of Room-Temperature Ionic Liquids on CO_2 Separation by a Cu-BTC Metal-Organic Framework. *Journal of Physical Chemistry C* **2013**, *117* (40), 20762–20768.

51. Li, Z., Xiao, Y., Xue, W., Yang, Q., Zhong, C., Ionic Liquid/Metal-Organic Framework Composites for H_2S Removal from Natural Gas: A Computational Exploration. *Journal of Physical Chemistry C* **2015**, *119* (7), 3674–3683.

52. Xue, W., Li, Z., Huang, H., Yang, Q., Liu, D., Xu, Q., Zhong, C., Effects of Ionic Liquid Dispersion in Metal-Organic Frameworks and Covalent Organic Frameworks on CO_2 capture: A Computational Study. *Chemical Engineering Science* **2016**, *140*, 1–9.

53. Vicent-Luna, J. M., Luna-Triguero, A., Calero, S., Storage and Separation of Carbon Dioxide and Methane in Hydrated Covalent Organic Frameworks. *Journal of Physical Chemistry C* **2016**, *120* (41), 23756–23762.

54. Vicent-Luna, J. M., Gutiérrez-Sevillano, J. J., Hamad, S., Anta, J., Calero, S., Role of Ionic Liquid $[EMIM]^+[SCN]^-$ in the Adsorption and Diffusion of Gases in Metal-Organic Frameworks. *ACS Applied Materials and Interfaces* **2018**, *10* (35), 29694–29704.

55. Gupta, K. M., Chen, Y., Hu, Z., Jiang, J., Metal-Organic Framework Supported Ionic Liquid Membranes for CO_2 capture: Anion Effects. *Physical Chemistry Chemical Physics* **2012**, *14* (16), 5785–5794.

56. Gupta, K. M., Chen, Y., Jiang, J., Ionic Liquid Membranes Supported by Hydrophobic and Hydrophilic Metal-Organic Frameworks for CO_2 Capture. *Journal of Physical Chemistry C* **2013**, *117* (11), 5792–5799.

57. Lan, Y., Yan, T., Tong, M., Zhong, C., Large-Scale Computational Assembly of Ionic Liquid/MOF Composites: Synergistic Effect in the Wire-Tube Conformation for Efficient CO_2/CH_4 Separation. *Journal of Materials Chemistry A* **2019**, *7* (20), 12556–12564.

58. Frisch, M. J., Trucks, G. W., Schlegel, H. B., Scuseria, G. E., Robb, M. A., Cheeseman, J. R., Scalmani, G., Barone, V., Mennucci, B., Petersson, G. A., et

al., Gaussian 09 Revision A.2. 2009.

59. Becke, A. D., Density-Functional Thermochemistry. III. The Role of Exact Exchange. *The Journal of Chemical Physics* **1993**, *98* (7), 5648–5652.

60. Lee, C., Yang, W., Parr, R. G., Development of the Colle-Salvetti Correlation-Energy Formula into a Functional of the Electron Density. *Phys. Rev. B* **1988**, *37* (2), 785–789.

61. Godbout, N., Salahub, D. R., Andzelm, J., Wimmer, E., Optimization of Gaussian-Type Basis Sets for Local Spin Density Functional Calculations. Part I. Boron through Neon, Optimization Technique and Validation. *Canadian Journal of Chemistry* **1992**, *70* (2), 560–571.

62. Foster, J. P., Weinhold, F., Natural Hybrid Orbitals. *Journal of the American Chemical Society* **1980**, *102* (24), 7211–7218.

63. Reed, A. E., Curtiss, L. A., Weinhold, F., Intermolecular Interactions from a Natural Bond Orbital, Donor-Acceptor Viewpoint. *Chemical Reviews* **1988**, *88* (6), 899–926.

64. Dubbeldam, D., Calero, S., Ellis, D. E., Snurr, R. Q., RASPA: Molecular Simulation Software for Adsorption and Diffusion in Flexible Nanoporous Materials. *Molecular Simulation* **2016**, *42* (2), 81–101.

65. Rappe, A. K., Casewit, C. J., Colwell, K. S., Goddard, W. A., Skiff, W. M., UFF, a Full Periodic Table Force Field for Molecular Mechanics and Molecular Dynamics Simulations. *Journal of the American Chemical Society* **1992**, *114* (25), 10024–10035.

66. Mayo, S. L., Olafson, B. D., Goddard, W. A., DREIDING: A Generic Force Field for Molecular Simulations. *Journal of Physical Chemistry* **1990**, *94* (26), 8897–8909.

67. Potoff, J. J., Siepmann, J. I., Vapor–Liquid Equilibria of Mixtures Containing Alkanes, Carbon Dioxide, and Nitrogen. *AIChE Journal* **2001**, *47* (7), 1676–1682.

68. Dubbeldam, D., Calero, S., Vlugt, T. J. H., Krishna, R., Maesen, T. L. M., Smit, B., United Atom Force Field for Alkanes in Nanoporous Materials. *Journal of Physical Chemistry B* **2004**, *108* (33), 12301–12313.

69. Makrodimitris, K., Papadopoulos, G. K., Theodorou, D. N., Prediction of Permeation Properties of CO_2 and N_2 through Silicalite via Molecular Simulations. *Journal of Physical Chemistry B* **2001**, *105* (4), 777–788.

70. Zhao, L., Yang, Q., Ma, Q., Zhong, C., Mi, J., Liu, D., A Force Field for Dynamic Cu-BTC Metal-Organic Framework. *Journal of Molecular Modeling* **2011**, *17* (2), 227–234.

71. Willems, T. F., Rycroft, C. H., Kazi, M., Meza, J. C., Haranczyk, M., Algorithms and Tools for High-Throughput Geometry-Based Analysis of Crystalline Porous Materials. *Microporous and Mesoporous Materials* **2012**, *149* (1), 134–141.

72. Dubbeldam, D., Krishna, R., Snurr, R. Q., Method for Analyzing Structural Changes of Flexible Metal-Organic Frameworks Induced by Adsorbates. *Journal of Physical Chemistry C* **2009**, *113* (44), 19317–19327.

73. Allen, F. H., The Cambridge Structural Database: A Quarter of a Million Crystal Structures and Rising. *Acta Crystallographica Section B* **2002**, *58* (3 Part 1), 380–388.

74. Wilmer, C. E., Snurr, R. Q., Towards Rapid Computational Screening of Metal-Organic Frameworks for Carbon Dioxide Capture: Calculation of Framework Charges via Charge Equilibration. *Chemical Engineering Journal* **2011**, *171* (3), 775–781.

75. Bae, Y.-S., Snurr, R. Q., Development and Evaluation of Porous Materials for Carbon Dioxide Separation and Capture. *Angewandte Chemie International Edition* **2011**, *50* (49), 11586–11596.

76. Nosé, S., A Molecular Dynamics Method for Simulations in the Canonical Ensemble. *Molecular Physics* **1984**, *52* (2), 255–268.

77. Hoover, W. G., Canonical Dynamics: Equilibrium Phase-Space Distributions. *Phys. Rev. A* **1985**, *31* (3), 1695–1697.

78. Babucci, M., Fang, C. Y., Perez-Aguilar, J. E., Hoffman, A. S., Boubnov, A., Guan, E., Bare, S. R., Gates, B. C., Uzun, A., Controlling Catalytic Activity and Selectivity for Partial Hydrogenation by Tuning the Environment around Active Sites in Iridium Complexes Bonded to Supports. *Chemical Science* **2019**, *10* (9), 2623–2632.

79. Karra, J. R., Walton, K. S., Effect of Open Metal Sites on Adsorption of Polar and Nonpolar Molecules in Metal−Organic Framework Cu-BTC. *Langmuir* **2008**, *24* (16), 8620–8626.

80. Karra, J. R., Walton, K. S., Molecular Simulations and Experimental Studies of CO_2, CO, and N_2 Adsorption in Metal-Organic Frameworks. *Journal of Physical Chemistry C* **2010**, *114* (37), 15735–15740.

81. Koh, H. S., Rana, M. K., Wong-Foy, A. G., Siegel, D. J., Predicting Methane Storage in Open-Metal-Site Metal-Organic Frameworks. *Journal of Physical Chemistry C* **2015**, *119* (24), 13451–13458.

82. Yazaydin, A.Ö., Benin, A. I., Faheem, S. a, Jakubczak, P., Low, J. J., Willis, R. R., Snurr, R. Q., Enhanced CO_2 Adsorption in Metal-Organic Frameworks via Occupation of Open-Metal Sites by Coordinated Water Molecules. *Chemistry of Materials* **2009**, *21* (13), 1425–1430.

83. Altintas, C., Erucar, I., Keskin, S., High-Throughput Computational Screening of the Metal Organic Framework Database for CH_4/H_2 Separations. *ACS Applied Materials and Interfaces* **2018**, *10* (4), 3668–3679.

84. Kaskel, S., Characterisation of Porous Solids VIII : Proceedings of the 8th International Symposium on the Characterisation of Porous Solids; 2009; p 446.

85. Campbell, C., Ferreiro-Rangel, C. A., Fischer, M., Gomes, J. R. B., Jorge, M., A Transferable Model for Adsorption in Mofs with Unsaturated Metal Sites. *Journal of Physical Chemistry C* **2017**, *121* (1), 441–458.

86. Bae, Y., Mulfort, K. L., Frost, H., Ryan, P., Punnathanam, S., Broadbelt, L. J., Hupp, J. T., Snurr, R. Q., Separation of CO_2 from CH_4 Using Mixed-Ligand Metal - Organic Frameworks. *Langmuir* **2008**, *24* (16), 8592–8598.

87. Surblé, S., Millange, F., Serre, C., Düren, T., Latroche, M., Bourrelly, S., Llewellyn, P. L., Férey, G., Synthesis of MIL-102, a Chromium Carboxylate Metal-Organic Framework, with Gas Sorption Analysis. *Journal of the American Chemical Society* **2006**, *128* (46), 14889–14896.

88. Dubbeldam, D., Frost, H., Walton, K. S., Snurr, R. Q., Molecular Simulation of Adsorption Sites of Light Gases in the Metal-Organic Framework IRMOF-1. *Fluid Phase Equilibria* **2007**, *261* (1–2), 152–161.

89. Pérez-Pellitero, J., Amrouche, H., Siperstein, F. R., Pirngruber, G., Nieto-Draghi, C., Chaplais, G., Simon-Masseron, A., Bazer-Bachi, D., Peralta, D., Bats, N., Adsorption of CO_2, CH_4, and N_2 on Zeolitic Imidazolate Frameworks: Experiments and Simulations. *Chemistry - A European Journal* **2010**, *16* (5), 1560–1571.

90. Sagara, T., Klassen, J., Ortony, J., Ganz, E., Binding Energies of Hydrogen Molecules to Isoreticular Metal-Organic Framework Materials. *Journal of Chemical Physics* **2005**, *123* (1), 1–5.

91. Tafipolsky, M., Schmid, R., Systematic First Principles Parameterization of Force Fields for Metal-Organic Frameworks Using a Genetic Algorithm Approach. *Journal of Physical Chemistry B* **2009**, *113* (5), 1341–1352.

92. Peñalber, C. Y., Grenoble, Z., Baker, G. A., Baldelli, S., Surface Characterization of Imidazolium-Based Ionic Liquids with Cyano-Functionalized Anions at the Gas-Liquid Interface Using Sum Frequency Generation Spectroscopy. *Physical Chemistry Chemical Physics* **2012**, *14* (15), 5122–5131.

93. Lee, S., Lee, J. H., Kim, J., User-Friendly Graphical User Interface Software for Ideal Adsorbed Solution Theory Calculations. *Korean Journal of Chemical Engineering* **2018**, *35* (1), 214–221.

94. Tan, K., Zuluaga, S., Gong, Q., Gao, Y., Nijem, N., Li, J., Thonhauser, T., Chabal, Y. J., Competitive Coadsorption of CO_2 with H_2O, NH_3, SO_2, NO, NO_2, N_2, O_2, and CH_4 in M-MOF-74 (M = Mg, Co, Ni): The Role of Hydrogen Bonding. *Chemistry of Materials* **2015**, *27* (6), 2203–2217.

95. Joos, L., Swisher, J. A., Smit, B., Molecular Simulation Study of the Competitive Adsorption of H_2O and CO_2 in Zeolite 13X. *Langmuir* **2013**, *29* (51), 15936–15942.

96. Liu, J., Wang, Y., Benin, A. I., Jakubczak, P., Willis, R. R., LeVan, M. D., CO_2/H_2O adsorption Equilibrium and Rates on Metal-Organic Frameworks: HKUST-1 and Ni/DOBDC. *Langmuir* **2010**, *26* (17), 14301–14307.

97. Zhang, Z., Li, Z., Li, J., Computational Study of Adsorption and Separation of CO_2, CH_4, and N_2 by an *Rht* -Type Metal–Organic Framework. *Langmuir* **2012**, *28* (33), 12122–12133.

98. Canepa, P., Nijem, N., Chabal, Y. J., Thonhauser, T., Diffusion of Small Molecules in Metal Organic Framework Materials. *Physical Review Letters*

2013, *110* (2), 1–5.

99. Hu, Y.-F., Liu, Z.-C., Xu, C.-M., Zhang, X.-M., The Molecular Characteristics Dominating the Solubility of Gases in Ionic Liquids. *Chemical Society Reviews* **2011**, *40* (7), 3802–3823.

100. Gonzalez-Miquel, M., Bedia, J., Abrusci, C., Palomar, J., Rodriguez, F., Anion Effects on Kinetics and Thermodynamics of CO_2 Absorption in Ionic Liquids. *The Journal of Physical Chemistry B* **2013**, *117* (12), 3398–3406.

101. Tovar, T. M., Zhao, J., Nunn, W. T., Barton, H. F., Peterson, G. W., Parsons, G. N., LeVan, M. D., Diffusion of CO_2 in Large Crystals of Cu-BTC MOF. *Journal of the American Chemical Society* **2016**, *138* (36), 11449–11452.

102. Schlayer, S., Pusch, A.-K., Pielenz, F., Beckert, S., Peksa, M., Horch, C., Moschkowitz, L., Einicke, W.-D., Stallmach, F., X-Nuclei NMR Self-Diffusion Studies in Mesoporous Silica Foam and Microporous MOF CuBTC. *Materials* **2012**, *5* (12), 617–633.

103. Gutiérrez-Sevillano, J. J., Caro-Pérez, A., Dubbeldam, D., Calero, S., Molecular Simulation Investigation into the Performance of Cu-BTC Metal-Organic Frameworks for Carbon Dioxide-Methane Separations. *Physical Chemistry Chemical Physics* **2011**, *13* (45), 20453–20460.

104. Cavka, J. H., Jakobsen, S., Olsbye, U., Guillou, N., Lamberti, C., Bordiga, S., Lillerud, K. P., A New Zirconium Inorganic Building Brick Forming Metal Organic Frameworks with Exceptional Stability. *Journal of the American Chemical Society* **2008**, *130* (42), 13850–13851.

105. Wang, H.-L., Yeh, H., Chen, Y.-C., Lai, Y.-C., Lin, C.-Y., Lu, K.-Y., Ho, R.-M., Li, B.-H., Lin, C.-H., Tsai, D.-H., Thermal Stability of Metal–Organic Frameworks and Encapsulation of CuO Nanocrystals for Highly Active Catalysis. *ACS Applied Materials & Interfaces* **2018**, *10* (11), 9332–9341.

106. Heimer, N. E., Sesto, R. E. Del, Meng, Z., Wilkes, J. S., Carper, W. R., Vibrational Spectra of Imidazolium Tetrafluoroborate Ionic Liquids. *Journal of Molecular Liquids* **2006**, *124* (1), 84–95.

107. Cha, S., Ao, M., Sung, W., Moon, B., Ahlström, B., Johansson, P., Ouchi, Y., Kim, D., Structures of Ionic Liquid–Water Mixtures Investigated by IR and NMR Spectroscopy. *Phys. Chem. Chem. Phys.* **2014**, *16* (20), 9591–9601.

108. Wang, B., Huang, H., Lv, X.-L., Xie, Y., Li, M., Li, J.-R., Tuning CO_2 Selective Adsorption over N2 and CH4 in UiO-67 Analogues through Ligand Functionalization. *Inorganic Chemistry* **2014**, *53* (17), 9254–9259.

109. Moghadam, P. Z., Li, A., Wiggin, S. B., Tao, A., Maloney, A. G. P., Wood, P. A., Ward, S. C., Fairen-Jimenez, D., Development of a Cambridge Structural Database Subset: A Collection of Metal–Organic Frameworks for Past, Present, and Future. *Chemistry of Materials* **2017**, *29* (7), 2618–2625.

APPENDIX A: Supplementary for Computational Details[‡]

Table A.1. Force field parameters used to represent IL/MOF composites.

	UFF		Dreiding	
	ε (K)	σ (Å)	ε (K)	σ (Å)
C	52.873	3.431	47.888	3.473
O	30.213	3.118	48.190	3.033
N	34.745	3.261	38.975	3.263
H	22.156	2.571	5.036	2.846
S	137.974	3.595	173.223	3.590
P	153.585	3.695	161.138	3.697
B	90.640	3.638	47.838	3.581
F	25.178	2.997	36.508	3.093
Sb	226.097	3.938	276.956	3.875
Cu	2.518	3.114	-	-
Na	251.778	2.801	-	-
Fe	27.6956	4.045	-	-
Zn	27.6956	4.045	-	-
Zr	34.7453	2.783	-	-

[‡] The results given in this chapter were published in Chemical Engineering Journal with following reference: Polat, H. M.; Zeeshan, M.; Uzun, A.; Keskin, S, Unlocking CO_2 separation performance of ionic liquid/CuBTC composites: Combining experiments with molecular simulations. Chemical Engineering Journal, **2019**, *373*, 1179-1189. This chapter is the reformatted version of the mentioned research paper.

Table A.2. Parameters used to represent gases in molecular simulations.

	ε (K)	σ (Å)	q (e^-)
CH_4	158.5	3.72	0.0
C_{CO_2}	27.0	2.80	0.70
O_{CO_2}	79.0	3.05	-0.35
N_{N_2}	36.4	3.32	-0.40
N_{COM}	0.0	0.0	0.8

Table A.3. The largest cavity diameters (LCDs) and pore limiting diameters (PLDs) of pristine CuBTC and IL/CuBTC composites.

	LCD (Å)	PLD (Å)
CuBTC	13.19	6.67
[BMIM][BF_4]/CuBTC	7.05	3.53
[BMIM][CF_3SO_3]/CuBTC	7.47	3.77
[BMIM][$MeSO_4$]/CuBTC	7.18	2.99
[BMIM][$MeSO_3$]/CuBTC	5.74	2.87
[BMIM][SbF_6]/CuBTC	9.29	4.72
[BMIM][PF_6]/CuBTC	7.65	3.77
[BMIM][$OcSO_4$]/CuBTC	6.83	3.11
[BMIM][DCA]/CuBTC	6.61	3.08
[BMIM][DBP]/CuBTC	5.94	3.22

Table A.4. Number of IL molecules per unit cell and calculated IL loading for IL/CuBTC composites used in molecular simulations.

Composite	Number of IL molecules/unit cell*	IL loading (wt.%)
[BMIM][BF_4]/CuBTC	18(18.35)	29.6
[BMIM][CF_3SO_3]/CuBTC	14(14.39)	29.4
[BMIM][$MeSO_4$]/CuBTC	17(16.57)	30.5
[BMIM][$MeSO_3$]/CuBTC	18(17.70)	30.4
[BMIM][SbF_6]/CuBTC	11(11.06)	29.9
[BMIM][PF_6]/CuBTC	15(14.60)	30.6
[BMIM][$OcSO_4$]/CuBTC	12(11.90)	30.2
[BMIM][DCA]/CuBTC	20(20.20)	29.8
[BMIM][DBP]/CuBTC	12(11.90)	30.2

* Numbers inside parentheses are the number of IL molecules per unit cell for exactly 30 wt.% loading.

Table A.5. ZPVE-corrected binding energies of all conformers.

IL	Binding Energy (kJ/mol)
[BMIM][BF_4]	-339.075
	-339.013
	-337.071
	-338.953
	-338.926
[BMIM][CF_3SO_3]	-330.628
	-330.539
	-297.528
	-328.190
	-328.181

[BMIM][$MeSO_4$]	-794.044
	-794.032
	-761.811
	-791.143
	-793.856
[BMIM][$MeSO_3$]	-775.614
	-771.381
	-737.618
	-742.158
	-771.609
[BMIM][SbF_6]	-381.709
	-380.600
	-377.457
	-380.710
	-376.052
[BMIM][PF_6]	-315.954
	-313.071
	-309.768
	-313.370
	-311.931
[BMIM][$OcSO_4$]	-347.611
	-346.726
	-346.894
	-312.270
	-305.303
[BMIM][DCA]	-322.604
	-295.604
	-320.195

	-283.151
	-317.758
[BMIM][DBP]	-377.182
	-376.483
	-336.627
	-330.703
	-339.109

Table A.6. Atomic positions and point charges (NBO) of [BMIM][BF_4] optimized at B3LYP/6-311+G(2d,p).

Atom	X	Y	Z	Charge (e^-)
C	-1.256759	-1.263004	0.971089	-0.162120
C	-2.179779	-0.826398	-0.164947	-0.403650
C	-3.546093	-0.381941	0.363254	-0.383310
C	-4.485704	0.067262	-0.756336	-0.567630
N	0.094182	-1.604580	0.485143	-0.357670
C	1.159321	-0.815294	0.608477	0.328510
N	2.176428	-1.354533	-0.062274	-0.357390
C	1.745166	-2.532832	-0.638888	-0.025450
C	0.440065	-2.687191	-0.298953	-0.022330
C	3.499479	-0.741004	-0.204136	-0.361220
H	-1.128295	-0.447895	1.681375	0.238790
H	-1.645639	-2.135099	1.501200	0.197990
H	-1.697344	-0.005551	-0.700214	0.246160
H	-2.308860	-1.651831	-0.874610	0.184410
H	-4.011125	-1.198956	0.927672	0.182100
H	-3.402151	0.442377	1.068618	0.203810

H	-5.448932	0.389512	-0.355350	0.201870
H	-4.057639	0.904745	-1.311720	0.205400
H	-4.675024	-0.742997	-1.466137	0.189420
H	1.173888	0.132036	1.122207	0.283490
H	2.392931	-3.148453	-1.237316	0.230030
H	-0.261915	-3.461718	-0.551149	0.231090
H	4.209487	-1.223533	0.467372	0.203030
H	3.828308	-0.855109	-1.235343	0.211260
H	3.404590	0.318517	0.025046	0.264470
F	1.989420	2.015548	0.269668	-0.587770
B	0.612690	2.198233	-0.048504	1.337230
F	0.339337	3.501875	-0.370686	-0.541750
F	0.295752	1.315632	-1.109217	-0.580410
F	-0.133862	1.776832	1.092837	-0.588340

Table A.7. Atomic positions and point charges (NBO) of [BMIM][CF_3SO_3] optimized at B3LYP/6-311+G(2d,p).

Atom	X	Y	Z	Charge (e^-)
C	-2.472633	0.478374	0.924069	-0.166410
C	-2.358545	1.547497	-0.159728	-0.393730
C	-2.541913	2.953221	0.418039	-0.385300
C	-2.421635	4.043834	-0.646727	-0.567730
N	-2.249659	-0.881067	0.392894	-0.358450
C	-1.099717	-1.548061	0.488290	0.307760
N	-1.216338	-2.698654	-0.175924	-0.357450
C	-2.485976	-2.771701	-0.714070	-0.028590
C	-3.131896	-1.630624	-0.359839	-0.022840
C	-0.141616	-3.687027	-0.309550	-0.362510

H	-1.713114	0.638634	1.687204	0.247170
H	-3.457217	0.483276	1.395951	0.199280
H	-1.370834	1.465829	-0.619566	0.226080
H	-3.103675	1.366326	-0.942933	0.186360
H	-3.519352	3.025624	0.909193	0.183740
H	-1.788251	3.116484	1.194063	0.207950
H	-2.551905	5.035408	-0.208672	0.203940
H	-1.439400	4.017728	-1.124166	0.203720
H	-3.177422	3.923270	-1.428024	0.189520
H	-0.197885	-1.201056	0.974892	0.293440
H	-2.816914	-3.615116	-1.293861	0.230990
H	-4.130289	-1.295049	-0.577482	0.231430
H	-0.389423	-4.580907	0.262151	0.205930
H	-0.020409	-3.941010	-1.361402	0.209670
H	0.775863	-3.237334	0.066005	0.265040
F	1.176699	0.120468	-1.623455	-0.381870
C	2.236228	0.553155	-0.892903	0.831540
S	1.998735	0.118478	0.914893	2.315770
O	1.866971	-1.349634	0.866265	-1.032630
O	3.176950	0.639306	1.570592	-0.942760
O	0.719898	0.778133	1.227098	-1.031130
F	3.333221	-0.020651	-1.400653	-0.353150
F	2.332091	1.876386	-1.074511	-0.354790

Table A.8. Atomic positions and point charges (NBO) of [BMIM][$MeSO_3$] optimized at B3LYP/6-311+G(2d,p).

Atom	X	Y	Z	Charge (e^-)
C	1.612091	1.139676	0.976137	-0.165050

C	2.408014	0.512099	-0.166406	-0.411090
C	3.621682	-0.260673	0.355647	-0.381590
C	4.422006	-0.915097	-0.771210	-0.568260
N	0.404625	1.836896	0.491078	-0.359850
C	-0.828741	1.339695	0.583472	0.305890
N	-1.663668	2.146072	-0.073270	-0.360530
C	-0.939478	3.197423	-0.598835	-0.026740
C	0.358175	3.001522	-0.248799	-0.027290
C	-3.095149	1.883510	-0.246586	-0.364850
H	1.260288	0.364429	1.656370	0.241480
H	2.204760	1.862719	1.541188	0.196060
H	1.746859	-0.168049	-0.710705	0.255140
H	2.737630	1.292873	-0.861756	0.182040
H	4.273533	0.408173	0.930792	0.180250
H	3.275881	-1.032869	1.049912	0.202220
H	5.275359	-1.471138	-0.376738	0.199120
H	3.797711	-1.611580	-1.335079	0.208410
H	4.807003	-0.167895	-1.471063	0.188180
H	-1.068501	0.389898	1.058880	0.293500
H	-1.400808	3.980053	-1.174545	0.227980
H	1.237506	3.580406	-0.467854	0.229510
H	-3.662151	2.347716	0.560329	0.201540
H	-3.409476	2.297432	-1.202514	0.205530
H	-3.232300	0.801807	-0.254775	0.273560
C	-1.538428	-3.632372	0.081790	-0.804250
S	-1.066483	-1.900858	-0.043315	2.357130
O	-0.692635	-1.483758	1.337009	-1.055730
O	0.063727	-1.842861	-0.981721	-1.023480

O	-2.272044	-1.180751	-0.514890	-1.053550
H	-2.370762	-3.710816	0.778288	0.217090
H	-1.830581	-3.973055	-0.909715	0.219420
H	-0.678332	-4.192875	0.442916	0.218200

Table A.9. Atomic positions and point charges (NBO) of [BMIM][$MeSO_4$] optimized at B3LYP/6-311+G(2d,p).

Atom	X	Y	Z	Charge (e^-)
C	-2.155232	0.679851	0.911966	-0.165870
C	-1.935643	1.697346	-0.205999	-0.407780
C	-1.976054	3.131768	0.327317	-0.382280
C	-1.749437	4.166271	-0.775664	-0.568790
N	-2.063099	-0.710741	0.422869	-0.359850
C	-0.992259	-1.488514	0.580787	0.310170
N	-1.183267	-2.621274	-0.096234	-0.358140
C	-2.421635	-2.568035	-0.704351	-0.026850
C	-2.971451	-1.368603	-0.382607	-0.026640
C	-0.185028	-3.687165	-0.214076	-0.361870
H	-1.381863	0.786889	1.671454	0.242910
H	-3.133428	0.796010	1.383580	0.197110
H	-0.961266	1.508936	-0.665352	0.248030
H	-2.701188	1.568267	-0.980085	0.183220
H	-2.937712	3.320610	0.819710	0.180270
H	-1.203478	3.244546	1.093958	0.204870
H	-1.767887	5.181140	-0.372629	0.200020
H	-0.780905	4.012599	-1.256247	0.210530
H	-2.522257	4.100366	-1.546950	0.187550

H	-0.096168	-1.186525	1.113896	0.293560
H	-2.797939	-3.373018	-1.310251	0.228840
H	-3.914627	-0.933287	-0.660613	0.230490
H	-0.296983	-4.161459	-1.186869	0.207280
H	0.799793	-3.226084	-0.147628	0.267440
H	-0.327785	-4.425691	0.574704	0.203260
S	1.861116	0.174995	0.117938	2.556860
O	1.161352	0.284191	1.408322	-1.027380
O	1.517753	1.210778	-0.852054	-0.997190
O	3.416468	0.437980	0.562038	-0.756220
C	4.360312	0.443663	-0.516124	-0.210500
O	1.817558	-1.192145	-0.433764	-1.040450
H	4.381615	-0.528482	-1.013430	0.176860
H	4.115022	1.226296	-1.236187	0.182740
H	5.327257	0.647156	-0.058345	0.177800

Table A.10. Atomic positions and point charges (NBO) of [BMIM][SbF_6] optimized at B3LYP/DGDZVP.

Atom	X	Y	Z	Charge (e^-)
C	-1.580213	-1.516359	0.640703	0.363490
C	-2.981985	-2.580636	-0.696363	-0.006600
C	-3.533758	-1.371943	-0.379573	-0.007760
N	-2.643951	-0.724601	0.461151	-0.383510
H	-0.703454	-1.266538	1.220153	0.259340
H	-3.348294	-3.380762	-1.322453	0.227710
H	-4.468913	-0.925317	-0.682693	0.228990
H	-1.987773	0.791295	1.715806	0.239330

C	-2.756891	0.667378	0.952607	-0.167960
C	-2.556364	1.691866	-0.170284	-0.403210
H	-3.738566	0.769287	1.425879	0.208520
C	-2.523831	3.125628	0.378634	-0.381700
H	-3.362637	1.594807	-0.909978	0.191040
H	-1.616775	1.467581	-0.683675	0.233890
C	-2.309569	4.168469	-0.725823	-0.592350
H	-1.714457	3.205630	1.114031	0.210210
H	-3.459247	3.341855	0.913296	0.188780
H	-2.285777	5.180352	-0.308281	0.209200
H	-1.360706	3.998977	-1.245339	0.211340
H	-3.113505	4.133812	-1.470648	0.192510
N	-1.760211	-2.650666	-0.047755	-0.380950
C	-0.783590	-3.744644	-0.146322	-0.363630
H	-1.146258	-4.616231	0.403691	0.211100
H	-0.643481	-3.997953	-1.198638	0.221490
H	0.165595	-3.399072	0.262390	0.254040
F	0.208908	-0.264469	-1.201549	-0.704680
F	0.375550	0.703385	1.305439	-0.713010
F	1.477916	-1.662350	0.717600	-0.711970
F	3.144919	0.500970	1.247523	-0.671240
F	1.778004	1.957873	-0.725651	-0.676840
F	2.964009	-0.531426	-1.348644	-0.673490
Sb	1.729938	0.152054	-0.023554	3.187920

Table A.11. Atomic positions and point charges (NBO) of [BMIM][PF_6] optimized at B3LYP/6-311+G(2d,p).

Atom	X	Y	Z	Charge (e^-)
C	2.354842	-0.055872	0.956055	-0.161120
C	2.453627	-1.087417	-0.166271	-0.401360
C	2.878207	-2.457976	0.367721	-0.384770
C	2.982897	-3.506686	-0.740134	-0.570000
N	1.863263	1.248320	0.470208	-0.362060
C	0.616976	1.691742	0.622020	0.328040
N	0.478705	2.831582	-0.053842	-0.360460
C	1.681543	3.128015	-0.664324	-0.024710
C	2.547198	2.134764	-0.338587	-0.021590
C	-0.772322	3.584119	-0.175469	-0.359590
H	1.646745	-0.389920	1.712239	0.235110
H	3.320519	0.117459	1.435575	0.200910
H	1.479606	-1.162813	-0.654140	0.240250
H	3.172151	-0.745085	-0.919699	0.187260
H	3.840385	-2.372495	0.886610	0.183240
H	2.148871	-2.789311	1.113191	0.205270
H	3.277592	-4.476853	-0.335013	0.203580
H	2.024215	-3.633736	-1.247748	0.208690
H	3.725085	-3.219621	-1.490296	0.189920
H	-0.168111	1.180216	1.153101	0.285040
H	1.814742	4.004799	-1.272846	0.232640
H	3.575720	1.984452	-0.614099	0.233290
H	-0.726463	4.486424	0.433859	0.206110
H	-0.923119	3.848104	-1.220558	0.214710
H	-1.588164	2.942111	0.147808	0.259110

F	-2.234039	0.782857	0.586901	-0.613570
P	-1.933055	-0.735454	-0.029249	2.603770
F	-1.551369	-2.187779	-0.614583	-0.581350
F	-0.738549	-0.890014	1.121870	-0.613750
F	-3.061577	-0.508661	-1.152441	-0.578670
F	-2.998508	-1.364201	0.995503	-0.576500
F	-0.802128	-0.041687	-1.022793	-0.607440

Table A.12. Atomic positions and point charges (NBO) of [BMIM][$OcSO_4$] optimized at B3LYP/6-311+G(2d,p).

Atom	X	Y	Z	Charge (e^-)
C	-3.473537	0.063626	-1.329352	0.299090
C	-5.564133	-0.345356	-1.937130	-0.028100
C	-5.453644	0.991420	-1.686831	-0.025840
N	-4.142990	1.226457	-1.311294	-0.372980
H	-2.425017	-0.069931	-1.034054	0.300320
H	-6.410117	-0.940503	-2.244310	0.230650
H	-6.185537	1.782692	-1.734482	0.229980
H	-2.819954	2.803163	-1.677207	0.215890
C	-3.565461	2.535649	-0.921732	-0.154680
C	-2.944440	2.532058	0.479439	-0.417220
H	-4.388447	3.253832	-0.990139	0.199540
C	-3.929694	2.221849	1.614374	-0.387180
H	-2.515105	3.533530	0.625302	0.206270
H	-2.102725	1.829404	0.502964	0.249800
C	-3.248775	2.238454	2.988964	-0.579320
H	-4.378190	1.231744	1.454458	0.195400

H	-4.756395	2.949525	1.594192	0.178620
H	-3.970902	2.023036	3.785203	0.198710
H	-2.455084	1.484676	3.038270	0.232850
H	-2.803978	3.220306	3.197796	0.187580
N	-4.320549	-0.903751	-1.705503	-0.354190
C	-3.963442	-2.325332	-1.825472	-0.368360
H	-3.177112	-2.534816	-1.094874	0.279100
H	-4.847630	-2.922537	-1.594830	0.205030
H	-3.627584	-2.537112	-2.844350	0.204090
C	1.509941	-1.983939	1.203639	-0.026440
C	2.346765	-1.224059	0.176206	-0.410760
H	1.950782	-2.965273	1.413381	0.174850
H	1.431294	-1.433295	2.147586	0.195620
C	3.784108	-0.994783	0.665001	-0.377990
H	1.863029	-0.264968	-0.042734	0.214050
H	2.356532	-1.795743	-0.762405	0.191560
H	3.763726	-0.427691	1.608008	0.189980
H	4.253279	-1.962866	0.900613	0.184630
O	-2.238737	-1.955644	0.715470	-1.016530
O	-0.834566	-0.608359	2.305762	-0.974810
O	-0.808148	-0.131479	-0.135765	-1.036010
O	0.181820	-2.294315	0.726974	-0.759860
C	4.658597	-0.247918	-0.352107	-0.372620
H	4.680153	-0.814253	-1.295741	0.186290
H	4.190879	0.719854	-0.588062	0.188520
C	6.096682	-0.012020	0.129755	-0.375480
H	6.563635	-0.980503	0.366336	0.186510
H	6.074283	0.553667	1.073803	0.187470

C	6.971515	0.735415	-0.886118	-0.376950
H	6.995151	0.170249	-1.830734	0.186020
H	6.505530	1.704355	-1.123160	0.186300
C	8.409790	0.972643	-0.405259	-0.381050
H	8.876509	0.005021	-0.169116	0.186480
H	8.387138	1.538147	0.537883	0.186700
C	9.275808	1.720010	-1.426619	-0.569540
H	10.295621	1.873154	-1.052751	0.197460
H	9.346951	1.162385	-2.369624	0.191280
H	8.853906	2.706923	-1.657393	0.191280
S	-1.008955	-1.156441	0.947355	2.527980

Table A.13. Atomic positions and point charges (NBO) of [BMIM][DCA] optimized at B3LYP/6-311+G(2d,p).

Atom	X	Y	Z	Charge (e^-)
C	1.258575	-0.708176	-0.853109	-0.186320
C	2.275490	-0.792610	0.289041	-0.385430
C	3.599466	-0.118429	-0.099762	-0.397480
C	4.629324	-0.154680	1.035107	-0.568110
N	-0.034981	-1.343336	-0.502965	-0.354750
C	-1.152847	-0.698850	-0.143969	0.305290
N	-2.102776	-1.601436	0.137727	-0.354910
C	-1.574678	-2.866084	-0.046293	-0.026730
C	-0.279607	-2.703768	-0.444818	-0.020430
C	-3.474982	-1.278547	0.562192	-0.374410
H	1.058310	0.339864	-1.095079	0.270430
H	1.621968	-1.214351	-1.753529	0.201530

H	1.855357	-0.290262	1.170180	0.208900
H	2.451546	-1.842933	0.565548	0.185550
H	4.015824	-0.616504	-0.988070	0.183610
H	3.391609	0.920136	-0.382694	0.233130
H	5.565206	0.326636	0.729359	0.205680
H	4.258462	0.376089	1.920580	0.199070
H	4.865296	-1.184713	1.334073	0.187570
H	-1.303490	0.371929	-0.081166	0.278130
H	-2.159901	-3.758298	0.115323	0.232880
H	0.479129	-3.429514	-0.693606	0.233860
H	-4.179410	-1.684429	-0.168211	0.206830
H	-3.657740	-1.722527	1.543920	0.207000
H	-3.569375	-0.189849	0.615529	0.282080
N	-1.064813	3.520542	-0.009504	-0.699470
C	-2.027112	2.672486	0.242678	0.494520
N	-2.911321	1.922547	0.473358	-0.632560
C	0.093545	3.002110	-0.353105	0.476110
N	1.145915	2.569969	-0.664319	-0.591560

Table A.14. Atomic positions and point charges (NBO) of [BMIM][DBP] optimized at B3LYP/6-311+G(2d,p).

Atom	X	Y	Z	Charge (e^-)
C	-2.571748	-1.240041	0.253250	0.297700
C	-4.291304	-2.634682	0.196530	-0.070330
C	-4.521619	-1.639251	-0.709584	-0.060480
N	-3.436139	-0.779590	-0.658776	-0.360380
H	-1.593315	-0.832912	0.511118	0.313460

H	-4.879784	-3.499188	0.463103	0.259430
H	-5.348809	-1.476731	-1.382726	0.261460
H	-2.121420	0.558325	-1.529412	0.324320
C	-3.208507	0.446277	-1.461307	-0.273260
C	-3.819797	1.702833	-0.832713	-0.482370
H	-3.625713	0.250754	-2.454882	0.239440
C	-5.350729	1.725561	-0.731401	-0.479370
H	-3.481156	2.545364	-1.451174	0.256900
H	-3.366961	1.854926	0.155634	0.255800
C	-5.884208	3.054553	-0.181871	-0.686780
H	-5.696202	0.907165	-0.084193	0.229380
H	-5.785491	1.542079	-1.726011	0.228550
H	-6.978380	3.047367	-0.114536	0.240170
H	-5.488388	3.254197	0.821640	0.237190
H	-5.593783	3.893994	-0.825748	0.235810
N	-3.067409	-2.363974	0.785119	-0.363470
C	-2.361852	-3.154071	1.802927	-0.485480
H	-2.924183	-3.131947	2.740349	0.245170
H	-2.261921	-4.184885	1.453636	0.245360
H	-1.373277	-2.706000	1.938788	0.310250
H	2.836330	4.352608	-0.584615	0.233110
C	3.514643	3.998389	0.205341	-0.474700
C	3.161339	2.548910	0.567048	-0.495520
H	3.336854	4.647606	1.075853	0.228470
C	4.966138	4.164176	-0.261600	-0.683570
C	1.714226	2.403782	1.037398	-0.110230
H	3.320112	1.898022	-0.302364	0.245420
H	3.829964	2.190908	1.362961	0.232350

H	5.190146	5.208354	-0.513083	0.233920
H	5.671297	3.849994	0.518880	0.229760
H	5.166114	3.555506	-1.152731	0.231960
H	1.538368	3.036673	1.916691	0.212320
H	1.014294	2.705916	0.249353	0.230070
O	1.410879	1.064351	1.459181	-0.870720
P	0.707387	-0.006314	0.428151	2.584350
O	-0.228253	0.705439	-0.524981	-1.193480
O	0.152337	-1.128501	1.288835	-1.192990
O	1.970741	-0.561048	-0.468663	-0.869660
C	2.957712	-1.397747	0.150989	-0.111980
C	3.891918	-1.928903	-0.930168	-0.484090
H	2.458073	-2.220227	0.678442	0.223050
H	3.518507	-0.812216	0.893708	0.209960
C	4.996494	-2.832376	-0.364986	-0.475010
H	4.340719	-1.078433	-1.462140	0.236790
H	3.296500	-2.482005	-1.669947	0.236800
H	5.580655	-2.273813	0.380951	0.232190
H	4.540014	-3.675506	0.174122	0.231010
C	5.940317	-3.372911	-1.446258	-0.683810
H	6.718868	-4.014203	-1.014898	0.234820
H	5.392304	-3.966467	-2.189504	0.229890
H	6.439922	-2.554484	-1.980481	0.231040

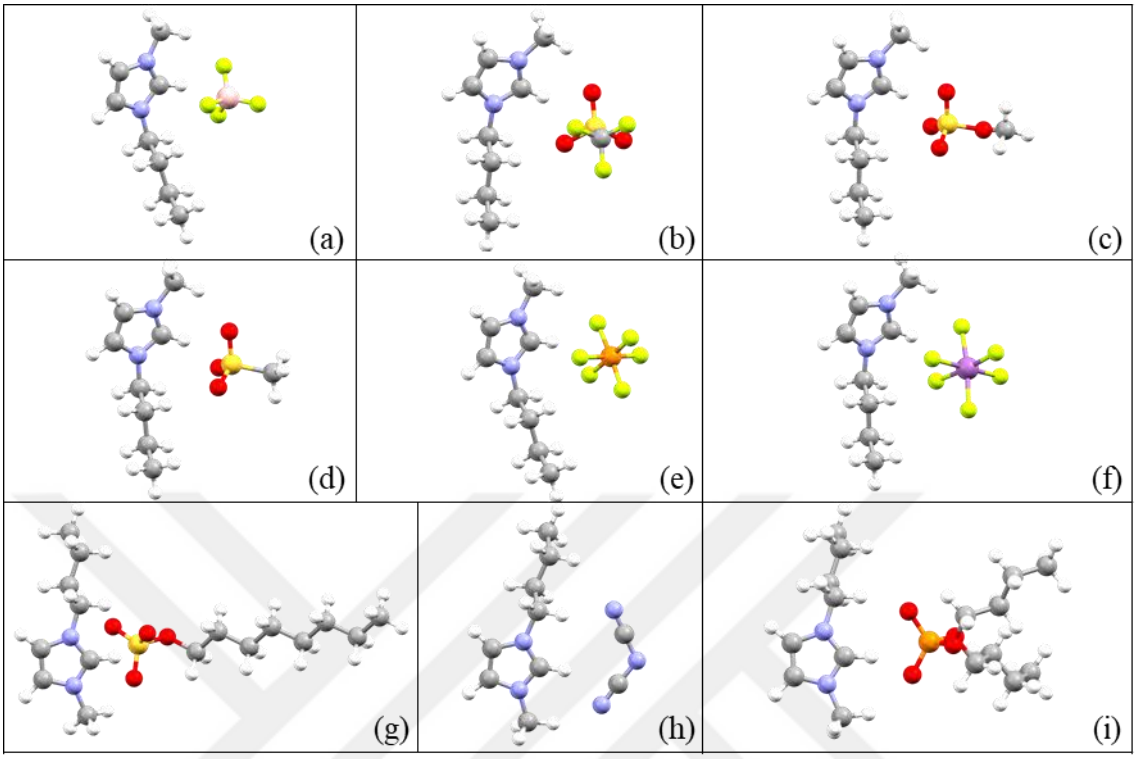

Figure A.1. Ball-and-stick molecular structures of (a) [BMIM][BF_4], (b) [BMIM][CF_3SO_3], (c) [BMIM][$MeSO_4$], (d) [BMIM][$MeSO_3$], (e) [BMIM][PF_6], (f) [BMIM][SbF_6], (g) [BMIM][$OcSO_4$], (h) [BMIM][DCA] and (i) [BMIM][DBP]

APPENDIX B: Supplementary Information for Chapter 4[§]

Table B.1. Dual-site Langmuir* fit parameters for [BMIM][DCA]/CuBTC and [BMIM][DBP]/CuBTC.

	[BMIM][DCA]/CuBTC			[BMIM][DBP]/CuBTC		
	CO_2	CH_4	N_2	CO_2	CH_4	N_2
q_1 (cm^3/g)	40.3959	14.5218	45.8415	50.4451	142.506	10.7770
k_1 (1/bar)	2.49303	1.19885	0.05632	0.07153	0.02644	0.20329
q_2 (cm^3/g)	147.202	93.6937	0.52610	64.9687	13.6346	4137.12
k_2 (1/bar)	0.03454	0.08022	2.63945	0.69015	0.65831	0.000217

*Dual-site Langmuir isotherm:

$$\mathrm{n(P)} = q_1 \times \frac{k_1 \times \mathrm{P}}{1 + k_1 \times \mathrm{P}} + q_2 \times \frac{k_2 \times \mathrm{P}}{1 + k_2 \times \mathrm{P}}$$

where P is the pressure, q_1 and q_2 is the saturation capacity of adsorption sites 1 and 2 and k_1 and k_2 are the affinity constants.

[§] The results given in this chapter were published in Chemical Engineering Journal with following reference: Polat, H. M.; Zeeshan, M.; Uzun, A.; Keskin, S, Unlocking CO_2 separation performance of ionic liquid/CuBTC composites: Combining experiments with molecular simulations. Chemical Engineering Journal, **2019**, *373*, 1179-1189. This chapter is the reformatted version of the mentioned research paper.

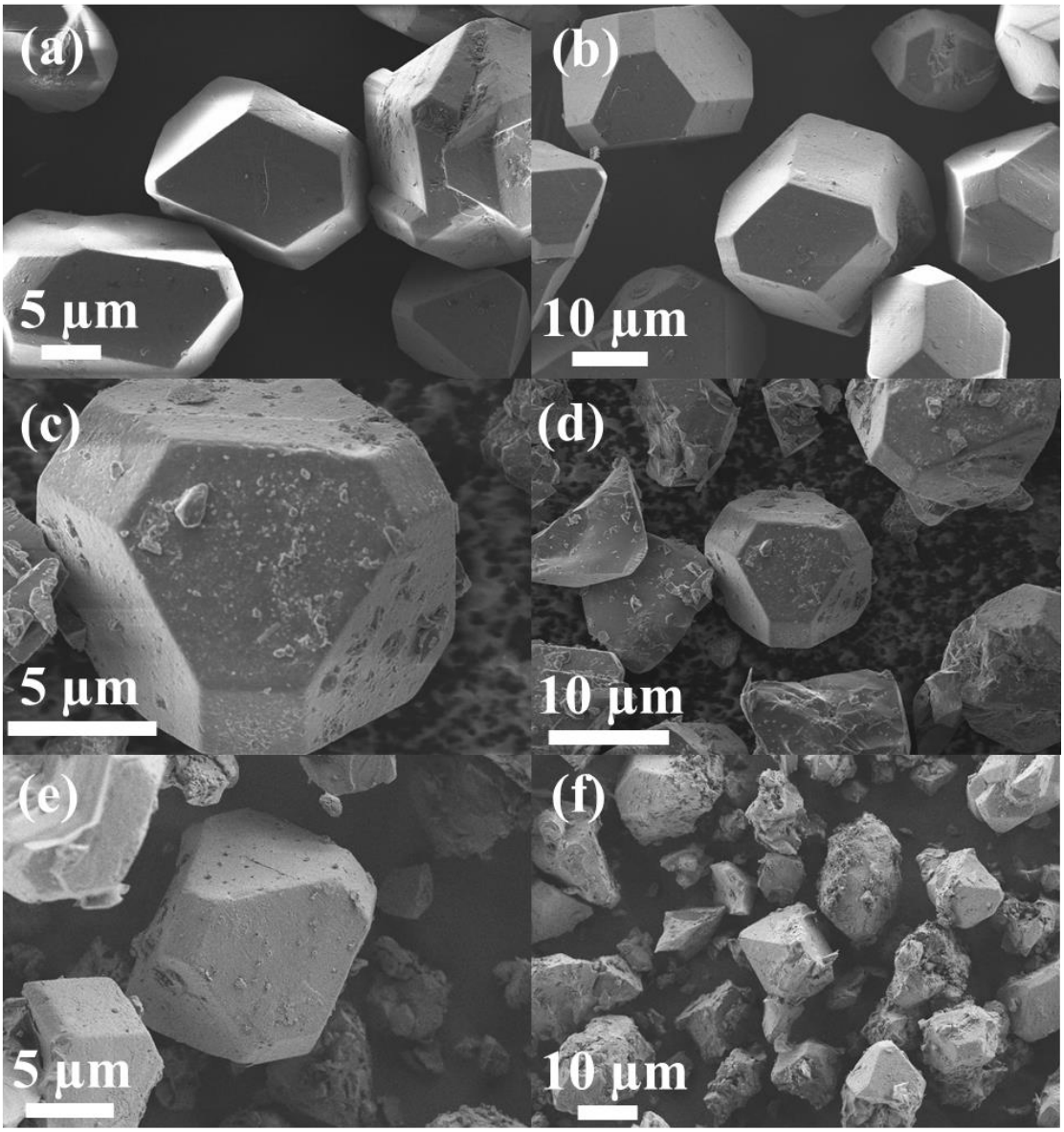

Figure B.1. SEM images of (a,b) pristine CuBTC [BMIM][DCA]/CuBTC, (c,d) [BMIM][DCA]/CuBTC and (e,f) [BMIM][DBP]/CuBTC at different magnifications.

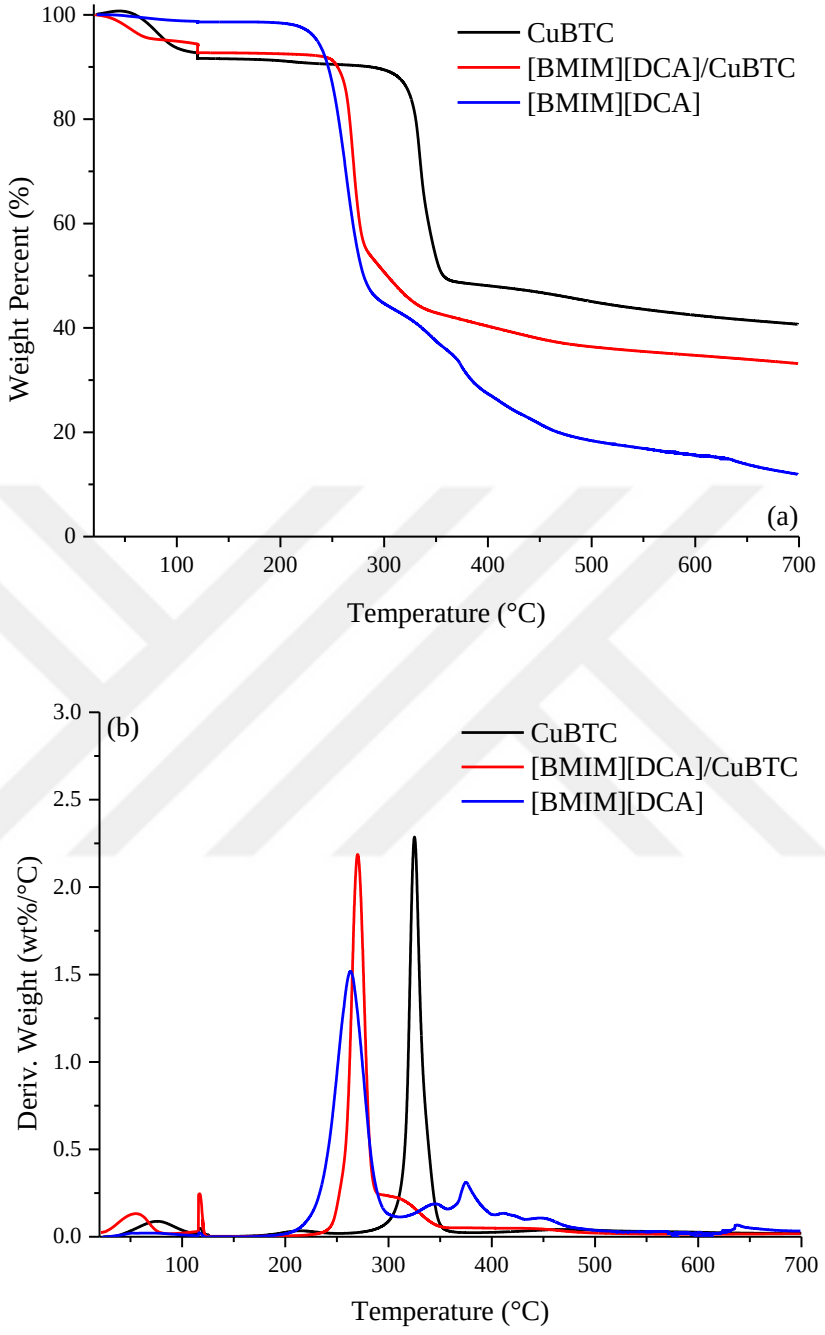

Figure B.2. (a) TGA and (b) derivative TGA curves of CuBTC, [BMIM][DCA]/CuBTC, and bulk [BMIM][DCA].

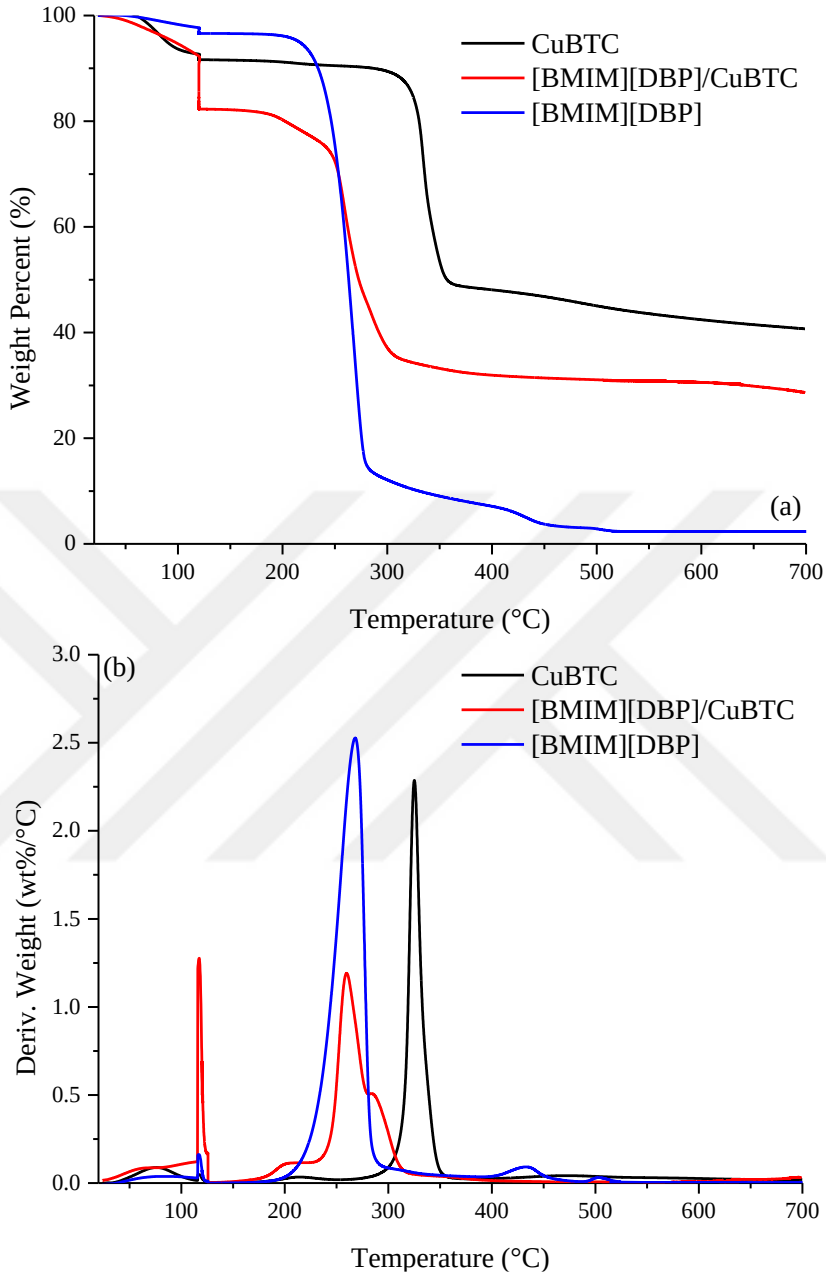

Figure B.3. (a) TGA and (b) derivative TGA curves of CuBTC, [BMIM][DBP]/CuBTC, and bulk [BMIM][DBP].

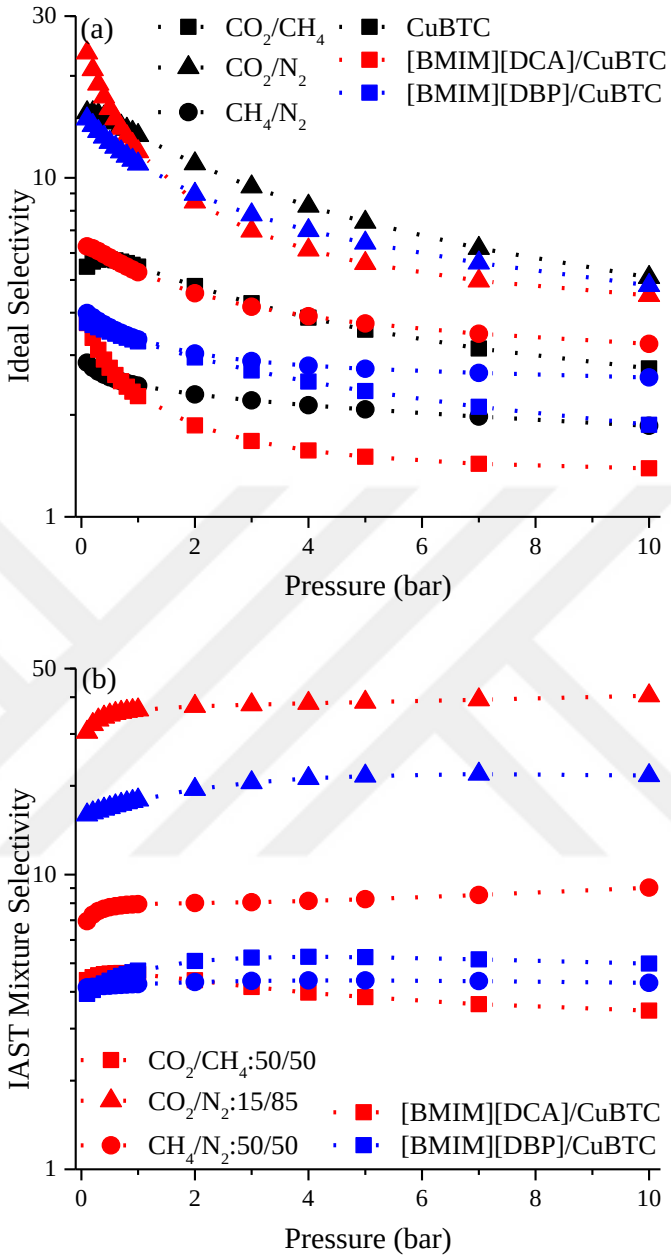

Figure B.4. (a) Experimental ideal CO_2/CH_4, CO_2/N_2, and CH_4/N_2 selectivities of CuBTC, [BMIM][DCA]/CuBTC, and [BMIM][DBP]/CuBTC as a function of pressure. (b) Mixture selectivities calculated using IAST from experimental uptakes of [BMIM][DCA]/CuBTC and [BMIM][DBP]/CuBTC as a function of pressure.

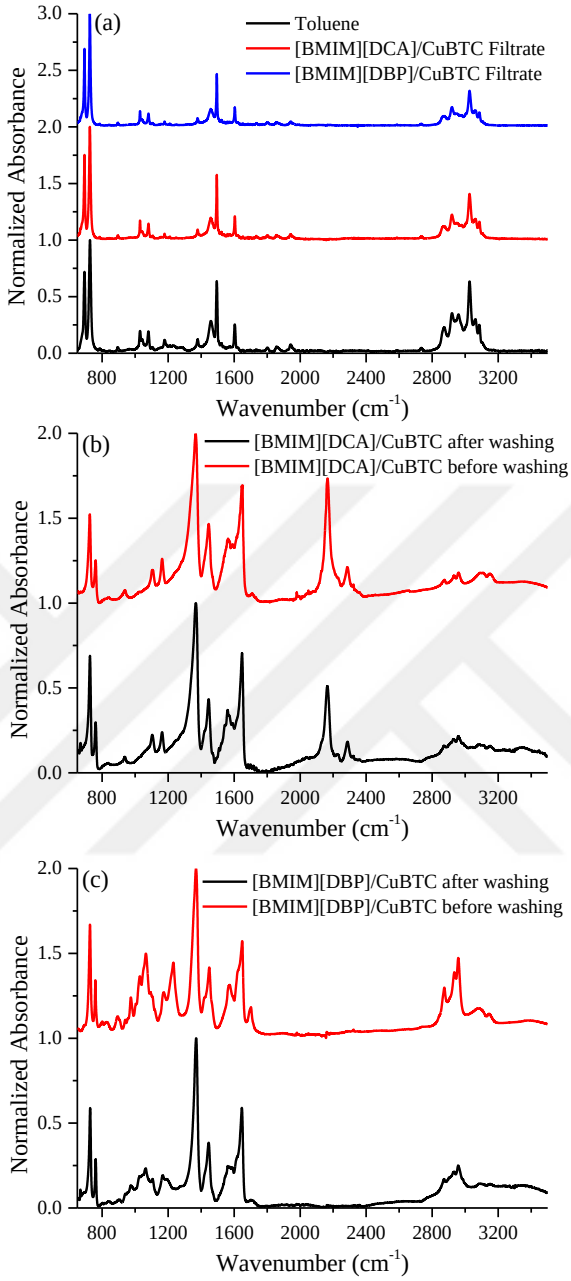

Figure B.5. FTIR spectra of (a) toluene, filtrate after washing [BMIM][DCA]/CuBTC and filtrate after [BMIM][DBP]/CuBTC with toluene. FTIR spectra of (b) [BMIM][DCA]/CuBTC and (c) [BMIM][DBP]/CuBTC before and after washing.

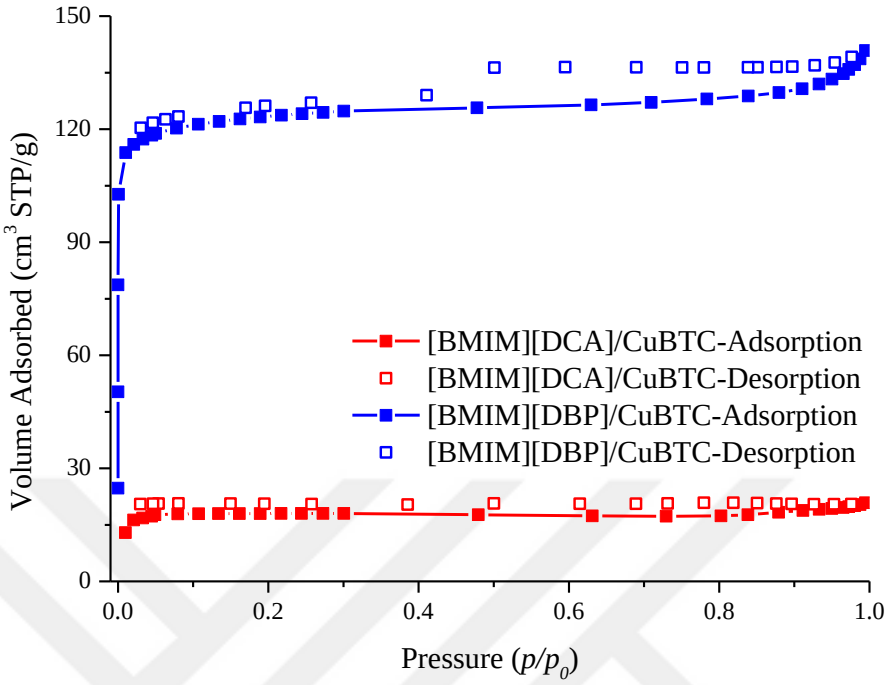

Figure B.6. N_2 adsorption-desorption isotherms of [BMIM][DCA]/CuBTC and [BMIM][DBP]/CuBTC at -196 °C.

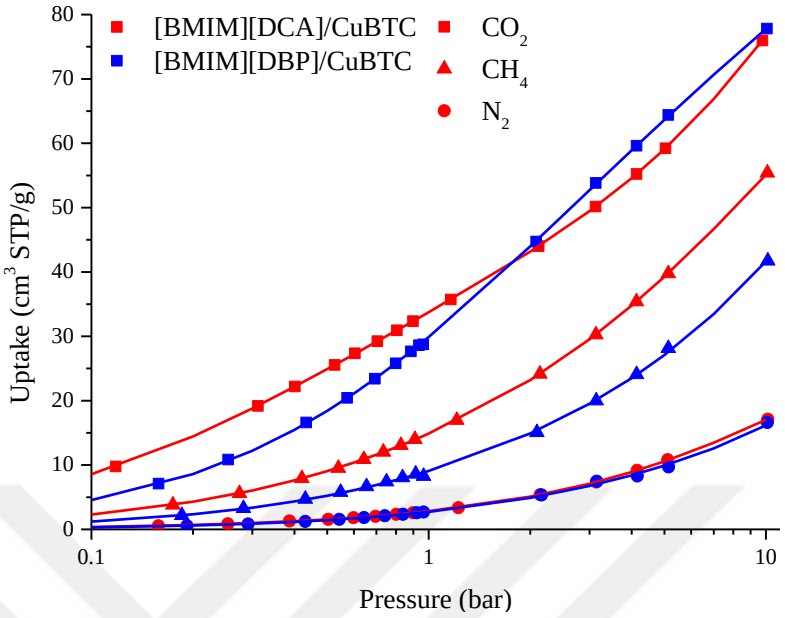

Figure B.7. Experimental adsorption isotherms and dual-site Langmuir fits of [BMIM][DCA]/CuBTC and [BMIM][DBP]/CuBTC. Lines represent the corresponding dual-site Langmuir fit.

APPENDIX C: Supplementary Information for Chapter 5

Table C.1. Freundlich* fit parameters for N_2 adsorption isotherms of UiO-66 and [BMIM][BF_4]/UiO-66.

	UiO-66	[BMIM][BF_4]/UiO-66
q (cm^3/g)	66.2182	45.9076
k (1/bar)	1.61113	1.84788
N	1.35242	1.39723
R^2	0.999	0.999

*Freundlich isotherm:

$$\mathrm{n(P)} = q \times \frac{(k \times \mathrm{P})^n}{1 + (k \times \mathrm{P})^n}$$

where P is the pressure, q is the saturation capacity, k is the affinity constant and n is the Freundlich constant.

Table C.2. Dual-site Langmuir fit parameters for N_2 adsorption isotherms of UiO-66 and [BMIM][BF_4]/UiO-66.

	UiO-66	[BMIM][BF_4]/UiO-66
q_1 (cm^3/g)	1.6100	1.4470
k_1 (1/bar)	18.3336	15.6860
q_2 (cm^3/g)	869.241	236.899
k_2 (1/bar)	0.00386	0.01114
R^2	0.999	0.999

Table C.3. Notes about the structures of MOFs that show APS increase higher than 10-times upon IL-incorporation.

Refcode	**Increase in APS (times)**	**Notes about structures**
ALICEE	194.007	No problems in the structure.
FAGZES	115.135	No problems in the structure. Na^+ ion is kept, which it should.
FAGZAO	102.694	No problems in the structure. Na^+ ion is kept, which it should.
ALICII	92.018	No problems in the structure.
MITGAX	80.553	No problems in the structure.
OHOFIA	79.052	No problems in the structure.
OHOFOG	69.547	Same structure with OHOFIA, but without the guest water molecules.
HAHPIQ	48.009	Cationic framework. $NO3^-$ ions are in the structure.
BEPNIV	39.273	AlaZnOAc. Framework is cationic. Cl^- ions are missing in CCDC therefore in our set.

LARVIL	34.589	No problems in the structure.
MUSMET	29.598	Compound 5 in the paper. No problems in the structure
XEWDUA	29.534	Compound 2 in the paper. No problems in the structure
GAVBIP	27.856	Same structure with reported. But composed of mononuclear units, not connected together.
SERKAC	27.311	Compound 3 in the paper. No problems in the structure
KIGCEK	25.643	ThrZnOAc. No problems in the structure
HOZBUV	23.911	Complex8. No problems in the structure.
QOSXAY	22.594	Hydrogen atoms are missing.
ILUCIC	22.199	MOF8. No problems in the structure.
ILUCOI	22.089	No problems in the structure. Er complex.
BEPPOD	21.973	Compound ValZnFor, similar structure with BEPNIV. Cl^- ions are missing in CCDC therefore in our set.
JOYKUF	21.623	Structure has chemisorped CO_2.
CANYUN	20.951	Compound 1. Desolvation of the compound leads to some disorder, not complete collapse.
ILUCUO	20.928	No problems in the structure. Sm complex
BEPNOB	20.367	Compound AlaZnFor, similar structure with BEPNIV. Cl^- ions are missing in CCDC therefore in our set.
ISOHEE	20.365	Structure collapses without water molecules.
FAKLUA	20.216	Anionic framework, but it seems to be fine with Zn^+ ions in the middle of the pores
IBICUT	18.335	Compound MOF1'. No problems in the structure.

XUMMUP	18.045	Complex 3. Cl^- is present in a water complex but waters are erased, Cls are not.
BEPLUF	17.628	Compound AlaZnFor, similar structure with BEPNIV. Cl^- ions are missing in CCDC therefore in our set.
VACFUB	17.585	Hydrogen atoms are missing.
BEPPIX	15.646	Compound ValZnOAc, similar structure with BEPNIV. Cl^- ions are missing in CCDC therefore in our set.
ILUDAV	15.577	No problems in the structure. Tb complex
DETHEQ	14.852	$NO3^-$ ions were deleted. They were a part of the structure.
BIDQOU	13.743	Hydrogen atoms are missing.
HAWMAT	13.705	Structure is composed of units that are not connected to each other.
ZASJAG	13.663	No problems in the structure.
SERKEG	13.293	Same structure with SERKAC, but with Y atoms.
BEPMEQ	12.765	Compound AlaZnCl, similar structure with BEPNIV. No problems in the structure.
BEPMAM	12.760	Compound AlaZnFor, similar structure with BEPNIV. Cl^- ions are missing in CCDC therefore in our set.
VACFUB01	12.604	Same structure with VACFUB but hydrogens were added. No problems.
BEPNUH	12.560	Compound AlaZnBr, similar structure with BEPNIV. No problems in the structure.
SEGBOX	12.369	No problems in the structure.
REZXIE	12.277	Not the structure from the article.

BEPMIU	11.732	Compound AlaZnCl, similar structure with BEPNIV. No problems in the structure.
REZXIE01	11.508	Not the structure from the article.
AJAGOI	11.376	Compound 4. No problems
CETHEQ	11.099	Compound 1. No problems
GEXFOG	10.826	Complex 6. Composed of 1D units held together by pi interactions. $ClO4^-$ anions are in the structure
TEJLIF	10.518	No problems in the structure.
IBICED	10.442	Structure MOF2. No problems in the structure.
XESKOX	10.429	Hydrogen atoms are missing.
CADZOY	10.395	Composed of 1D units held together by pi interactions. Hydrogen atoms are missing.
QALGUH	10.383	Mil-53(Cr). No problems in the structure.
IBIDAA	10.347	Same with IBICED but without water molecules. Structure MOF2. No problems in the structure.